Universitá degli Studi di Padova

Centro Ricerche Fusione (**CRF**)

Universitá degli studi di Napoli Federico II

Universidade de Lisboa

Instituto Superior Técnico (**IST**)

JOINT RESEARCH DOCTORATE IN FUSION SCIENCE AND ENGINEERING

Cycle XXX

POWER EXHAUST DATA ANALYSIS AND MODELING OF ADVANCED DIVERTOR CONFIGURATIONS

Coordinator: Prof. Paolo Bettini

Supervisors: Dr. Flavio Crisanti

Ph.D. student: Giulio Rubino

Padova, January 2018

UNIVERSITÀ DEGLI STUDI DI PADOVA

JOINT Doctorate and NETWORK in Fusion Science and Engineering

Network Partners:

- Instituto Superior Técnico (IST) Lisboa, Portugal
- Universitá degli studi di Padova, Italy
- Ludwig Maximilians University Munich, Germany

In collaboration with:

Consorzio RFX
IPP Garching, Germany

A mio padre Matteo

Contents

List of Figures

List of Tables

Acknowledgements

Ringrazio sentitamente il mio supervisore Dr. Flavio Crisanti per la loro costante presenza, per la sua costante disponibilità mostrata nei miei confronti e per abvermi guidato durante l'intero svolgimento di questo lavoro. I suoi suggerimenti e l'opportunità di poter confrontare i nostri punti di vista hanno arricchito il mio bagaglio di conoscenze e mi hanno fatto evolvere a livello professionale.

Vorrei inoltre ringraziare il Dr. Bruno Viola, il Dr. Paolo Innocente, il Dr. Vincenzo Pericoli e il Prof. Giuseppe Calabró per le utili discussioni e dell'aiuto che mi hanno fornito durante lo svolgimento di questo progetto di ricerca.

Vorrei ringraziare il personale del Centro Ricerche Fusione ENEA Frascati e il personale dei centro di ricerca Consorzio RFX di Padova.

Ringrazio mia madre Renza, mia sorella Rossella e mio fratello Fausto che mi hanno aiutato ad affrontare questa esperienza spingendomi a dare il meglio di me. Vi ringrazio per tutto quello che ogni giorno fate per me.

Ringrazio la mia fidanzata Donatella. La ringrazio per tutto quello che fa costantemente per me ogni giorno, per la forza che riesce a darmi nell'affrontare le difficoltá che incontro e per i momenti stupendi che continua a regalarmi.

Ringrazio i miei amici di sempre, quelli presenti e quelli che purtroppo non ci sono più, e tutti gli amici incontrati durante questo percorso.

Soprattutto ringazio te papà, per avermi seguito nel corso della mia vita e per avermi reso la persona che sono. Mi hai insegnato tanto, mi hai insegnato che non bisogna mai arrendersi, che c'è sempre la speranza che le cose possano andare meglio, che le situazioni bisogna affrontarle con positività e con il sorriso per quanto difficili e dure possano sembrare. Grazie per tutto quello che hai fatto e per tutto quello che continui a fare per me.

Abstract

The possibility to exploit fusion energy in a reliable, safe and available way is one of the greatest challenges in the worldwide research. Very hot magnetically confined plasma are required to achieve high rates of fusion reactions. However, these conditions are not compatible with the material facing the plasma. In order to protect the wall, a hot core confined region is created while most of the power and particles are ultimately exhausted in a properly design component of the reactor, the so-called *divertor*.

The Ph.D. activity presented in this thesis is carried out in the framework of EUROfusion program for the realization of a Demonstration power plant (DEMO) by the years 2050 . One of the most critical aspects has been recognized in the exhaust of huge amount of power which can severely damage the plasma facing component (PFC). Therefore, the analysis of the plasma conditions in the divertor region is essential to asses the reliability and the feasibility of a fusion reactor machine. In order to mitigate the power exhaust issue the fusion community is currently investigating several possible solutions as the use of alternative magnetic divertor configurations (AC) or the use of liquid metal as PFC.

This thesis focuses on the study of the Scrape off Layer (SOL), the region where the particles coming out of the core are diverted towards the target plates. The modelling is performed by means of 2D edge codes on future and existing fusion reactors.

The first point in the analysis is the assessment of the edge plasma conditions in DEMO by considering a set of simplifying assumptions and taking into account a possible set of reference parameters. A scoping study is performed to evaluate the behaviour of the SOL plasma by varying the density and the transport coefficients. The numerical simulations are performed by means of the EDGE2D-EIRENE code. The results of the calculations predict divertor conditions totally unacceptable from an operational point of view. Most importantly, since the most used and validated code available in the fusion community are not able to deal with ACs, we perform a benchmark between EDGE2D-EIRENE and TECXY. The latter is a simple and fast code able to treat ACs. Despite the differences in the physical model adopted by the two numerical tools, the results shows a good match, especially in terms of power loads on the target plates and general trends of global quantities. On the other hand, discrepancies are observed in the electron density and temperature profiles on the outer divertor primarily due to the different numerical models adopted for the neutral particles description.

As a second step, we perform the analysis of an AC by comparing a conventional Single Null (SN) and a Quasi snowflake (QSF, characterized by a transition from Snowflake to X-Divertor configurations) magnetic configurations of DTT (Divertor

Test Tokamak). The modelling is performed by means of EDE2D-EIRENE. The scoping study obtained by varying the upstream density investigates three different aspects: the effect on the attainment of the detachment, the effect on the power loads and the effect on the neutral particles behaviour. The simulations show that the QSF configuration is more prone to reach detached divertor conditions than the SN configurations. Furthermore, while in SN unacceptable power loads are foreseen onto the outer target plates, in case of QSF manageable values of the power peaks are obtained. This difference is primarily due to geometrical factors, especially the main driver is recognized in the flaring of the flux surfaces in the divertor region. By analysing the neutral particles behaviour, we see that a better confinement is achieved in QSF than in SN since the ionization front is not able to move towards the X-point. A preliminary analysis of liquid lithium divertor is also discussed. Since we simulate regimes dominated by the sputtering, minor differences are observed by comparing the liquid lithium divertor and the standard Tungsten one.

The last point of the research activity concerns the use of a different 2D edge code, i.e. SOLEDGE2D-EIRENE. Thanks to the high flexibility, this code is able to treat ACs. We discuss the preliminary results of a validation phase carried out by comparing the numerical results with the experimental one. While the upstream profiles are fairly reproduced by varying the diffusion coefficients, the target quantities shows mismatches in terms of electron density and temperature whereas the power profile is partially recovered. The results are then compared in terms of radiation distribution. The code is able to reproduce the 2D distribution in the high field side, even though discrepancies on the inner divertor baffle are observed. Finally, we show that improvements can be obtained by suitably defining the recycling coefficient.

This thesis is organized as follows.

In **chapter 1**, a general discussion on fusion energy and on the magnetic confinement configuration will be addressed. The main phenomena characterizing the SOL plasma are described and a short introduction of the alternative divertor configurations is given.

In **chapter 2**, the general physical model used by the 2D edge code is derived. In addition, the different methods used to describe the neutral particles are presented. In the last section the main features of the codes used in this thesis are discussed.

In **chapter 3**, we present the results of the modelling performed with EDGE2D-EIRENE. In the first section the results of the DEMO simulations are discussed, while in the second part we focuses on the modelling of the alternative divertor configurations of DTT.

In **chapter 4**, the preliminary results of the validation phase of SOLEDGE2D-EIRENE are given. In particular, the numerical results are compared to the experimental data of the JET pulse 91986.

Finally, the **conclusions** are presented in the last chapter with an overview of

possible future works.

Sommario

La possibilitá di poter sfruttare l'energia da fusione in modo affidabile, sicuro and con alta disponibilitá é una delle piú grandi sfide della ricerca mondiale. Plasmi ad altissima temperatura confinati magneticamente sono necessari per raggiungere alti tassi di reazioni di fusione. Tuttavia queste condizioni non sono compatibili con i materiali affaciati sul plasma. Al fine di proteggere la parete, viene creato un regione molto calda confinata mentre la maggior parte della potenza e delle particelle sono essenzialmente smaltite in uno specifico componente del reattore, il cosiddetto '*divertore*'.

L'attivitá di ricerca del dottorato presentato in questa tesi é stata fatta all'interno del programma EUROfusion per la realizzazione di un reattore dimostrativo (DEMO) entro il 2050. Uno degli aspetti piú critici é stato individuato nello smaltimento di alte potenze che possono danneggiare irreparabilmente i componenti affacciati al plasma (PFC). Quindi, l'analisi delle condizioni di plasma nella regione del divertore é essenziale per valutare l'affidabilitá e la fattibilitá dei reattori a fusione. Al fine di mitigare il problema dello smaltimento della potenza la comunitá fusionistica sta attualmente studiando diverse soluzioni possibili come l'uso di configurazioni magnetiche alternative nel divertore (AC) o l'uso di metalli liquidi come PFC.

Questa tesi si concentra sullo studio dello Scrape off Layer (SOL), la regione dove le particelle che escono dal nucleo caldo sono dirottate verso i piatti del divertore. La modellazione numerica viene effettuata con codici di bordo bidimensionali su macchine future ed esistenti.

Il primo punto nell'analisi consiste nella valutazione delle condizioni del plasma di bordo in DEMO considerando alcune ipotesi semplificative e un insieme di parametri di riferimento. Uno studio esplorativo viene fatto per valutare il comportamento del plasma nel SOL variando la densitá e i coefficienti di trasporto. Le simulazioni numeriche sono state fatte con il codice EDGE2D-EIRENE. I risultati predicono condizioni nel divertore totalmente inaccetabili dal punto di vista operazionale. Abbiamo soprattutto effettuato un benchmark tra EDGE2D-EIRENE e TECXY dato che i codici piú utilizzati e verificati attualmente disponibili nella comunitá fusionistica non sono in grado di trattare le AC. TECXY é un codice semplice e veloce in grado di gestire le AC. Nonostante le differenze nei modelli fisici utilizzati nei due codici, i risultati mostrano un buon accordo, in particolare in termini di carichi termici sui piatti del divertore e trend generali delle quantitá globali. D'altro canto discrepanze sono osservate nei profili della temperature e densitá elettronica sul divertore esterno principalmente dovute ai diversi modelli numerici adottati per la descrizione delle particelle neutre.

Il seocndo punto nell'analisi riguarda le AC fatta comparando una configurazione magnetica a singolo nullo (SN) convenzionale con un quasi Snowflake (QSF, caratterizzato da una transizione da una configurazione Snowflake ad una X-divertor) del reattore DTT (Divertor Test Tokamak). La modellizzazione é fatta con EDGE2D-EIRENE. Lo studio preliminare effettuato variando la densitá a monte si propone di indagare tre aspetti principali: l'effetto sul raggiungimento del detachment, l'effetto sui carichi termici e l'effetto sul comportamento dei neutri. Le simulazioni mostrano che la configurazione QSF é piú incline a raggiungere il detachment rispetto al caso SN. Inoltre, mentre nel caso SN sono predetti carichi termici inaccetabili sui piatti esterni, in QSF sono ottenuti valori gestibili di picchi di potenza. Questa differenza risiede principalmente in fattori geometrici ed in particolare il fattore primario é riconducibile all'allargamento delle superfici di flusso nella regione del divertore. Analizzando il comportamento dei neutri si osserva un miglior confinamento in QSF che in SN dato che il fronte di ionizzazione non riesce a risalire verso il punto ad X. Un'analisi preliminare di un divertore a litio liquido é anche discussa. Leggere differenze sono osservate confrontando il divertore a litio liquido e quello convenzionale in tungsteno in quanto vengono simulati regimi dominati dallo sputtering.

L'ultimo punto nell'attivitá di ricerca riguarda l'utilizzo di un diverso codice di bordo, SOLEDGE2D-EIRENE. Grazie all'alta flessibilitá, questo codice é in grado di trattare le AC. Vengono discussi i risultati preliminari della fase di convalida effettuata confrontando i risultati numerici con quelli sperimentali. Mentre i profili a monte sono discretamente riprodotti variando i coefficienti di diffusione, le quantitá a valle mostrano discrepanze in termini di densitá e temperature elettroniche. D'altro canto il profilo di potenza é parzialmente riprodotto. I risultati sono successivamente comparati in termini di distribuzione della radiazione. Il codice riesce a riprodurre la distribuzione 2D nella parte ad alto campo anche se differenze sul baffle interno sono presenti. Infine mostriamo che miglioramenti possono essere ottenuti definendo in modo adatto il coefficiente di riciclo.

Questa tesi é organizzata come segue.

Nel **capitolo 1** l'energia da fusione e le configurazioni magnetiche vengono presentate nei loro aspetti generali. I fenomeni principali caratterizzanti il plasma nel SOL sono descritti e viene data una breve introduzione alle configurazioni alternative del divertore.

Nel **capitolo 2** il modello fisico piú generale utilizzato nei codici 2D di bordo viene derivato. Inoltre i diversi modelli utilizzati per i neutri sono descritti. Nell'ultima parte le principali caratteristiche dei codici utilizzati nella tesi sono descritte.

Nel **capitolo 3** presentiamo i risultati delle simulazioni fatte con EDGE2D-EIRENE. Nella prrima parte sono descritti i risultati di DEMO mentre nella seconda parte ci si focalizza sulla modellazione delle configurazioni alternative del divertore.

Nel **capitolo 4** i risultati preliminari della fase di convalida di SOLEDGE2D-EIRENE sono presentati. I risultati numerici sono confrontati con quelli sperimentali

dell'impulso 91986 del JET.

Infine le **conclusioni** sono presentate nell'ultimo capitolo con un panorama sui possibili sviluppi futuri.

Resumo

A possibilidade de explorar a energia de fusão de uma maneira confiável, segura e disponível é um dos maiores desafios da pesquisa mundial. Plasma muito quente e magneticamente confinado é necessário para obter altas taxas de reações de fusão. Contudo, essas condições não são compatíveis com o material que enfrenta o plasma. Para proteger a parede, uma região confinada no núcleo quente é criada, enquanto a maior parte da energia e das partículas são, por fim, esgotadas num componente do reator adequadamente projetado, o chamado 'divertor'.

A actividade de doutoramento apresentada nesta tese é realizada no âmbito do programa EUROfusion para a realização de uma Central de Demonstração (DEMO) até 2050. Um dos aspectos mais importantes foi reconhecido como o escape de grandes quantidades de energia, que podem danificar severamente o componente que enfrenta o plasma (plasma facing component - PFC). Por isso, a análise das condições plasmáticas na região do divertor é essencial, para avaliar a confiabilidade e a viabilidade de uma máquina de reator de fusão. Para mitigar o problema de escape de energia, a comunidade de fusão está atualmente investigando várias soluções possíveis, como o uso de configurações de divertor magnético alternativas (alternative magnetic divertor configurations - AC) ou o uso de metal líquido como PFC.

Esta tese enfoca o estudo do Scrape Off Layer (SOL), a região onde as partículas que saem do núcleo são desviadas para as placas alvo. A modelagem é realizada por meio de 2D código de borda sobre reatores de fusão existentes e futuros.

O primeiro ponto na análise é a avaliação das condições plasmáticas de borda em DEMO, considerando um conjunto de premissas simplificadoras e tendo em conta um possível conjunto de parâmetros de referência. Um estudo de escopo é realizado para avaliar o comportamento do plasma SOL, variando a densidade e os coeficientes de transporte. As simulações numéricas são realizadas por meio do código EDGE2D-EIRENE. Os resultados dos cálculos prevêem condições para o divertor completamente inaceitáveis de um ponto de vista operacional. Mais importante, visto que os código mais usados e validados, disponível na comunidade de fusão, não são capazes de lidar com ACs, realizamos uma comparação entre EDGE2D-EIRENE e TECXY. O último é um código simples e rápido, capaz de lidar com ACs. Apesar das diferenças no modelo físico adotado pelas duas ferramentas numéricas, os resultados mostram uma boa combinação, especialmente em termos de cargas de energia nas placas alvo e de tendências gerais de quantidades globais. Em contrapartida, observam-se discrepâncias na densidade eletrônica e nos perfis de temperatura no divertor externo, principalmente devido aos diferentes modelos numéricos adotados para a descrição das partículas neutras.

Como um segundo passo, realizamos a análise de uma AC, comparando as configurações magnéticas convencionais Nulo único (SN) e Quasi Snow Flake (QSF, caracterizado por uma transição das configurações Snowflake para X-Divertor) do DTT (Dambor Test Tokamak). A modelagem é realizada por EDE2DEIRENE. O estudo de escopo obtido pela variação da densidade a montante indaga três aspectos diferentes: o efeito na conquista do destacamento, o efeito sobre as cargas de energia, e o efeito sobre o comportamento das partículas neutras. As simulações mostram que a configuração QSF é mais propensa a alcançar condições de desviados destacadas do que as configurações SN. Além disso, enquanto na configuração SN são previstas cargas de energia inaceitáveis nas placas alvo externas, no caso da configuração QSF são obtidos valores gerenciáveis dos picos de energia. Esta diferença é principalmente devida a fatores geométricos, especialmente o driver principal é reconhecido na queima das superfícies de fluxo na região do divertor. Ao analisar o comportamento das partículas neutras, vemos que um melhor confinamento é alcançado na QSF do que na SN, uma vez que a frente de ionização não é capaz de se mover para o ponto X. Uma análise preliminar do divertor de lítio líquido também é discutida. Como simulamos regimes dominados pela pulverização catódica, observam-se pequenas diferenças comparando simulamos regimes dominados pela pulverização catódica, observam-se pequenas diferenças comparando o divertor de lítio líquido e um divertor padrão de Tungstênio.

O último ponto da atividade de pesquisa diz respeito ao uso de um 2D código de borda diferente, ou seja, SOLEDGE2D-EIRENE. Graças Ã alta flexibilidade, este código é capaz de lidar com ACs. Discutimos os resultados preliminares de uma fase de validação realizada comparando os resultados numéricos com o resultado experimental. Embora os perfis a montante sejam reproduzidos de forma justa variando os coeficientes de difusão, as quantidades alvo mostram desajustes em termos de densidade e temperatura de elétrons, enquanto o perfil de energia é parcialmente recuperado. Os resultados são então comparados em termos de distribuição de radiação. O código é capaz de reproduzir a distribuição 2D no lado do campo alto, mesmo que sejam observadas discrepâncias no deflector interno do divertor. Finalmente, mostramos que melhorias podem ser obtidas definindo adequadamente o coeficiente de reciclagem.

Esta tese está organizada da seguinte forma:

No **capítulo 1**, será abordada uma discussão geral sobre energia de fusão e sobre a configuração de confinamento magnético. Os principais fenômenos que caracterizam o plasma SOL são descritos e é dada uma breve introdução das configurações de divertor alternativas.

No **capítulo 2**, o modelo físico geral usado pelo 2D código de borda é derivado. Além disso, são apresentados os diferentes métodos utilizados para descrever as partículas neutras. Na última seção são discutidas as principais características dos códigos usados nesta tese.

No **capítulo 3**, apresentamos os resultados da modelagem realizada com EDGE2DEIRENE. Na primeira seção são discutidos os resultados das simulações DEMO, enquanto a segunda parte centra-se na modelagem das configurações de divertor alternativas do DTT.

No **capítulo 4**, são fornecidos os resultados preliminares da fase de validação do SOLEDGE2DEIRENE. Em particular, os resultados numéricos são comparados aos dados experimentais do pulso JET 91986.

Finalmente, as **conclusões** são apresentadas no último capítulo, junto a uma visão geral sobre os possíveis trabalhos futuros.

Chapter 1

Fusion Energy and plasma wall interaction

The future energy mix and the combination of different resources is becoming more and more important, due to the constantly increasing world energy demand. Nuclear energy, and in particular fusion energy, has an enormous potential and may represent a non-negligible part of the future energy supply, especially in view of a low carbon global electricity system[1]. In 2012 EFDA (European Fusion Development Agreement) published the 'Fusion Electricity - A roadmap to the realisation of fusion energy' [2] report which sets up a strategic path to follow for the generation of electrical power by a Demonstration Fusion Power Plant (DEMO) by the year 2050. The roadmap defines eight major challenges to overcome that tackle the physics, engineering and economic aspects of a future power plant. In particular, one of the missions is related to "Heat-exhaust issue" since most of the power is ultimately exhausted in very narrow region on a specific designed component of the reactor, the divertor. In this section we will give a brief and general overview of the thermonuclear fusion, of the main features of the fusion reactors and of the power exhaust related problem, by highlighting the main challenges to face out and introducing the possible solutions that could be adopted.

1.1 Fusion overview

The basic idea of nuclear fusion is to combine two light particles, exploiting the difference of mass between the reactants and the products of the reaction. This mass defect is converted into energy. A physical explanation can be obtained by considering the binding energy per nucleon of the different chemical elements, which is the result of the competition between the long range Coulomb forces and the short range nuclear forces. The binding energy is weaker for lighter and heavier elements. Therefore, a release of energy can occur either by splitting heavy nucleus, or by

Table 1.1: Fusion reaction for energy production and the released energy.

Name	Reaction	Energy [MeV]
DT	D + T $\rightarrow \alpha$ + n	17.6
DD	D + D $\rightarrow {}^3He$+ n	3.27
DD	D + D $\rightarrow$ T + p	4.03
D ^3He	D + $^3He \rightarrow \alpha$ + p	18.3

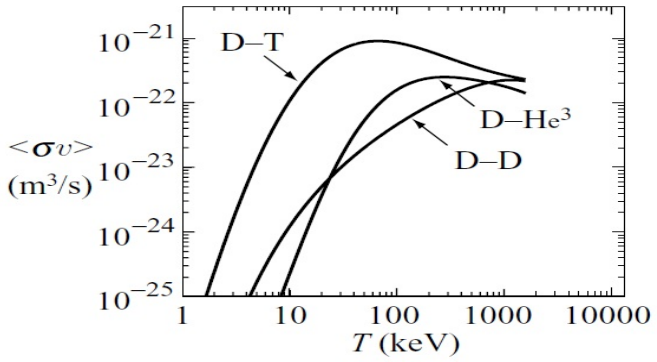

Figure 1.1: Averaged fusion cross section $\langle \sigma v \rangle$ vs. nucleon Temperature in [KeV] for the DD, DT and D$_3He$ reactions [3].

combining two light ones, as we move to more strongly bounded elements.

There are three different fusion reactions advantageous for nuclear energy production, as shown in table 1.1, involving Deuterium, Tritium and ^3He. In order to have a fusion reaction the two nuclei must be close enough, within a distance of the order of few femtometers, to overcome the repulsive Coulomb force. Figure 1.1 depicts the fusion cross section σ, which can be view as the probability that two nuclei will undergo a fusion reaction, averaged on the velocity space as a function of the temperature for the main fusion reactions in table 1.1. It is clear that the most interesting reaction is the DT one, as it is the easiest to initiate and it is the central focus of fusion worldwide research. The fuel temperature able to produce fusion reactions is of order of tens of KeV[1]. In this condition the fuel is in state of plasma, i.e. a quasi-neutral fully ionized gas characterized by a high electrical conductivity and whose behaviour is dominated by collective effects. The high electrical conductivity results in the ability to shield electrical field. In a plasma, the typical dimension

[1]In plasma physics the temperature is often expressed in electronvolts (eV) or kiloelectronvolts (KeV), since the considered phenomena involve very high temperature. The relation between eV and K is 1eV= 11605 K

where charge inhomogeneity can appear is defined by the Debye length λ_D[3]:

$$\lambda_D = \sqrt{\frac{\epsilon_0 T_e}{n_e e^2}}, \tag{1.1}$$

while the characteristic plasma oscillation is defined by the plasma frequency ω_p[3]:

$$\omega_p = \sqrt{\frac{n_e e^2}{m_e \epsilon_0}}. \tag{1.2}$$

Plasma behaviour requires $\lambda_D \ll L$ and $\omega_p \gg \omega_T$, where L and $\omega_T = v_T/L$ are the typical macroscopic length and macroscopic frequency (the inverse thermal transit time), respectively. Furthermore, in order for collective effects to dominate, the number of particles in a Debye sphere must be greater than one, namely [3]:

$$\Lambda_D = \frac{4}{3}\pi\lambda_D^3 n_e = \frac{4\pi}{3}\frac{\epsilon_0^{3/2} T_e^{3/2}}{e^2 n_e^{1/2}}. \tag{1.3}$$

The confinement of this hot plasma is a crucial aspect in a fusion reactor. Nowadays, the most promising confinement method is by means of magnetic fields, i.e. by using Magnetic Confinement (MC). The charged particles are subject to the Lorentz force and are bound to the magnetic field lines gyrating with the characteristic Larmor radius ρ_L and cyclotron frequency ω_c:

$$\rho_L = \frac{m v_\perp}{q|B|},\ \omega_c = \frac{q|B|}{m}. \tag{1.4}$$

Ideally, in a fusion reactor we would get a self sustained reaction that means the power produced in the fusion reaction must compensate the unavoidable losses. Since in a MC reactor the neutrons do not heat up the plasma, the alpha power, P_α, must balance the Bremsstrahlung, synchroton and thermal conduction losses. This ignition criterion is satisfied if[3]:

$$nT\tau_E = 8.3\ atm \cdot s,\ T = 15KeV \tag{1.5}$$

where n is the fuel density (equal for D and T), T is the ions temperature and τ_E is the energy confinement time. $nT\tau_E$ is called triple product and can represent a measure of the quality of the confinement. However, we actually need an external power P_{in} to sustain the steady state condition of a fusion reactor. We can therefore define the 'gain factor' Q[3]:

$$Q = \frac{P_{out} - P_{in}}{P_{in}} \tag{1.6}$$

where P_{out} is the output thermal power. Clearly, for ignition we have $Q = \infty$, while for the next step fusion device ITER it is expected to have $Q = 10$.

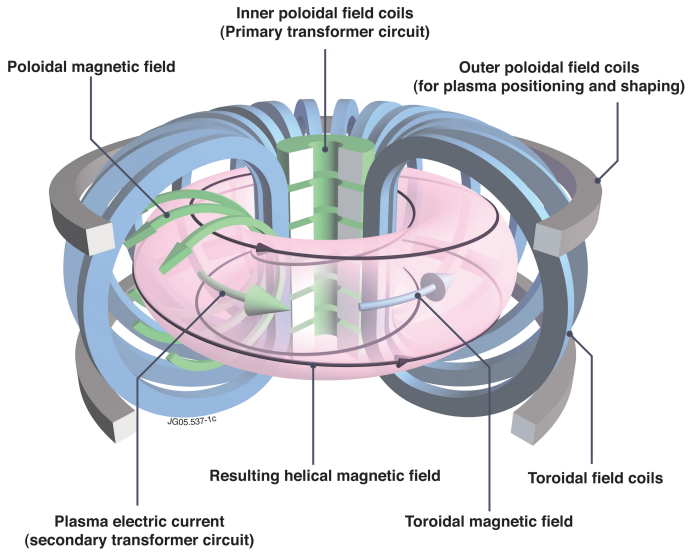

Figure 1.2: Schematic representation of a Tokamak[4].

1.2 Tokamak

The Tokamak (Russian acronym for '**to**roidal'naya **ka**mera s **ma**gnitnymi **k**atushkami', toroidal chamber with magnetic coils) is a donut-shaped device where the confinement magnetic field is obtained by a combination of a toroidal B_{tor} and a poloidal B_{pol} magnetic field. Figure 1.2 shows a schematic representation of a Tokamak. The toroidal field is obtained by a set of toroidal field coils distributed all around the torus. The need to superimpose a poloidal field comes from equilibrium problems in presence of a pure B_{tor}. Indeed, the toroidal field B_{tor} scales as 1/R producing a vertical separation between ions and electrons in the plasma column due to the $\nabla B \times B$ drift[3]. This charge separation produces an electric field that entails an $E \times B$ drift, which in turn pushes the plasma outward. To overcome the problem encountered in a pure toroidal field we need to add a magnetic poloidal component B_{pol}. The combination of B_{pol} and B_{tor} prevents the build-up of the particles on the top and on the bottom of the plasma. In a Tokamak the poloidal field is generated by an internal plasma current I_p. In the so-called 'inductive tokamak', this plasma current is induced by the central transformer coil, referred to as Central Solenoid (CS), while the plasma acts as the secondary of the transformer. Naturally, in these devices the length of the pulse is limited by the allowed flux swing of the CS. The resulting helical magnetic field is shown in figure 1.2.

The equilibrium field is characterized by nested magnetic surfaces traced out by the helical field lines whose center is the magnetic axis. By considering a circular corona delimited by the magnetic axis and a magnetic surface, we have that the poloidal flux Ψ_p is constant. Therefore, the magnetic flux surfaces can be mapped

out by means of the poloidal flux coordinate Ψ and are also called flux surfaces. In tokamaks devices, the plasma is confined by closed magnetic surfaces and bounded by the so-called Last Close Flux Surface (LCFS). Beyond the LCFS there is a region of open field line, in direct contact with the wall, named Scrape-Off Layer (SOL). In this latter region, the power conducted and convected by the charged particles is directly deposited on narrow area of the solid surface which is eventually exposed to high thermal loads that could damage the surface itself. A more detailed description of the SOL and the related issues, also known as 'Power exhaust issue', will be given in the next section.

It is useful to introduce the key concept of safety factor q, that is the number of toroidal turns $\Delta\phi$ made by the field line per poloidal turn $\Delta\theta = 2\pi$:

$$q = \frac{\Delta\phi}{2\pi}. \tag{1.7}$$

This parameter is strictly connected to the stability and the configurations with an higher q are more stable, hence the name safety factor.

As previously mentioned, the performance of a fusion reactor can be evaluated by considering the *triple product* and in particular the confinement time τ_E. In the early 1980s, there was a step forward the increase in tokamak performance with the discovery of the H-mode on the ASDEX tokamak, where H stays for high confinement[5]: a sharp increase of τ_E of a factor 2 was seen above a critical power threshold. The transition from L-mode (low confinement) to H-mode is mainly related to a radial turbulence suppression in the edge region that is the dominant mechanism for the edge radial transport. A region of steep radial pressure gradients and of an Edge Transport Barrier (ETB) builds up and the of so-called *'pedestal'* forms. The L-H transition is strictly connected to the power crossing the LCFS and entering the SOL, imposing a threshold to operate in H-mode $P_{SOL} > P_{LH}$. However, in this new confinement regime a new class of instability arises, the Edge Localized Mode (ELM), which results in high transient heat and particle load on the first wall and driven by the steep gradients of edge temperature and density[6].

Several tokamak devices are now present all over the world with different size and different features. We will give below a general description of the main present and future machines.

1.2.1 JET

JET (Joint European Torus) is largest tokamak in the world and is located in Culham UK. Figure 1.3 shows a drawing of the machine. It is a D-shaped reactor with major radius $R = 3m$, minor radius $a = 0.9m$ and a plasma volume of $V_{pl} = 90m^3$ equipped by a set of 32 toroidal water cooled copper coils, the CS and 6 poloidal magnets, which produce a toroidal magnetic field up to 3.5 T with a plasma current up to $4MA$. The auxiliary heating system is a combination of Neutral Beam

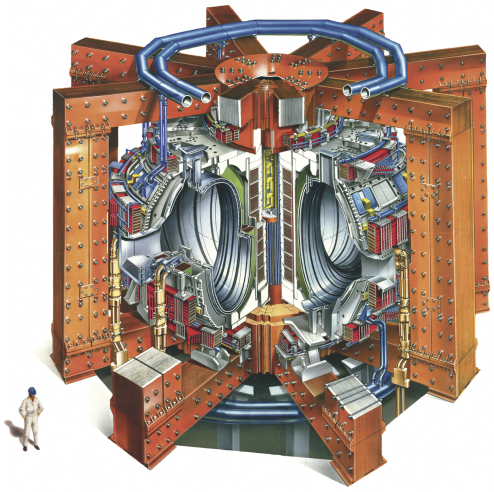

Figure 1.3: Drawing of the JET machine[7].

Injection (NBI, up to $34MW$), Ion Cyclotron Resonance Heating (ICRH, up to $10MW$) and Lower Hybrid Current Drive (LH, up to $7MW$)[8]. It is worth noting the presence of the iron transformer core which is used to improve the efficiency of the primary field and to reduce the stray fields.

In operation since 1983, it has been designed to work in conditions approaching the ones required for a fusion reactor. It is the first tokamak that achieved controlled deuterium-tritium fusion power in 1991 and has reached the highest value of the gain factor $Q = 0.65$, producing a fusion power of $P_{fus} = 16.1MW$ in 1997. In recent years, JET plays a pivotal role in the realization of ITER, since it acts as a test bed for the physics, material and systems of it. In this context, in 2011, JET was equipped with the ITER-like plasma facing wall, with Tungsten divertor and Beryllium wall.

1.2.2 ITER and DEMO

ITER (International Thermonuclear Experimental Reactor) is the next step fusion device under construction in Cadarache, France. Its primary goal is to demonstrate the possibility to produce a stable, well-confined plasma with a gain factor $Q = 10$ and discharge lasting for $t = 400s$. It is a superconducting tokamak with $R = 6.2m$ and $a = 2.0m$ (figure 1.4). The plasma is confined with a toroidal magnetic field $B_{tor} = 5.3T$, obtained by a set of 18 superconducting coils, the CS, 6 poloidal coils and a maximum plasma current of $15MA$. The auxiliary heating system are composed by $33MW$ of negative NBI, $20MW$ of ICRH and $20MW$ of Electron Cyclotron Resonant Heating (ECRH). Specifically, the main missions of ITER are:

- the production of $P_{out} = 400MW$ with a input of $P_{in} = 40MW$;

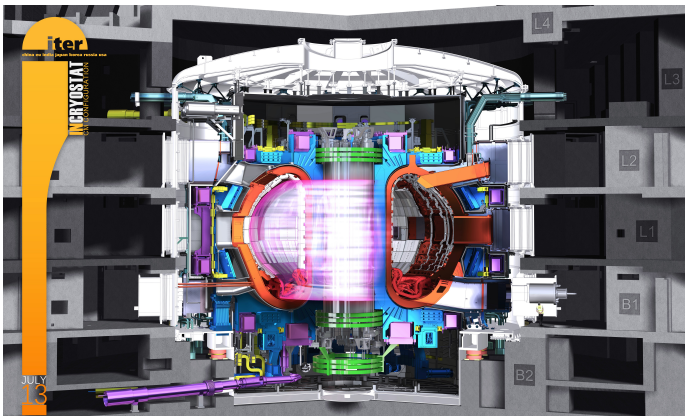

Figure 1.4: Artist's drawing of the ITER device[9].

- to fill the gaps between the present small-scale experimental reactors and a future fusion power plant by testing the technologies and their integrated operation in a reactor;
- to achieve a DT plasma that is sustained by internal heating;
- to test the Tritium breeding concept by inserting some specific Tritium breeding modules in the blanket;
- to demonstrate the safety characteristic of a fusion device;
- to demonstrate the effectiveness of the divertor design.

However, ITER represents an intermediate step towards the realization of a commercial prototype reactor, referred to as DEMO (Demonstration power plant). Currently, a conceptual design of DEMO does not exist and the fusion community is considering all the possible solutions. The main goals for DEMO, highlighted in the EUROfusion roadmap[2], can be summarized in:

- demonstrate the possibility to produce several hundreds of net electric power for the grid;
- achieve the Tritium self-sufficiency;
- demonstrate the availability and the reliability of all the technologies of a future fusion reactor.

Although the solution foreseen for ITER are the base for a future DEMO design, an integrated design is necessary in order to tackle the various criticalities that could be encountered in the transition from ITER to DEMO. In particular, some satellite tokamaks or facilities are now working or planned to work in collaboration to ITER

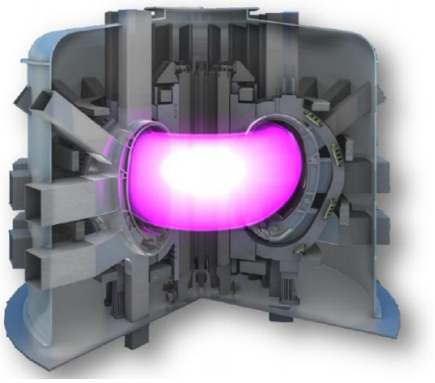

Figure 1.5: Artist's drawing of the DTT device[10].

to study for example the neutron damage on the material in the International Fusion Materials Irradiation Facility (IFMIF).

1.2.3 DTT

A crucial aspect to take into account in DEMO is the power exhaust issue which is much more severe than in ITER and such that the baseline solution that will be tested in ITER may not extrapolate to DEMO. In this context, Italy has proposed a satellite tokamak whose main goal is to test alternative divertor solutions in physics and technological DEMO relevant conditions. The DTT machine (figure 1.5) is characterized by a major radius of $R = 2.15m$, minor radius of $a = 0.7m$ and a toroidal field of $B_{tor} = 6T$ with a plasma current of 6 MA. The external power heating is $P_{in} = 45MW$, obtained by a combination of ECRH, ICRH and NBI. The main issue that DTT should address are:

- study the possible heat exhaust systems capable to withstand the high thermal load of DEMO;
- study the heat exhaust issue that cannot be addressed by the present devices;
- demonstrate that the possible solutions can be integrated in DEMO, by analyzing the physical (exhaust problem and plasma bulk performances) technological (materials compatibility) and engineering aspect (forces on poloidal coils, space constrains, etc).

1.3 The Scrape off layer

Outside the LCFS there is a region of open field lines where the plasma comes in contact with solid surfaces. Clearly, in the SOL region the physical phenomena

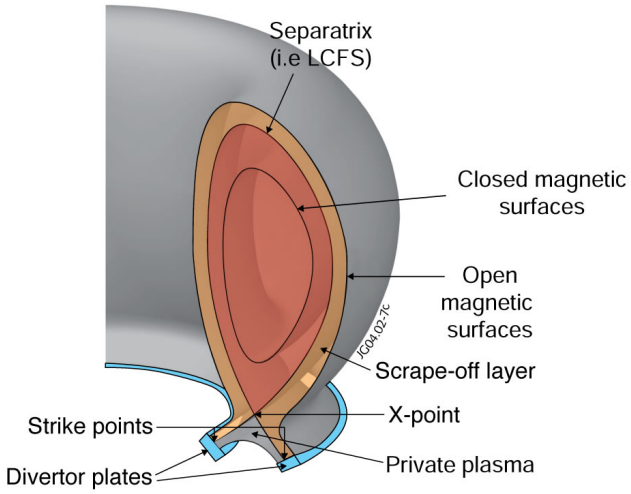

Figure 1.6: Schematic view of a poloidal divertor configuration. The core plasma (red) the SOL (orange) and the private plasma(grey) regions are clearly visible. The LCFS, the divertor plates, the strike points and the X-point are also pointed out[11].

involve plasma-surface and plasma-neutral interactions which play a vital role in the dynamics and performances of the reactor. This boundary region can be created either by inserting a solid object, getting the so-called limiter configuration, or by shaping the poloidal magnetic field by means of external currents, obtaining the so called poloidal divertor configuration.

1.3.1 Limiter configurations

The concept of limiter SOL is rather simple and was the first method used to shield the main chamber of the reactor from the hot core plasma. A limiting solid surface, i.e. the 'limiter', is inserted inside the plasma chamber by divining the plasma volume in the closed confined region and in the SOL, thus defining the LCFS. Therefore, the limiter is in close proximity to the edge plasma, the narrow region just inside the LCFS, and the impurities released from the surface can directly enter the core plasma; as a consequence, there is a drastic negative effect on the plasma performances and even a termination of the discharge.

1.3.2 Divertor configurations

A different approach is used in the so called poloidal divertor configuration, shown in figure 1.6. Differently from the limiter case, the LCFS is obtained by acting directly on the magnetic field by means of additional current coils: a null of the magnetic poloidal field, i.e. the X-point, is generated. In addtion, the surface that encloses the

closed field line region (i.e. the core) is called separatrix and is indicated in figure. The SOL plasma is diverted towards the target plates. As can be seen, the domain is split in three different regions: the core region (i.e. the region of closed magnetic surfaces), the SOL and the private plasma (PFR, the region inside the separatrix below the X-point). Also shown are the target plates and the strike points, namely the point where the separatrix hits the targets. Clearly, the plasma wall interaction (the target plates) are located away from the LCFS. The main drawbacks are related to the cost, size and complexity.

The main advantages related to the divertor configuration are:

- the increase in the near target plasma compression with positive effect on the particle exhaust and pumping efficiency since a colder and denser plasma than in the limiter case can be obtained;
- reduction in the material erosion and in the impurity source;
- reduction in the impurity and neutral penetration in the core plasma with positive effect on the plasma core contamination (lower Z_{eff}) and on the plasma performances;
- achievement of the detachment regime (see section 1.3.3) where a cloud of neutral forms in front of the target preventing damages and reducing the sputtering of the target material;
- appearance of a robust H-mode at high sufficiently power level.

In addition, the change in the magnetic topology with a decrease of the local poloidal magnetic field has a direct effect on plasma wetted area A_{wet}:

$$A_{wet} = 2\pi R_t f_x \lambda_q, \tag{1.8}$$

where f_x is the flux expansion. This key parameter is realted to geometrical aspect since the magnetic flux near the X-point and on the target must preserve leading to a flaring of the flux surfaces with respect to the equatorial plane. It is defined as the ratio of the distance between two flux surfaces at the target, l_t, and at the outer-midplane, l_u [3]:

$$f_x = \frac{l_t}{l_u} = \frac{(B_p/B)_u}{(B_p/B)_t}. \tag{1.9}$$

Furthermore, there is an increase in A_{wet} since the attack angle of the field line on the target is related to B_p. As a result, the parallel power flow on the divertor plates must be corrected by the term $sin(\gamma) = (B_p/B)$, hence on the target we have:

$$q_t = \frac{P_{sep}/2}{2\pi R_t \lambda_q f_x}, \tag{1.10}$$

where for simplicity we have considered P_{sep} equally distributed between inner and outer plates. Nowadays, the divertor is the most used configuration in the present tokamak devices and the ones that will be adopted in ITER.

1.3.3 Plasma edge Physics

The power loads on the divertor plates are strictly related to the geometry and to the thickness of the SOL which is determined by the competition between perpendicular (i.e. radial direction) and parallel (i.e. along the field line) transport. As a first approximation, we can consider that collisional transport theory predicts that the heat flows in the two directions are ordered by[12]:

$$q_{\parallel} : q_{\perp} = 1 : \left(\frac{\nu_s}{\omega_c}\right)^2, \tag{1.11}$$

where ν_s and ω_c are the collisional frequency and gyro-frequency (eq. 1.4) , respectively. Since one of the conditions defining a strong magnetized plasma is $\nu_s/\omega_c \ll 1$, the perpendicular heat flow is much lower than the parallel one and this is the reason for the thin and strongly elongated shape of the SOL. However, while the parallel transport is mainly classical and well understood, the cross-field transport is anomalous and dominated by turbulence. Therefore, the SOL transport features can be identified by prescribing diffusion coefficients for particles and energy, $D_{\perp}$ and χ respectively; we can equivalently define the radial e-folding length λ_q, which refers to the exponential decay of the power flow into the SOL, or λ_{int}, which also takes into account the diffusion into the PFR.

Empirical scalings on JET and ASDEX [13] have shown that λ_q is barely independent on the machine size while it is strongly affected by the magnetic field; it is of the order of few millimeters for JET, ITER and DEMO. Taking also into account that A_{wet} is proportional to the machine size, we can use P_{sep}/R as a figure of merit of divertor conditions in the different devices. $P_{sep}/R = 14MW/m$ is foreseen for ITER, while $P_{sep}/R = 17 \div 23MW/m$ for DEMO, considering the uncertainty related to the design. For the proposed satellite tokamak DTT a value of $P_{sep}/R = 14 \div 17MW/m$ has been chosen during the design phase in order to study divertor conditions close to DEMO and to achieve the main goals of the proposed studies.

In order to better understand the physics phenomena characterizing the SOL we should consider the parallel transport. Furthermore, the presence of a solid wall implies the recombination of ions at the target plates and the presence of a sheath and a magnetic pre-sheath, which set up due to the mass difference between ions and electrons and where the Bohm-Chodura criterion $M_{se} \geq 1$ holds, being $M_{se} = v_{i,//}/c_s$ the Mach number given by the ratio of the ion velocity over the sound speed $c_s = \sqrt{(n_e T_e + T_j \sum_j n_j)/\sum_j m_j n_j}$. Qualitatively, we have that the

edge physics is strictly related to the different values of the upstream collisionality $\nu_u^* \propto qRn_u/T_u^2$[12]. By varying the latter parameters, for example by increasing the upstream density $n_{e,LCFS}$, we can distinguish different cases where the conduction and convection heat fluxes play a different role and where the downstream (or target) variables (n, T, Γ) are differently related to the upstream ones. Depending on the value of ν_u^* we have three main different regimes:

- for low collisionality ($\nu_u^* \ll 30$) we have the *sheat limited* (or *low recycling*) regime where both temperature and pressure are roughly constant along the magnetic field and the power outflow is dominated by the electrostatic sheath. T_t are quite high ($T_t > 10eV$) and n_t increase nearly linearly with the n_u. In this case the atomic interactions between plasma and recycled neutrals are ineffective in removing momentum and energy from the plasma itself;

- for intermediate collisionality ($\nu_u^* \sim 30$) we get the *conduction limited* (or *high recycling*) regime, where the pressure remains constant but large temperature gradients set in because of the reduction in the parallel heat conduction. In this case n_t increase at least quadratically with n_u. Clearly, higher is the outflux, higher is the neutral inflow rate and one eventually reach a steady state condition where the outflux is matched by the recycled neutral flux, hence the name *high recycling*. Because of the T_t drop and the appearance of a high near-target recycling region, the volume losses change but most of power, carried by convection, still reaches the target; therefore, we have no effect on the global power balance and on the power exhaust issue;

- for high value of ν_u^* one find the so called *detached* regime. Increasing the upstream density beyond the typical value of the *high recycling* regime, the T_t drops below $5eV$ and the ionization rate dramatically drops. As a consequence, there is a decrease in n_t and Γ_t due to the strong recombination occurring in the near target region with a 'detachment' of the plasma flame from the target. Since neutral particles are subject to several charge exchange (CX) processes before being ionized, there is a loss of momentum and energy from the plasma which results in a pressure drop along the flux tube and in an increase in the volumetric losses via radiation and CX. Therefore, the characteristic marker of the detachment are the 'roll-over' of n_t and Γ_t (and also of the saturation current measured by the Langmuir probe j_{sat}) with increasing n_u, $T_t < 5eV$ and the pressure drop along the flux tube.

Figure 1.7 shows the different regimes as a function of the averaged bulk density $\bar{n}_u$ for the ASDEX tokamak[14]. Starting form the left, we can clearly observe the transition from the *sheat limited* to the *conduction limited* regime, characterized by the drop in the T_t (both ions and electron) and the change in the dependence of n_t on $\bar{n}_u$. On the right, the typical signal of the detachment are present, since the

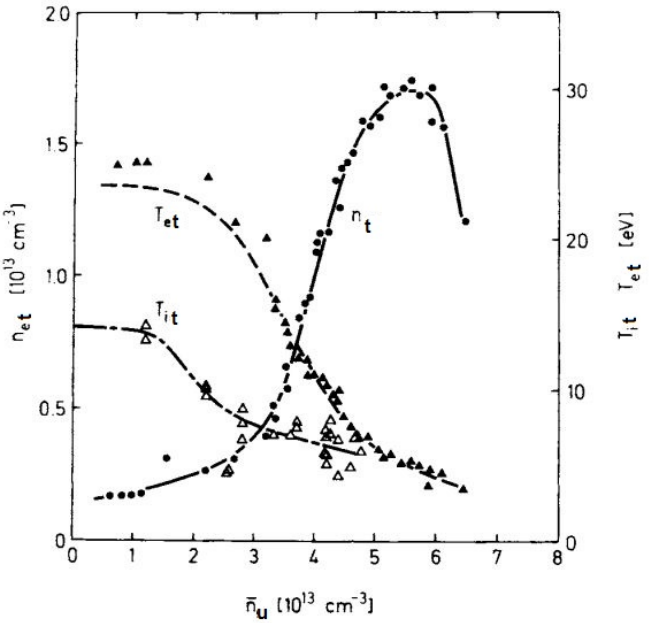

Figure 1.7: Target temperature (T_{et} and T_{it}) and density (n_{et}) as a function of the bulk plasma density ($\bar{n}_u$) for the three different divertor regimes in the ASDEX tokamak (1983). It is clearly visible the 'roll-over' point of n_t[14].

fall of T_t below 5 eV and the 'roll-over' of n_t are clearly visible. However, a remark should be made about the detachment: the definition *'partial detachment'* is more appropriate when there is the transition from high recycling to detached regimes. In this case the roll-over of the ion flux (and of n_t) and the pressure drop is observed only in the proximity of the separatrix where the temperature falls below $T_e < 5eV$. As the detachment evolves, the plasma flame detaches all along the target and the temperature drops to $T_e < 2 - 3eV$. In this case a fully (or total) detachment state is achieved.

For reactor relevant scenario, as DEMO, the detachment condition are mandatory for two main reasons. On one hand, the $T_{e,t} < 5$ eV is necessary due the erosion of the target material. In particular, this limit is related to the sputtering of the solid surface by the plasma that reaches level compatible with the 2 years lifetime of the divertor below the $5eV$ threshold [15]. On the other hand, we have to consider that in case of H-mode, the power crossing the separatrix has a lower limit defined by $P_{sep} = 150 \div 200 > P_{LH}$[10],[16]. If we consider a major radius of $R = 9m$ and a dacay length $\lambda_{int} \sim 3mm$ (cf. section 3.1), the deposition area is $A \sim 4$ m^2. Moreover, taking into account that in stationary conditions a limit on the maximum power density $P_{max} = 5 \div 10$ MW/m^2 is imposed by the technology, it is clear that most of the power in the SOL must be radiated before reaching the divertor plates.

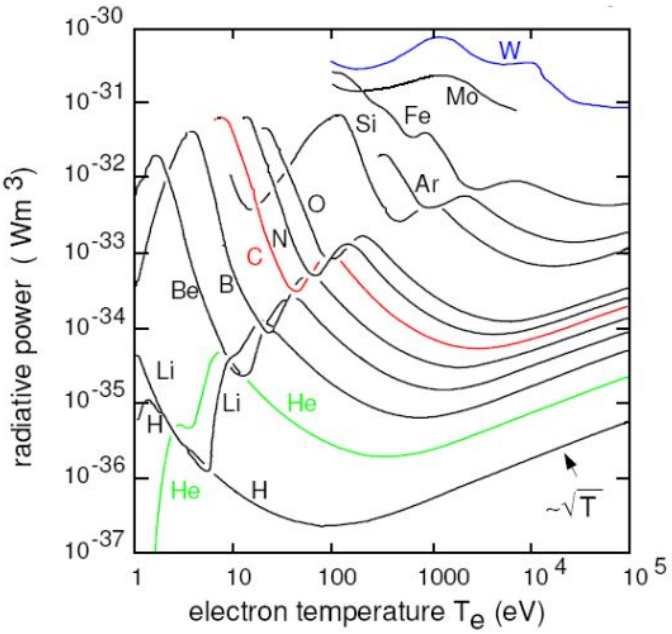

Figure 1.8: Radiation power function vs electron temperature for different elements in corona equilibrium [17].

Therefore, the volumetric losses, $P_{rad} > 80\% P_{sep}$, plays a vital role. In order to reach such level of radiation one can insert external impurities. A first estimate of the radiative power of the different impurities can be done by observing figure 1.8, where the radiative power as a function of the electron temperature in corona equilibrium is shown. We can see that light elements, e.g. Carbon or Nitrogen, are suitable for edge radiative cooling since the maximum of the radiative power is located in a temperature range compatible with SOL, while heavier elements, as Tungsten or Argon, radiates mainly in the core region: one should consider the possible negative effect that the different elements could have on the core plasma performances related to the core radiation and fuel dilution. Therefore, the study of these highly radiating, impurity seeded scenarios is a crucial aspect to investigate for future fusion reactors in terms core performance compatibility and SOL conditions. Since of the complexity of the problem, these analyses are made by using numerical edge codes (described in chapter 2) in order to better understand the physical mechanisms and the possible benefits deriving from the different possible solutions that could be adopted.

1.4 Alternative Divertor Configurations

The baseline scenario for a future DEMO reactor is currently based on the baseline divertor solution of ITER. However, because of the hard divertor conditions in terms of power fluxes and particle and neutron fluence, there is the possibility that this scenario does not extrapolate from ITER to DEMO. In order to mitigate this risk, the EUROfusion consortium is assessing different alternative divertor solutions that are based on two main mechanisms:

- an increase in the power radiation in the SOL or divertor region by changing the magnetic divertor topology. This solution is referred to as '*Advanced magnetic divertor configurations*' and is based on the idea that a modification of the poloidal magnetic field either near the target or in the proximity of the X-point region, e.g. by creating a second null point, can enhance the radiative performance of the SOL plasma;
- an increase of the tolerable heat load of the divertor component by changing the target material, e.g. by using liquid metal in place of W.

We can therefore analyze in details the possible alternative solutions, highlighting the possible benefits and physical mechanisms that could help to tackle the power exhaust issue.

1.4.1 Advanced magnetic divertor configurations

Several advanced magnetic divertor configurations has been proposed. In figure 1.10 we show a X divertor, a Super X divertor and a Snowflake (SF) divertor. The difference from the standard Single Null (SN) configuration stems in a change of the magnetic poloidal field and the presence of a second order or second null point of B_p. This characteristic is generally obtained by using a set of divertor coils, which increase the complexity of the poloidal field coils system.

X divertor

The X divertor [18] was introduced in 2004 and is characterized by the presence of a second null point in the target region, as can be seen in figure 1.9a. As a consequence, there is a flaring of the flux surfaces near the divertor plates and an increase both in divertor volume and in connection length $L_{\parallel}$, which is generally defined as half of the distance between two points of contact with the solid surface. The change in the magnetic field is generally obtained by using dedicated divertor coils. The increase in the wetted area, related to the increased in f_x, and the increase in $L_{\parallel}$ could result in a reduced peak heat flux and also in a drop of the plasma temperature that could lead to detachment at lower density.

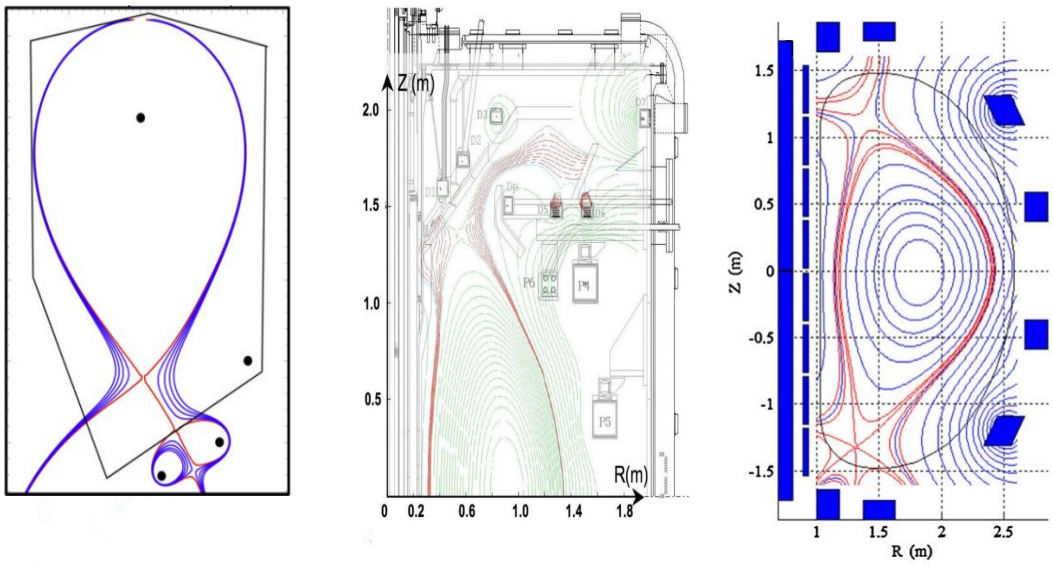

(a) (b) (c)

Figure 1.9: Scketch view of three different advanced magnetic configurations: (a) X divertor (XD) [18], (b) Super X divertor (SXD)[19] and (c) exact snowflake divertor (SF)[20].

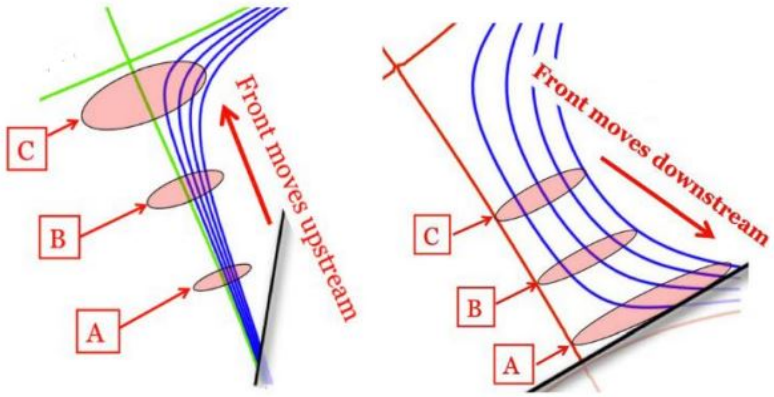

(a) (b)

Figure 1.10: Movement of a detachment front in (a) contracting SN geometry and in (b) flaring XD geometry. The reduction of the contact area in XD has a stabilizing effect on the movement of the detachment front.[18].

Most importantly, the flaring of the flux surface could introduce a stabilizing effect on the movement of the detachment front. As shown in figure 1.10a, in case of a standard SN configuration, the detachment front tends to move upstream towards the X-point, since the contact area increase in this direction. In particular, if the

energy losses increases the neutrals tends to move towards the heat source, that is the plasma. This movement could cause a 'radiation condensation instability', the so called $MARFE$, and eventually a termination of the plasma discharge. Conversely, in case of an XD (figure 1.10b) the contact area decreases by moving towards the X point, because of the flaring of the flux surfaces. As a results, there is a positive feedback that tends to localize the detachment in front of the divertor plates.

Super X divertor

The Super X divertor [19] (figure 1.9b), introduced in 2007, exploits the increase in the major radius of the target plates R_t to increase $L_{\parallel}$ and A_{wet}. In addition, this concept is combined with an increase of the flux expansion as in the XD configuration, hence the name '$Super - Xdivertor$'. It is worth noting that there is a reduction of the parallel heat flux $q_{\parallel}$ towards the target because of the larger cross sectional area corresponding to the increase in R_t. This feature could have strong effect on the sheath temperature, which is tightly related to $q_{\parallel}$. Therefore, the presence of a negative gradient could increase the robustness of the detachment.

Snowflake divertor

The SF [20] divertor was introduced in 2007. A second order null at the main plasma X-point is created by a set of poloidal coils that give rise to a six-fold symmetry in the divertor region as can be seen in figure (1.9c)[20]. This shape gives the name Snowflake to this magnetic configuration. Differently from the SN characterized a linear increase of B_{pol} with the distance from the X-point, the presence of a second order null implies a quadratic dependence on the distance that, in turn, entails an increase in the divertor volume, in the flux expansion in the vicinity of the X-point region and in the connection length $L_{\parallel}$ between the equatorial plane and the target. Unlike the XD, the SF is characterized by contracting flux surface in the target region.

However, the SF is topologically unstable and any real configuration is characterized by the presence of two nearby null points. The first null point defines the separatrix and the primary strike points. The second null point can be located either in the PFR or in the common flux region, generating a Snowflake plus (SF+) and Snowflake minus (SF-), respectively. If the secondary X-point approaches the target, there is a transition from SF to XD and this configuration is referred to as Quasi-Snowflake (QSF)[21].

An important effect of the change in magnetic topology is the possible increase of the cross-field transport. Since the region close to the X-point is characterized by a high value of $\beta_p = 8\pi p/B_p^2$, because of the low value of B and the still high value of p, a '*churning*' mode could arise increasing the convection in this region. A simple sketch is shown in figure 1.11. The origin of this convection mechanism

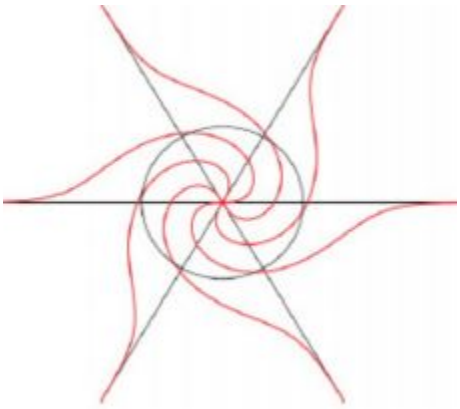

Figure 1.11: Sketch of a '*churning mode*' driven by the low B field and by the still high value of p. This mode entails an increase in the cross-field transport[20].

is similar to a boiling fluid in a box heated by a side wall. The fluid expands and, driven by the buoyancy force, start to flow upward and a convection cell appears. Likewise, in the X-point region, the gravity force is in the radial direction, while the vertical gradient pressure play the role of the side wall heating [20]. This effect could be beneficial for the power sharing and could decrease the peaks power on the target plates.

The geometrical effect related to the change in magnetic topology and the increase in $L_{\parallel}$ that could results in an increase in the radiative performance of the SOL plasma can represent a possible solution for the power exhaust issue. A strong effort is than necessary in simulating reactor conditions similar to DEMO scenario by using the current available edge code (described in chapter 2). On one hand, we can use codes largely and robustly validated in the past, as in case of EDGE2D-EIRENE (described in section 2.3.1), to predict the SOL plasma conditions in DEMO relevant scenarios. In chapter 3 an analysis of the the DEMO baseline scenario is initially performed. In addition, a benchmark of EDGE2D-EIRENE and TECXY (section 3.1.4) will be discussed, analyzing the causes of the differences obtained in the two calculations and highlighting the benefits deriving from the use of each code. On the other hand, a validation of the code is necessary by benchmarking the numerical results with the experimental data. This is the main focus of chapter 4, where the results obtained with the SOLEDGE2D-EIRENE (section 2.3.3)code will be compared with the experimental data of a JET experiment. Sensitivity analysis on different input variable will be performed, as for the diffusion coefficients $D_{\perp}$ and χ and for the recycling coefficient R_c.

1.4.2 Liquid metal as Plasma Facing Component

A different approach to tackle to power exhaust problem is based on the idea of changing the properties of the target material, that is to switch from a solid material, as W in ITER scenario, to liquid metal surfaces. A liquid can support high power fluxes due to the high heat conduction and the possibility to exploit different heat transfer mechanisms, namely the convection and the vaporization. However, if one would exploit the movement of the liquid to carry heat power by means of convection, one must ensure the stability of the moving liquid itself in a varying strong magnetic field. Some test performed on T10 and ISTOK showed the difficulties to work in these operational conditions[22], [23]. Therefore, the most promising techniques are based on static liquid metals that exhaust power through conduction.

The system used to confine the liquid metal are the so called Capillary Porous System (CPS). They are based on the idea that a porous structure, made of a mesh, felt or porous solid and wetted by a liquid metal, provides the capillary force able to counteract $J \times B$ force that tends to splash the liquid metal droplets throughout the plasma volume. The wetting of the mesh plays a pivotal role in the CPS since a good wetting ensure the capillary forces and the refilling of the lost material. This condition has been verified and tested in T11 tokamak equipped with a Lithium Limiter CPS [24]. The CPS can than be integrated in a more complex system where one can provide a cooling system (e.g. with water or gas) and a reservoir of liquid metal in order to ensure the replenishment of eroded material.

An important mechanism that generates in case of liquid metal is the so called '*vapor shielding*'[25]. When a high heat flux arrives on the target plates, the presence of a liquid and the sudden increase in temperature results in a strong increase in the evaporation of the liquid itself. Therefore, a shielding layer forms in front of the target that is able to radiate most of the power reaching this area. Eventually, a reduction of the heat power occurs which yields to a reduction of the target temperature and, as a consequence, of the evaporation rate. This feature can be viewed as a self healing mechanism for the divertor in case of high thermal loads, as in case of ELM events, and could protect the surface from further damages.

When one has to choose a suitable liquid metal for the power exhaust in a fusion reactor there are several constraints. The most important criteria to fulfill are:

- plasma compatibility, that is the contamination of the plasma by eroded material should not have a negative effect on the plasma performance both in terms of fuel dilution (in case of low Z elements) or core radiation (in case of high Z elements);
- long term Tritium retention, since the tritium release in the environment is a safety hazard and a possible source of accidents. Therefore, the tritium inventory is ruled by stringent safety law and the total quantity of tritium retained by the liquid metal must be assessed;

- acceptable activation;

Nowadays, lithium (Li) and tin (Sn) are the most promising and the central focus of the fusion worldwide research in the liquid metal context. Recently, several experiments with Cooled Lithium Limiter (CLL) and Sn limiter were performed on FTU (Frascati Tokamak Upgrade) tokamak with promising results in terms of stability of the CPS system under a power flow of 2 MW/m^2 for a 1.5 s discharge[26] with lithium and $18MW/m^2$ with tin [27].

Chapter 2

2D modeling of SOL plasma

The analysis of the SOL plasma is a complex task. The presence of the solid wall directly interacting with the plasma and the corresponding plasma neutral interaction defines the different condistions of the SOL plasma. Several simple models have been developed during the year, such as the two-Point model (well described in [28]). However, in order to perform a deep analysis of the characterstic of the SOL plasma conditions it is advised the use of 2D edge codes. Nowadays, several 2D codes are available in the fusion community. Therefore, a background of the physical model at the base of these codes is essential to better understand the obtained results and, most importantly, it is an essential ingredient in the reliability and correctness evaluation phase.

In this chapter we will give an introduction of the physical model that is the base for the 2D edge code that we have used during the PhD research activity. These codes can be viewed as a combination of two different parts which continuosly interact each other. A multi fluid plasma code, that is generally based on the Braginskii's equation[29], is used to describe the evolution of the ions, (both hydrogen isotopes and impurities) and electrons; this part of the code is coupled with another one for the neutral particles description. Indeed, a strong link exists between the two since the quantities calculated from the multi fluid code (as n, T, etc.) represent an input for the neutral part, while the latter gives the sources to the multi fluid code.

Initially, the derivation of the Braginskii's equation is presented, by following the methodology adopted by [29][30]. Starting from the most general kinetic equation we will derive the basic conservations equations solved by the different codes. The treatment of the neutral particles is discussed in section 2.2. In particular, different possible descriptions will be discussed: the analytical, the fluid and the Monte Carlo appraoch. Finally, an overview of the different available code currently present in the fusion community will be given, by highlighting the characteristics and the main advantages and drawbacks of them.

2.1 Braginskii's equations

The Braginskii's equations are a set of partial differential equations that describes the plasma evolution and, in particular, a set of conservation laws for electrons and different ion populations. These equations were first obtained by Braginskii in the famous article in 1965 [29].

2.1.1 Boltzmann equation

Let's start by considering the equation in phace space:

$$\frac{\partial F_s}{\partial t} + \mathbf{v} \cdot \nabla F_s + \mathbf{a}_s \cdot \nabla_v F_s = 0, \tag{2.1}$$

that describes the evolution of the full distribution function F_s for a general plasma species s. The particle accelaration is naturally given by the Lorentz force divided by the particle mass $\mathbf{a}_s = e_s/m_s(\mathbf{E} + \mathbf{v} \times \mathbf{B})$, where the $\mathbf{E}$ and $\mathbf{B}$ fields are given by Maxwell's equations. Even if eq. 2.1 seems a simple formula, in a tokamak reactor it is not practicable to use since we have to consider the trajectory of each particle, that means eq. 2.1 is given by the sum of Dirac delta functions. Therefore, we need to apply an ensamble average, by considering a smoothed distribution function $f_s = \langle F_s \rangle_{ensamble}$. It is important to note that due to the interdependence between the particles trajectories and the $\mathbf{E}$ and $\mathbf{B}$ fields, we introduce the collisional operator $C_s(f)$ in order to take into account the correlations related to the Coulomb collisions occuring between plasma species. Eventually, the evolution of f_s can be written as:

$$\frac{\partial f_s}{\partial t} + \mathbf{v} \cdot \nabla f_s + \mathbf{a}_s \cdot \nabla_v f_s = C_s(f), \tag{2.2}$$

which is the so called Boltzmann (or kinetic) equation.

2.1.2 Moments of the distribution function

The description of the plasma can be performed by considering more intuitive physical quantities which can be obtained by averaging the distribution function. In other words, we can obtain the density n_s, flow velocity $\mathbf{V}$, the stress tensor $\mathbf{P}_s$ and the energy flux density $\mathbf{Q}_s$ by calculating the zero and the first three order moments of the distribution function:

$$n_s(\mathbf{r},t) = \int f_s(\mathbf{r},\mathbf{v},t)d^3\mathbf{v}, \tag{2.3a}$$

$$\mathbf{V}_s(\mathbf{r},t) = \frac{1}{n_s}\int \mathbf{v} f_s(\mathbf{r},\mathbf{v},t)d^3\mathbf{v}, \tag{2.3b}$$

$$\mathbf{P}_s(\mathbf{r},t) = \int m_s \mathbf{v}\mathbf{v} f_s(\mathbf{r},\mathbf{v},t)d^3\mathbf{v}, \tag{2.3c}$$

$$\mathbf{Q}_s(\mathbf{r},t) = \int \frac{1}{2} m_s v^2 \mathbf{v} f_s(\mathbf{r},\mathbf{v},t)d^3\mathbf{v}, \tag{2.3d}$$

One can note that the second and third order moments, which are defined in the laboratory rest frame, represents the flow of momentum and the flow of energy. It is useful to define these two quantities in framework moving with the species under considerations. Once introduced the relative velocity:

$$\mathbf{v}' = \mathbf{v} - \mathbf{V}_s, \tag{2.4}$$

we get the new expressions:

$$\mathbf{p}_s(\mathbf{r},t) = \int m_s \mathbf{v}'\mathbf{v}' f_s(\mathbf{r},\mathbf{v},t)d^3\mathbf{v}, \tag{2.5a}$$

$$\mathbf{q}_s(\mathbf{r},t) = \int \frac{1}{2} m_s v'^2 \mathbf{v}' f_s(\mathbf{r},\mathbf{v},t)d^3\mathbf{v}, \tag{2.5b}$$

where the moments $\mathbf{p}_s$ and $\mathbf{q}_s$ are respectively called pressure tensor and heat flux density and are directly related to the thermal motion of the specie s. Moreover, the pressure tensor can be further split in two different components:

$$\mathbf{p}_s = p_s \mathbf{I} - \boldsymbol{\pi}_s, \tag{2.6}$$

where the first term p_s on the right hand side is the *scalar pressure* and correspond to 1/3 the trace of $\mathbf{p}_s$, whereas the second term $\boldsymbol{\pi}_s$ is the *generalized viscosity tensor* and is related to the anisotropy in the distribution function. For a Maxwellian distribution, that is at thermal equilibrium characterized by a temperature T_s, the only term is the scalar pressure and $p_s = n_s T_s$ since the the scalar pressure is simply 2/3 of the kinetic energy of the species s:

$$p_s = \frac{2}{3}\int \frac{1}{2} m_s v'^2 f_s d^3\mathbf{v}. \tag{2.7}$$

Finally, by direct substitution of eqs. 2.4 in eqs. 2.5, one can find the relationships between the moments $\mathbf{p}_s$ and $\mathbf{q}_s$ and the ones evaluated in the rest frame of the laboratory given by:

$$\mathbf{P}_s = \mathbf{p}_s + m_s n_s \mathbf{V}_s \mathbf{V}_s, \tag{2.8a}$$

$$\mathbf{Q}_s = \mathbf{q}_s + \mathbf{p}_s \cdot \mathbf{V}_s + \frac{3}{2} p_s \mathbf{V}_s + \frac{1}{2} m_s n_s V_s^2 \mathbf{V}_s \mathbf{p}_s. \tag{2.8b}$$

2.1.3 Moments of the collision operator

The collision operator introduced in eq. 2.2 is related to the effect of the Coulomb collisions, which are long range interactions. As a consequence, the effect on a particle is a many-body problem related to the Debye shielding. Nonetheless, $C_s(f)$ can be considered bilinear, that is it describes the change in f_s due to the interaction with particle s':

$$C_s(f) = \sum_{i=0}^{n} C_{s,s'}(f_s, f_{s'}). \tag{2.9}$$

The moments of the collision operator therefore express a change in a quantity related to Coulomb collisions.

The zero order moment expresses the variation of the particle amount due to collisions. Clearly, it must be zero since the interaction of particle of two different species cannot change the total number of particles:

$$\int C_{s,s'} d^3\mathbf{v} = 0. \tag{2.10}$$

However, in case of cold plasma and in presence of a non negligible neutral population, the inelastic collisions (e.g. ionization, recombination) should be taken into account and an extra source term $S_{n,part}$ should be added.

The first moment represents the force $\mathbf{R}_{s,s'}$ exerted on particle s due to the collision with particle s':

$$\mathbf{R}_s \equiv \sum_{s \neq s'}^{n} \mathbf{R}_{s,s'}, \tag{2.11a}$$

$$\mathbf{R}_{s,s'} \equiv \int m_s \mathbf{v} C_{s,s'} d^3\mathbf{v}. \tag{2.11b}$$

For momentum conservation, the global exchange between two particle species is zero, that is $\mathbf{R}_{\mathbf{s},\mathbf{s}'} = \mathbf{R}_{\mathbf{s}',\mathbf{s}}$. The transfer of momentum can be divided in two different parts. The first one is the *friction force* that originates from the difference in velocity of the two colliding particle species. The second one is due to the presence of temperature gradient and is called *thermal force*. In addition, an extra term $\mathbf{S}_{n,mom}$ is necessary because of the presence of neutrals.

Finally, the second order moment defines the variation in the internal energy due to Coulomb collisions:

$$W_s \equiv \sum_{s \neq s'}^{n} W_{s,s'}, \tag{2.12a}$$

$$W_{s,s'} \equiv \int \frac{1}{2} m_s \mathbf{v}'^2 C_{s,s'} d^3\mathbf{v}, \tag{2.12b}$$

where the integral is calculated in the rest frame of the specie s. By using eq. 2.4, can be easily demonstrated that:

$$W^L_{s,s'} = W_{s,s'} + \mathbf{V}_s \cdot \mathbf{R}_{s,s'} \tag{2.13}$$

where the apex L stays for the laboratory rest frame. Obviously, in presence of neutrals and in case of cold plasma extra terms are needed to take into account the source or sink of energy due to plasma neutrals interaction $S_{n,en}$. Furthermore, for the electrons there is also an additional term $S_{e,rad}$ to take into account the radiation emission.

2.1.4 Moments of kinetic equation: Conservation laws

A fluid approach can be used to describe the plasma evolution, rather than using the Boltzmann's equation 2.2. The balance equations can be obtained by performing the moments of eq. 2.2, that is by multiplying by 1, $m_s\mathbf{v}$ and $1/2m_sv^2$ and integrating over all the velocity space. In addition, we should also consider the presence of neutral particles and the corresponding source terms for particles, momentum and energy.

The zero order moments gives the continuity equation:

$$\frac{\partial n_s}{\partial t} + \nabla \cdot (n_s \mathbf{V}_s) = S_{n,part}. \tag{2.14}$$

This equation simply states that the variation of the particle density is due to a net flux, corresponding to the divergence of the flux $n_s\mathbf{V}_s$, and to a sink or source of particles in the volume, given by the source term $S_{n,part}$.

Taking into account eqs. 2.6 and 2.8a and performing some algebra, the conservation of momentum is obtained by the first order moment of eq. 2.2 :

$$m_s n_s \frac{d\mathbf{V}_s}{dt} + \nabla p_s + \nabla \cdot \boldsymbol{\pi}_s - e n_s \left(\mathbf{E} + \mathbf{V}_s \times \mathbf{B}\right) = \mathbf{R}_s + \mathbf{S}_{n,mom}, \tag{2.15}$$

where we use the total derivative:

$$\frac{d}{dt} \equiv \frac{\partial}{\partial t} + \mathbf{V}_s \cdot \nabla. \tag{2.16}$$

In the balance equation we can recognize the different terms that cause the change in the momentum. There is a change in the momentum due to the pressure gradient and to the viscous term, that represents a momentum flux, to the Lorentz force and to the collision between particle species. Finally, the source term defines the rate of generation of momentum due to the neutral plasma interaction.

Finally, in order to get the conservation of energy we perform the second order moment of the kinetic equation. We get:

$$\frac{\partial}{dt}\left(\frac{3}{2}p_s + \frac{1}{2}m_s n_s V_s^2\right) + \nabla \cdot \mathbf{Q}_s - e n_s \mathbf{E} \cdot \mathbf{V}_s = W_s + \mathbf{R}_s \cdot \mathbf{V}_s + S_{n,en} + S_{e,rad}. \quad (2.17)$$

From the latter formula, we can see that the energy, given by the sum of internal energy $3/2p_s$ and of the kinetic energy $1/2m_s n_s V_s^2$, changes due to the energy flux ($\nabla \cdot \mathbf{Q}_s$), the electrical work, the interaction between plasma species and frictional heating. In addition, also the source term has been taken into account, where the radiation term holds for electrons only. Bearing in mind expressions 2.7 and 2.8b, we can derive the energy balance in terms of internal energy by means of the continuity equation and momentum balance. Eventually we have:

$$\frac{3}{2}\frac{dp_s}{dt} + \frac{5}{2}p_s \nabla \mathbf{V}_s^2 + \boldsymbol{\pi}_s : \nabla \mathbf{V}_s - \nabla \cdot \mathbf{q}_s = W_s + S_{n,en} + S_{e,rad}. \quad (2.18)$$

Eqs. 2.14, 2.15 and 2.18 are the so called Braginskii's equations, where we also consider the extra source terms related to the plasma neutral interactions. These are the physics basis for the plasma description in the 2D edge codes we have used during the PhD research activity; in these codes, different assumptions and different numerical schemes are used to solve the transport equations. Hereafter, a discussion on these topics will be given together with a description of the main characteristics of each code.

2.2 Neutral description

The presence of neutral particles plays a vital role in the plasma edge physics and in some cases could dominate the plasma dynamics, as in case of the detached regime. The source terms of the particles, momentum and energy in the Braginskii's equations are generally extracted from a dedicated module for neutral description which takes as input the main physical quantities (e.g. n, T, etc.) of the background plasma. It is then crucial to have an insight into the physical models used in the different 2D edge codes in order to better evaluate the effects of neutrals and to decide the most suitable one related to the different situations to study. In other word, the knowledge of these models allows to define the range of applicability and reliability of the different descriptions. An example of this kind of analysis and of how the neutral description affects the output of the simulations is given in section 3.1.4 where we perform a benchmark of two numerical tools using two different neutral models.

When a neutral enters the plasma as a consequence of the recycling or of the external puff, it can undergo several processes, which are listed in table 2.1. We point out that the main reactions taken into account in the different descriptions are the charge exchange (CX), the recombination and the ionisation. In addition,

Table 2.1: Main reactions that can occur in the neutral plasma interaction process.

Name	Reaction
Ionisation	$\mathrm{D} + e \rightarrow D^+ + 2e$
Charge Exchange	$\mathrm{D} + D^+ \rightarrow D_+ + \mathrm{D}$
Radiative recombination	$D^+ + e \rightarrow \mathrm{D} + h\nu$
3 - body recombination	$D^+ + 2e \rightarrow \mathrm{D} + e$
Dissociative recombination	$D_2^+ + e \rightarrow 2\mathrm{D}$
Dissociative exitation	$D_2^+ + e \rightarrow \mathrm{D} + D^+ + e$
Dissociative ionisation	$D_2^+ + e \rightarrow 2D^+ \; e$

we do not take into account the neutral- neutral reaction since it can be generally neglected, except for high value of neutral density.

2.2.1 Analytical and fluid models

Among the different approaches used to simulate the neutral dynamic in a fusion reactor, the simplest model assigns an analytical function that describes the 2D distribution of the neutral density. An example is given in [31]. The neutral dynamics is described in a self-consistent way accounting for the recycling of deuterium and the sputtering and self-sputtering of the impurities. As far as the deuterium is concerned, the neutrals are divided in two different groups, i.e. fast N_D^f and slow N_D^s, since the different cross sections of the reaction listed in table 2.1 depends on the velocity $v_{Dx,y}$. The 2D profile of the density depends on the position of the plate x_{plate}, on the point of neutral maximum reflux form the target y_M and on the cross section of ionisation α_i^D and charge exchange α_{CX}^D processes taken into account by defining the two mean free paths:

$$\lambda_{x,y}^f = \frac{v_{Dx,y}^f}{n_e\sqrt{\alpha_i^D \alpha_{CX}^D}}; \lambda_{x,y}^s = \frac{v_{Dx,y}^s}{n_e\sqrt{\alpha_i^D}}. \tag{2.19}$$

The planar distribution of the neutral density is then prescribed by a combination of two exponential functions and given by:

$$N_D^{f,s}(x,y) = N_{plate}^{f,s} \exp\left(-\frac{|x_{plate} - x|}{\lambda_x^{f,s}}\right) \exp\left(-\frac{(y_M - y)^2}{\lambda_y^{f,s}}\right), \tag{2.20}$$

where the target neutral densities for fast and slow groups, respectively $N_{plate}^f = 3/4\ N_{plate}^D$ and $N_{plate}^s = 1/4\ N_{plate}^D$, depend on the recycling coefficient R given by:

$$\int_{VOL} N_D^{f,s}(x,y)\alpha_i^D(x,y)n_e(x,y)dV = R\int |n_i v_x^i|(X_{plate,y})dS. \tag{2.21}$$

For the calculation of the reaction rate of the two neutral groups different temperature are imposed. For the fast neutral the temperature is obtained by imposing an equilibrium with plasma ions as a consequence of the charge exchange and ionisation processes. For the slow ones the temperature is given by the Frank-Condon energies of about 2 eV. The expression for the impurities is similar to that of D in eq. 2.20, but with N^Z_{plate} defined by the sputtering yields Y_D and Y_j related to deuterium or to the impurity, respectively.

This model is the fastest and the least computational time demanding. However, the neutral conditions are quite approximated; as a result, situations where neutrals play an important role in defining the plasma conditions, e.g. in detached regimes, are not properly described and a more detailed description is needed.

A second approach is based on a fluid description of the neutral particles. This model assume that the neutral density evolution is governed by diffusive processes. Details on this model are given for example in [32]. The continuity equation can be written as:

$$\frac{\partial n_n}{\partial t} - \nabla \cdot (D_n \nabla n_D) = S_n(n_n), \tag{2.22}$$

where, as in case of eq. 2.14, the variation of the neutral density is related to a net flux, namely a diffusion of particles, and a volumetric source. The latter term is related to the ionisation governed by the corresponding reaction rates $\langle \sigma v \rangle_{ei}$:

$$S_n(n_n) = -n n_n \langle \sigma v \rangle_{ei}, \tag{2.23}$$

while the diffusion coefficient is related to the total reaction rate $\langle \sigma v \rangle_{tot}$, which also takes into account other possible reactions as the charge exchange, and given by:

$$D_n = \frac{u_n^2}{3n\langle \sigma v \rangle_{tot}}. \tag{2.24}$$

As a first approximation, the neutral velocity u_n can be simply obtained by considering a one group energy in thermal equilibrium with the background plasma. Naturally, boundary conditions has to be imposed on the surface such that the total particle conservation is respected. We can then write down the following condition:

$$\left[\frac{1-\alpha}{1+\alpha}\right]\left(\frac{n_n u_n}{2}\right) \pm D_n \nabla n_n = S_0, \tag{2.25}$$

where the α is a reflection coefficient, the flux $D_n \nabla n_n$ is outward directed and the source S_0 is inward directed (e.g. the flux related to the recycling of particles and governed by the coefficient R).

Finally, we can obtain the source terms for the continuity, momentum and energy

equations by:

$$S_{n,part} = nn_n\langle\sigma v\rangle_{ei}, \tag{2.26a}$$

$$S_{n,mom,i} \simeq nn_n\langle\sigma v\rangle_{ei} m_n u_{n,d} + nn_n\langle\sigma v\rangle_{CX}(m_n u_{n,d} - m_i u_i), \tag{2.26b}$$

$$S_{n,mom,e} \simeq nn_n\langle\sigma v\rangle_{ei} m_e u_e, \tag{2.26c}$$

$$S_{n,en,i} \simeq nn_n\langle\sigma v\rangle_{ei}\left(E_n + \frac{m_n u_{n,d}^2}{2}\right) + nn_n\langle\sigma v\rangle_{CX}\left[\left(E_n + \frac{m_n u_{n,d}^2}{2}\right) - \left(\frac{3}{2}T_i + \frac{m_i V_i^2}{2}\right)\right], \tag{2.26d}$$

$$S_{e,rad} \simeq nn_n\langle\sigma v\rangle_{ei} E_{ioniz}, \tag{2.26e}$$

where E_n is the averaged neutral energy, $u_{n,d}$ is the neutral fluid diffusion velocity and E_{ioniz} is the electron energy loss related to radiative losses.

2.2.2 Monte Carlo method: EIRENE

In high density regimes, as in case of *high recycling* or *detachment*, the analytical and fluid models are not suited to describe the neutral dynamics since of the short neutral particle mean free path with respect to the typical physical and geometrical length scales. It is therefore necessary a kinetic description of the neutral behaviour; in this context, in the early 1980s the neutral gas transport Monte Carlo code EIRENE has been developed[33], [34].

The EIRENE codes solves the Boltzmann's equation for the neutral particles by using a Monte Carlo procedure. First of all, since the transport phenomena related to neutral particles are short compared to the ones relates to plasma transport, we consider a stationary problem. In addition, we can write the problem in term of the collision density $\Psi(x) = \Sigma_t(x)vf$, where $\Sigma_t(x)$ is the macroscopic cross section. The kinetic equation is then written in the integral form for a stationary problem as:

$$\Psi(x) = S(x) + \int dx'\Psi(x') \cdot K(x' \to x), \tag{2.27}$$

where $S(x)$ is the initial distribution. The term K indicates the transition kernel, which represents the probability to pass from a pre-collision state x' to a post collision state x. This term can be further split in two different components $K = C \cdot T$. C is the collisional distribution and gives the probability that a particle i with velocity v' has undergone a collision event at position r' and reaches the new coordinate v. It is clearly given by the summation over the different collision processes with their own conditional probability $p_k = \Sigma_k/\Sigma_t$. The term T is the transport kernel and represents the motion of particle between two collision events. It is defined by the plasma conditions, the test particle velocity and collision rate from the atomic data. For a more detailed description of the code the reader can refer to [34]. As noted, in order to get the data for the different computation EIRENE is coupled with a fluid

plasma code, where the different plasma parameters are frozen in each EIRENE call. Furthermore, the cross section are extracted from a mixture of Atomic Data and Analysis Structure (ADAS [35]) and AMJUEL [36] databases.

The process described by eq. 2.27 is a Markovian jump process governed by the transition probability K: in this process a transition event depends only on the previous one, i.e. the system has not memory of events that happens before the last collision. This description is well suited to be solved with a Monte Carlo method, as made in EIRENE. More precisely, a set of Markov chains are generated by considering the initial distribution S. Each test particle is followed until is it absorbed or lost form the computational box; this process is governed by the conditional probability K. Eventually, the source terms for the fluid equations can be obtained by calculating the responses R:

$$R = \int dx \Psi(x) g_c(x) = \int dx f(x) g_t(x), \tag{2.28}$$

where the g_c and g_t are the so called $detector functions$. The latter can be chosen depending on the quantity of interest. In particular, in case of sources $S_{n,part}$, $S_{n,mom}$, $S_{n,en}$ due to neutral plasma interactions, g_c and g_t are directly related to the mass, momentum and energy exchange between neutrals and the background plasma in a collision with cross section σ.

The use of a kinetic Monte Carlo codes allows to perform an accurate description of the neutral dynamics by tracking directly the neutrals trajectories; in turn, this feature allows to take into account the actual geometry of the divertor and vessel wall. As a results, the EIRENE code is able to perform a deep analysis on the effect related to a change in the vessel or magnetic configuration, e.g. to study the effect of the increase of the divertor closure. However, the greatest drawback stems in the high computational time which is much longer than the one required by the analytical and fluid model treatment.

2.3 2D edge codes

Since the most general physics model used in the different plasma edge codes has been presented, it is important to discuss their own characteristics. In this section a general description in terms of main assumptions, boundary conditions and overall characteristics for the three different numerical tools (i.e. EDGE2D-EIRENE, TECXY and SOLEDGE2D-EIRENE) used during the PhD research activity will be given, highlighting the main advantages and the main limitation related to them.

2.3.1 EDGE2D-EIRENE

EDGE2D [38] is a multi fluid codes for the treatment of the SOL plasma which solves a simplified version of the Braginskii's equations 2.14, 2.15, 2.18. Toroidal

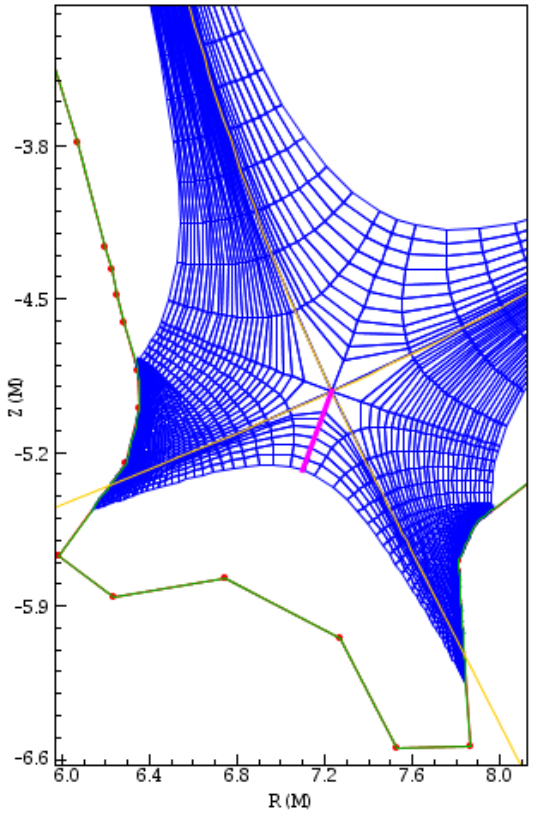

Figure 2.1: Example of a computational mesh used in EDGE2D generated with GRID2D. The mesh cells are aligned with the flux surface. The three different subdomains, that is the SOL region, PFR and core region are visible and divided by the separatrix (yellow line). Finally, the mesh reshaping near the target and the void region between the fluid mesh and vessel are also visible.

symmetry is assumed and the set of conservation laws are written in a curvilinear coordinate system (ρ, θ) in the poloidal plane, where θ is the coordinate along the flux surface, which by convention increases from the outer to the inner target, while ρ is the perpendicular one. The metric coefficients are H_θ and H_ρ such that the arc lengths are given by $H_\theta d\theta$ and $H_\rho d\rho$. As a result, the volume elements and the poloidal arc length are respectively given by:

$$dV = 2\pi R H_\theta d\theta H_\rho d\rho, \tag{2.29a}$$
$$ds^2 = H_\theta^2 d\theta^2 + H_\rho^2 d\rho^2, \tag{2.29b}$$

where R is the major radius.

An example of the mesh used in the EDGE2D calculation is given in figure 3.2.

This mesh is obtained by means of a dedicated mesh generator, i.e. GRID2D[37], developed at JET. The number of the grid points in the radial direction, which defines the number of '*rings*', and in poloidal one, defining the number of '*row*', are external parameters chosen by the user. It is important to point out that a trade-off should be reached between a grid resolution and computational time. For example, in this thesis we adopt the power e-folding length as reference parameter to define a good quality of the grid. As can be seen in figure, the mesh domain also includes the PFR, whose width can be also chosen by the user, and the core region just inside the separatrix. Except from the near target region, where a reshaping of the mesh is performed, the grid does not reaches the vessel wall. Moreover, since EDGE2D is coupled with EIRENE (cf. section 2.2.2), a different mesh for the Monte-Carlo calculation is automatically defined: it is a triangular mesh defined on the fluid grid and between the fluid grid and the vessel wall.

The EDGE2D set of equations written in the (ρ, θ) coordinate system are given in [38]. In particular, the equations solved by the codes are the conservation equations of the mass, momentum and internal energy, that is energy conservation written in the plasma rest frame. The continuity and momentum balance are written for the main ion and for each impurity ion. This means that assumptions are made in the definition of the code equations. First of all, the quasi-neutrality is assumed, i.e. if Z_j is the charge state of a general ion specie j the electron density is given by:

$$n_e = \sum_j Z_j n_j. \tag{2.30}$$

The electron inertia terms are neglected and the parallel electron momentum becomes the Ohm's law used to derive the parallel electric field $E_\parallel$. As far as the energy conservation is concerned, the temperatures of the different ions (i.e. for main and impurity ions) are assumed to be equal. This allows to consider the conservation of internal energy only for the main ion. Naturally, the balance equation for the electron internal energy is also needed.

A key point to discuss is the closure of Braginskii's equations. In particular, assumptions are necessary in order to define the quantities $\mathbf{R}_s$, W_s, $\boldsymbol{\pi}_s$ and $\mathbf{q}_s$ in terms of density, velocity and pressure. Differently from the methodology adopted in [29] where a low impurity density is assumed, these quantities are evaluated with a 21-moment approach[39]. Following this methodology, the parallel transport coefficients at each time step n are calculated with an inversion of the matrix obtained by using the plasma condition of the time step n-1 (for a detailed description the reader can refere to [39]). This is a more general approach but naturally require higher complexity and more computational time than the one derived by Braginskii. However, the 21 moment approach requires that the distribution function is close to a Maxwellian, that is the plasma is high collisional, but there are situations where the plasma temperature are too high to meet this condition. As a consequence 'kinetic corrections' are needed. The most important one is the correction on the parallel

heat flux which is corrected through specific coefficients, the *heat flux limiters* α_i and α_e, in order to avoid unphysically high parallel heat fluxes. A more detailed expression of the equations used for the closure of the problem are reported in [40]. The radial transport of particles and energy is prescribed by diffusive and convective terms. More specifically, the cross field transport processes are related to the coefficients:

- $D_{j,\rho}$ and $V_{j,\rho}^{pinch}$ for the diffusive and convective transport of particles, respectively;
- $\eta_{j,\rho}$ for the momentum transport;
- $\chi_{i,\rho}$ and $\chi_{e,\rho}$ for the main ion and electron energy perpendicular heat flux.

The values of these coefficients are externally set by the user and are adjusted to match the experimental or foreseen mid plane profiles of n and T.

Different boundary conditions are imposed depending on the region of interest. For the core boundary region we have:

- for the density the user can choose to impose either a certain value of the density or the ion flux through the innermost ring. In the latter case the user can either specify the gradient or impose that the neutral outflux toward the core equals the radial input influx into the mesh domain;
- a constant value of the parallel velocity can be set. It is generally equal to zero;
- for the temperature, the user can choose a certain gradient by imposing an input power, both for ions and electrons (the total power is generally equally split between them). Alternatively, a constant temperature can be imposed.

As far as the outermost ring is concerned, the boundary condition are externally imposed on density and temperature by defining a gradient length $n/(\partial n/\partial\rho)$ and a temperature drop in % between the outermost ring and the main wall. For the velocity, a zero radial gradient of the parallel velocity is imposed.

At the target plates the Bohm condition is applied. This means that the parallel velocity at the sheath entrance is imposed equal to the sound speed, i.e. $V_{j,\parallel}^{se} = c_{s,j}$. This condition can be relaxed by allowing supersonic flows. The boundary conditions for the electron and ion heat fluxes are given by:

$$\frac{5}{2} p_i^{se} V_{i,\parallel}^{se} + q_{i,cond}^{se} = \gamma_i p_{i,\parallel}^{se} V_{i,\parallel}^{se}, \tag{2.31a}$$

$$\frac{5}{2} p_e^{se} V_{e,\parallel}^{se} + q_{e,cond}^{se} = \gamma_e p_{e,\parallel}^{se} V_{e,\parallel}^{se}, \tag{2.31b}$$

where γ_i and γ_e are the sheath transmission factor for ions and electrons, respectively. They are generally posed to $\gamma_i \sim 2.5$ and $\gamma_e \sim 4.5$[1]. Finally, the boundary condition for the target potential drop reads as:

$$j_\parallel = j_\parallel^{th} = e\left(\sum_j n_j^{se} Z_j V_{j,\parallel}^{se} - n_e^{se}\frac{V_{e,\parallel}^{se}}{2\sqrt{\pi}} e^{-\frac{e\phi}{T_e^{se}}}\right), \tag{2.32}$$

where the parallel current is given by the thermoelectric current which arises because of the parallel temperature gradient.

Conclusively, the EDGE2D-EIRENE code is suited for an accurate description of the SOL plasma. Indeed, the presence of a reshaping of the mesh near the target plates and the neutral description performed by EIRENE allows to take into account the actual divertor geometry, while the presence of the void region between the plasma fluid mesh and the first wall can represent a limitation for a direct evaluation of effect of the first wall on the edge plasma conditions. However, several works have shown the reliability of this codes by benchmarking the results of the calculation with the experimental data, as done for example in [40]. The main disadvantages of EDGE2D-EIRENE are related on one hand to the high required computational time, especially in case of simulation of large machine as DEMO, and on the other hand to the low flexibility. This feature limits the possible magnetic configurations to simulate; more specifically, since the GRID2D is able to deal with diverted magnetic configurations with only one X-point (also the limiter cases are forbidden), it is not possible to simulate advanced divertor configurations as Snowflake or XD with the second X point near or inside the vessel. As we will see in section 3.2, GRID2D is only able to generate the mesh for cases where the second null point is far from the wall such that it can be excluded from the domain.

2.3.2 TECXY

TECXY[31] code is based on the Braginskii's equations. This numerical tool is similar to EDGE2D and solves the set of equations involving the particle and momentum balance for the different ions species, in order to take into account the presence of impurities, and the electron and main ion energy balance. All the ion temperature are assumed equal to T_i, different from the electron temperature T_e. The electron density is obtained by the quasi-neutrality condition. As in EDGE2D, the transport coefficient are obtained with a 21 moment approximation.

[1]The value of γ_e is obtained by considering that only the electrons with an energy higher than the sheat potential V_s can enter the sheath. The parallel heat flux at sheath entrance is then given by $q_{e,\parallel}^{se} = (2eT_e + |eV_s|)n_e V_{e,\parallel}^{se} + 0.7eT_e$, where the last term indicates the accelation of ions and represent an energy transfer from electrons to ions. Since $q_{e,\parallel}^{se} = \gamma_e p_{e,\parallel}^{se} V_{e,\parallel}^{se}$, we get $\gamma_e \sim 4.5$. For the ion we have that $q_{i,\parallel}^{se} = 5/2 n_i V_{i,\parallel}^{se} eT$, thus $\gamma_i \sim 2.5$.

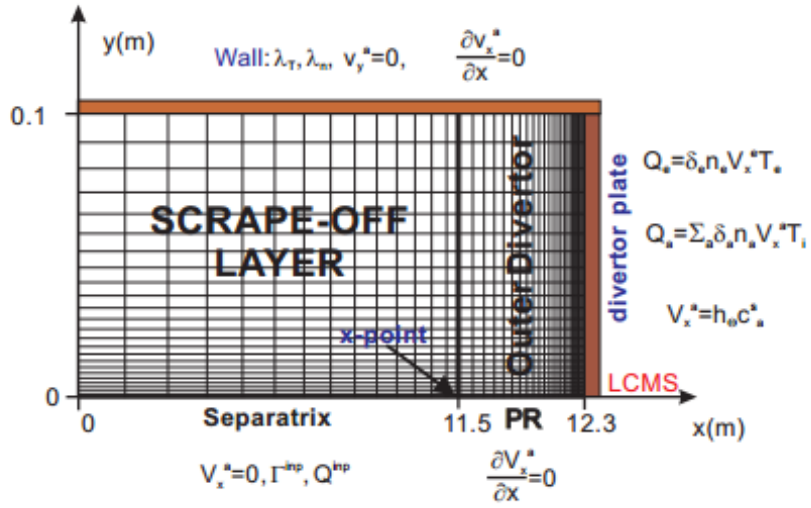

Figure 2.2: Scheme of boundary conditions used in the TECXY code. Bohm boundary conditions are imposed at the divertor plate (right). Energy and particle fluxes are set at the separatrix, while decay lengths are given for the wall and PFR region.

There are two main differences between TECXY and EDGE2D-EIRENE. The first one stems in the neutral description which is performed by means of an analytical model. This model, described in section 2.2.1 allows to speed up the simulations; however, the less accurate neutral description can strongly affect the results. As a consequence, the possible neutrals effect cannot be properly studied. It is therefore important to point out that this code is not suitable to describes such regimes where the neutral particles play an important role in defining the edge plasma condition, as in case of detachment.

The second important difference is the domain that TECXY takes into account. The real magnetic geometry is considered, namely the cells of the mesh are aligned with flux surface, whereas the target plate are imposed to be perpendicular to the separatrix. In addition, the PFR and the core region are not considered in the computational domain. These features on one hand directly reflect on a less accurate description of the SOL plasma but on the other hand allows to strongly bring down the computational time as a consequence of the simple geometry in the near target region, naturally combined with the analytical neutral description. Nonetheless, as we will see in section 3.1.4, the different physics and numerical approach used in TECXY allows a suitable description of the SOL plasma condition in attached regime. An interesting feature of this code is the high flexibility leading to the possibility of simulating advanced magnetic configuration, as done for example in [10].

A scheme of the different boundary conditions imposed in TECXY is shown in

figure 2.2. Bohm condition is imposed at the target plates, that is the ion and electron given by 2.31 and the flow velocity is equal to the projected sound speed $V_x^a = h_\Theta c_s^a$, where a is the ion specie, x the coordinate along the flux surface and $h_\Theta = B_\Theta/B$. Constant power input and particle fluxes are imposed at the separatrix; in particular, the particle flux is adjusted in order to get the desired value of the plasma density. Decay length are specified for density and temperature at the wall, while all radial gradient are zero at the PFR boundary.

Despite the simple model adopted for the neutral particles and the simplified geometry, this code is a useful tool for a first fast scan of the possible paramenter to take into account. As we will discuss in section 3.1.4, this numerical tools is suited for the description of the well attached plasma regime, where neutrals plays a minor role. By benchmarking this codes with EDGE2D-EIRENE, we see that similar trends and power loads are predicted. As a consequence, TECXY can be used for a first screening and for the assessment of the general characteristics of the possible solutions.

2.3.3 SOLEDGE2D-EIRENE

SOLEDGE2D[41],[42] is a multi fluid code for the description of the SOL plasma that is based on mass, momentum and energy balances derived from the Braginskii's equations. As previously, the quasi-neutrality condition is assumed, that means only mass and momentum conservation laws for main and impurities ions are considered. The electron density are then given by 2.30 and from ambipolarity we get $u_e = u_i = u$. Contrarily to EDGE2D and TECXY, in SOLEDGE2D the energy balance is solved for each ion specie and for electrons. These equations are written in terms of total energy, that is by considering the thermal and parallel kinetic energies. The details of the set of partial differential equations solved by this numerical tool is given in [41] or [42]. In addition, in the parallel electron balance equation the inertia and viscosity terms are neglected and the parallel electric field is given by:

$$enE_\parallel = -\nabla_\parallel(nT_e) - R_{ei}, \tag{2.33}$$

where R_{ei} is the electron-ion friction force. The cross field transport is treated via diffusive models, which for particle transport also take into account a convective term through a cross field pinch velocity $\vec{v}_{pinch}$. The diffusion coefficient $D, \mu, \chi_{i/e}$ are set externally by the user and chosen to fit experimental data or expected profiles. As EDGE2D, this fluid code is coupled with EIRENE for the neutral description. This allows to perform an accurate evaluation of the neutral effect on plasma conditions. Furthermore, for a fast analysis, a coupling with a fluid model is also possible.

As previously discussed, the combination of a field aligned mesh with the different shape of the vessel can be obtained by reshaping the grid cells in the near target region. As a results, proper boundary conditions can be imposed in this area, e.g.

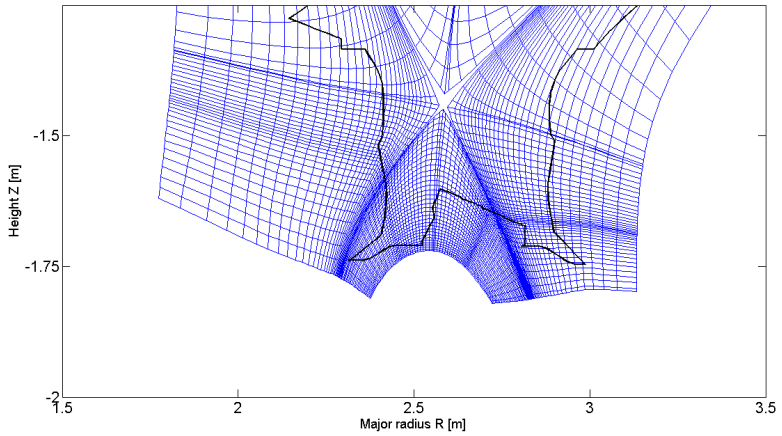

Figure 2.3: Zoom in the divertor region of a mesh obtained with the SOLEDGE2D mesh generator. The cells are aligned with the flux surfaces. The penetration of the grid into the vessel wall (black line) and the subdivision in the three different regions (i.e. SOL, core and PFR) are clearly visible.

Bohm condition. However, this mechanism can increase on one hand the complexity of the code and on the other hand the computational time. SOLEDGE2D is based on a different numerical approach to implement the boundary condition at the vessel wall. A '*penalization technique*' is used. In this novel approach a mask function is used to define the wall domain. More precisely, the grid includes plasma domain and extends into the vessel wall, as can be seen in figure 2.3. On the boundary of the plasma domain the grid is not aligned with the vessel wall. The two domain are defined via the penalization parameter χ which is zero in the plasma and 1 otherwise. This parameter is used to insert extra terms in the balances equations into the wall domain without generating extra source terms in the plasma. As a consequence, boundary conditions at the plasma-wall interfaces are recovered. This numerical scheme has been tested in different work both for limiter[43] and divertor[44] configurations. As far as the core boundary conditions are concerned, a power input and particle flux can be imposed at the innermost flux surface. Alternatively, the user can specify a certain value of density and temperature.

Given the different characteristics of SOLEDGE2D code, combined with the possibility to adopt EIRENE for the neutral description, it is particularly suited for the simulation of different edge plasma scenarios. The penalization technique used to implement the wall boundary conditions have two important consequences:

1. it allows to directly assess the effect of the first wall on the SOL plasma. This can be done since the grid extend up to the vessel and any assumption is imposed on the profile of the plasma parameter in the far SOL region;

2. the increase of the flexibility of the code since any shape of the vessel can be defined. This is possible since only a redefinition of the mask function matrix is necessary. As a results, the code is also able to treat advanced magnetic configurations with more than one X-point.

These features, especially the latter point, are very interesting for the purpose of the PhD research activity. However, a validation phase is necessary and a benchmark of the results with experimental data is required. This is the focus of the chapter 4, where the results obtained with SOLEDGE2D-EIRENE code on a JET experiment are compared with the corresponding experimental data.

2.3.4 Other codes: SOLPS and EMC3-EIRENE

Finally, it is worth to mention other two edge codes, largely diffused in the fusion community. The first one is SOLPS[33][45], also known as B2-EIRENE. This code is very similar to EDGE2D-EIRENE. The fluid description is based on the Braginskii's equations and toroidal symmetry is assumed. The neutral particle dynamics is described by means of EIRENE, but also a fluid model can be adopted. The boundary conditions imposed at the target plates are given by the Bohm conditions. The parallel transport is given by the expression derived by Braginskii[29]. This numerical tool is becoming the most used code in the framework of the SOL plasma modeling and is the one used for ITER simluations; in particular, the so called SOLPS-ITER code has been developed and optimized to study the ITER divertor conditions[46].

The second one is EMC3-EIRENE in which the 3D plasma fluid code EMC3[47] is coupled with the neutral tracker EIRENE. EMC3 solves the time-independent Braginskii's equations for mass, momentum, electron and ion energy in 3D by using a Monte Carlo method. This code is particularly suited, and even necessary, to treat all the cases characterized by an intrinsic 3D nature of the configuration to study, e.g. in case of induced Resonant Magnetic Perturbation.

Chapter 3

EDGE2D-EIRENE modelling

The EDGE2D-EIRENE code presented in the previous chapter is used to simulate the SOL plasma in different machines and configurations. The analysis starts by considering a possible DEMO scenario (see table 3.1). This work is performed in the framework of the EUROfusion Work Package WPDTT1. A set of input parameters that define the so called 'baseline solution' is chosen since they are not expected to change drastically in terms of power and major radius. In the analysis a scan in density and in diffusion coefficients is performed in order to identify the characteristic conditions and regimes of the SOL.

Most importantly, a benchmark of TECXY and EDGE2D-EIRENE is discussed. The comparison of the numerical results shows the role of the different description of the neutral particles that has a strong effect on the density and temperature on the outer target. Nonetheless, the two codes predict similar SOL plasma conditions and similar trends of the global quantities.

In the second part of this chapter the analysis is focused on the DTT machine. As previously noted, one of the main mission of this proposed satellite tokamak is the study of the power exhaust issue in DEMO relevant conditions. This device is particularly suited to study alternative divertor solutions. We perform a preliminary analysis of a QSF configuration which is compared to the reference one.

A density scan is performed in order to study the different behaviour of the two configurations. First of all, the aim of this study is to identify the different SOL plasma conditions and the effect of the topology change on the attainment of the detachment. Subsequently, the analysis focuses on the power loads onto the outer target. While in the SN case the code predicts heat flux densities higher than the tolerable value in the over all density scan, in QSF manageable values of the power loads are obtained. The main driver for the different bahaviour is recognized in the different topological properties.

Furthermore, since stable detached regimes are mandatory for DEMO, we investigate the effect of the magnetic topology on the neutral particles behaviour by analysing the neutral density and pressure and the radiation by deuterium atoms.

Table 3.1: Main parameters of the DEMO baseline scenario used for the EDGE2D-EIRENE simulations[49].

Parameter	Unit	Value
Major radius (R)	m	9
Aspect ratio (A)	-	3
Toroidal field (B_{tor})	T	5.24
Plasma current (I_p)	MA	20.3
Pulse length	h	1.5
Average density ($\langle n \rangle$)	$10^{19} m^{-3}$	7.7
Average temperature ($\langle T_e \rangle$)	keV	12.8
Net electric power (P_{net})	MW	500
Auxiliary power (P_{aux})	MW	50
Fusion power (P_{fus})	MW	1794
Power crossing separatrix (P_{sep})	MW	150

We show that in case of QSF a stabilizing effect is observed and neutral particles are better confined near the target than in SN.

Finally, an initial analysis on a liquid lithium divertor is discussed. However, the main aim of this part of the study is not yet achieved since of numerical problems leading to code crashes or unacceptable results. The results obtained by considering regimes dominated by the Li sputtering shows that the power peaks are barely affected by the change of the target materials since of the low level of radiation by lithium. However, a complete and accurate analysis should also consider the Li evaporation and motivate a future work.

3.1 DEMO simulations

3.1.1 DEMO baseline scenario

The conceptual design of DEMO is not yet fully defined and different possibilities are currently under investigation in the EUROfusion community by considering the safety, environmental and socioeconomic aspects[48]. However, by considering the main missions and the most important constraints, one can define a set of relevant parameters which can represent the milestones for a reference solution. This baseline solution can be viewed as a 'conservative baseline design' and it is based on the expected performance of ITER, assuming possible moderate improvements of the technology and of the physics performances. Currently, it is based on a long pulse inductively supported plasma in a conventional H-mode plasma scenario with SN

divertor configuration and W divertor plates. The leading parameters are given in table 3.1. A modest confinement improvement factor $H = 1.1$ and a relatively low β_N are foreseen. The production of net electrical power is fixed to $P_{net} = 500MW$, while the major radius $R = 9m$ is fixed by the ignition criterion and the aspect ratio A by the need to sustain the plasma having fixed P_{net} and R.

Particular emphasis should be given to the value of the power entering the SOL, P_{sep}. If we consider the main parameters in table 3.1 and following the scaling proposed in [16], we have a lower threshold to work in H-mode $P_{sep} > P_{L-H}$ given by:

$$P_{LH} = 2.15e^{\pm 0.107} n_{e20}^{0.782\pm0.037} B_{tor}^{0.772\pm0.031} a^{0.795\pm0.08} R^{0.999\pm0.101} \approx 136MW, \qquad (3.1)$$

where a is the minor radius $a = R/A = 3m$. Therefore, the power crossing the separatrix is fixed to $P_{sep} = 150MW$.

Another important parameter to consider is the power e-folding length evaluated at the equatorial plane. As previously noted, we can evaluate this value by following the scaling law suggested by Eich[13]. Considering the reference parameters of the baseline scenario, we get:

$$\lambda_q(mm) = (0.73 \pm 0.38) B_{tor}^{-0.78\pm0.25} q_{cyl}^{1.2\pm0.27} P_{sep}^{0.1\pm0.11} R^{0.02\pm0.2} \simeq 1mm, \qquad (3.2)$$

where q_{cyl} is the cylindrical safety factor. However, we refers to λ_{int} since it also takes into account the diffusion in the PFR and given by:

$$\lambda_{int} = 1.3\lambda_q + 1.36 \pm 0.4mm \simeq 3mm. \qquad (3.3)$$

It is worth noting that this parameter is essential since in the generation of the EDGE2D-EIRENE grid we use λ_{int} as reference parameter for the resolution.

Finally, we should point out that in DEMO stronger constraints than in ITER are imposed to the target materials in terms of power load and sputtering. On one hand, since of the high neutron and particle fluence, the tolerable heat fluxes are limited to value smaller than $10MW/m^2$. On the other hand, the erosion limit must be compatible with 2 years lifetime of the component, that is fully detached conditions are mandatory and the maximum divertor plasma temperature is limited to $5eV$.

3.1.2 EDGE2D-EIRENE inputs

As a first approximation, a pure deuterium plasma is considered since the first aim of this work is a preliminary parameters scan in order to identify the behaviour and the different conditions of the SOL plasma in terms of temperature, density and collisionality. As a consequence, the choice to leave the external impurities out of the simulations is motivated by the possibility to drastically reduce the computational

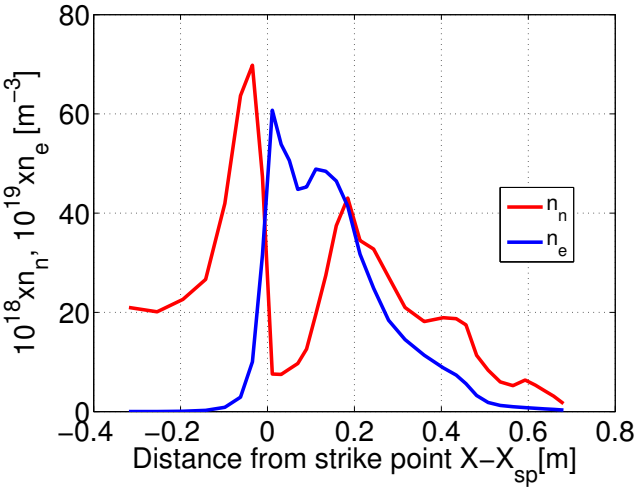

Figure 3.1: Neutral (red line) and electron (blue line) density on the outer target. The mesh is generated by considering the actual shape of the vessel and gives unreasonable results.

time. In addition, this study also represents the reference point for a comparison with preliminary parameter scans of alternative divertor configurations in order to analyse the different SOL plasma behaviour.

The first input to consider is the grid generated for the calculations. The magnetic equilibrium is a SN divertor configuration with the strike points located on the vertical targets both on inner and outer divertor regions. However, numerical instabilities arise in the calculation leading to unreasonable results on the target plates, especially for low separatrix density at the equatorial plane $n_{e,LCMS}$. Figure 3.1 shows the profile on the outer target of the electron and neutral density obtained by considering the actual shape of the divertor. It is evident that the results obtained in the calculation are unacceptable from a physic point of view because, on one hand, the neutral density shows the presence of two peaks, one in the private region and the other one in the SOL. This clearly disagrees with the expected diffusive behaviuor of neutral particle, which are not confined by the magnetic field. On the other hand, the electron density shows a hole near the strike point location. In addition, the numerical noise in the temporal evolution of the target quantities is too high with an oscillation of the same order of magnitude of the quantity itself.

In order to solve these issues leaving the shape unchanged, a sensitivity analysis is performed by changing the EIRENE parameters, that is the frequency of EIRENE calls in the simulation and the number of histories. A slight reduction of the numerical noise is observed, whilst the target profiles retain the same behaviour. As a second step, a change in the grid is carried out by changing the grid resolution in the target region. An improvement of the target profiles is obtained, but the results

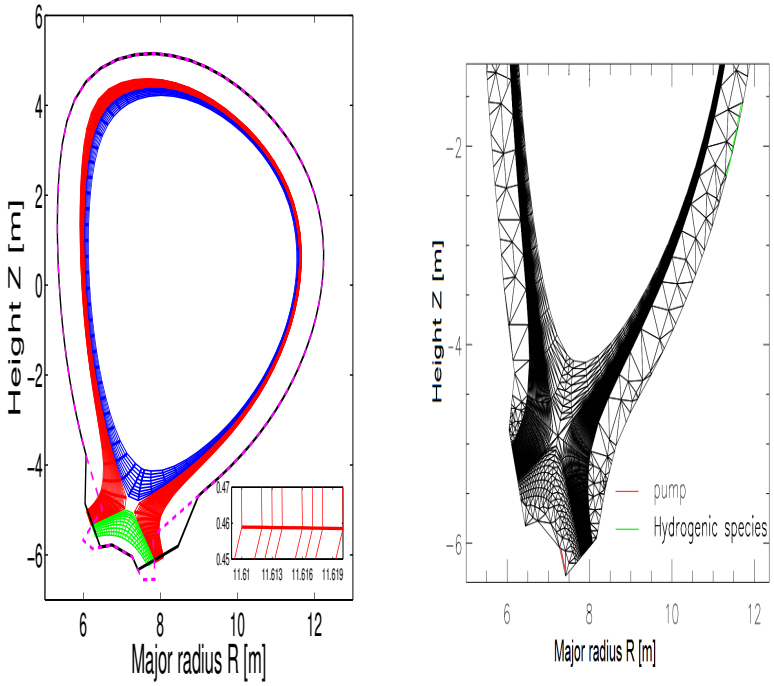

(a) (b)

Figure 3.2: (a) Mesh generated for the EDGE2D calculations with GRID2D. The PFR, core and SOL regions are shown in green, blue and red, respectively. The vessel with perpendicular targets (black line) and the actual shape (magenta line) are also depicted. In the bottom right corner a zoom of the OMP is shown. The resolution of the grid is chosen such that at least 4 point are defined within a λ_q. (b) The EIRENE mesh generated by EDGE2D-EIRENE code. The extension up to the vessel and the definition of the triangles on the fluid mesh are visible. Also shown are the location of the pump and of the deuterium puff.

are still unacceptable. Therefore, the conclusion is that the numerical issues are probably related to the distortion of the polygons near the target plate performed by the code in order to implement the boundary conditions.

Perpendicular target are then imposed, by leaving the strike point location unchanged. This change in the vessel geometry can affect the results since a closure of the vessel can help to access detachment regimes[50]. However, as a first approximation we can evaluate only the geometrical effect by considering the target inclination in the poloidal plane. This hypothesis is as good as far we are from detachment. Hereafter, we confirm this hypothesis since well attached plasma conditions are simulated.

The mesh generated with GRID2D for the fluid computation is shown in figure

3.2. The three different sub-domains are shown in red (SOL), green (PFR) and blue (core). The resolution of the mesh is chosen by considering $\lambda_q \simeq 3mm$. In the bottom right corner a zoom of the first SOL rings is depicted. We can see that at least three rings are located within λ_q, that means a grid resolution of $\sim 1mm$. In addition, the perpendicular targets and the actual vessel shape are shown in black and magenta, respectively. The poloidal tilt of the vertical target is $\theta = 23°$ and we can consider this value to evaluate the beneficial effect deriving from the target geometry. The mesh generated for the EIRENE calculation is shown in figure 3.2b. The extension of the mesh up to the wall and the definition of the triangles by superposition on the EDGE2D fluid mesh are clearly visible. The puff and the pump location are given respectively in red and green.

The external deuterium puff is feedback controlled by the code. A value of the separatrix electron density $n_{e,LCMS}$ is imposed and the puff is automatically given by taking into account the recycling of deuterium. The recycling coefficient is set to $R_c = 1$ both on divertor and first wall since a fully W wall is considered in the simulations. The pump is defined by imposing an albedo $\alpha = 0.94$, that is the 6% of the particles reaching the pumping surface are taken out of the domain.

The default setting for the EIRENE model is used, namely we consider the atomic and molecular processes listed in table 2.1. The frequency for the EIRENE calls and the number of histories are chosen empirically by considering the numerical noise on the temporal quantities and the required computational time: a maximum frequency of 10 time steps and a total number of 30000 histories are chosen.

Finally, the boundary conditions are defined by the input power P_{sep}, equally split between ions and electron, and by the standard value of the radial decay lengths on the outermost rings. The Bohm criterion is relaxed at the target plates, allowing supersonic flows. As a first approximation, drifts are neglected in the simulations (also for the DTT case in the next section) since we are performing a preliminary scoping study and we are mainly interested in the outer target quantities.

3.1.3 Results

The analysis of the SOL is performed by considering two different parameters scans. The first one involve a change of the upstream density, by fixing all the other parameters. This analysis is performed in order to identify the plasma regimes obtained by considering the range of separatrix densities compatible with the average density reported in table 3.1. The results are presented in terms of outer target profiles and trends of the global quantities. The assessment of the accessed regime is obtained by studying the collisionality and further confirmed by evaluating the trends of the maximum electron density and ion flux on the target plates with respect to a change of $n_{e,LCMS}$.

The second scan is performed in terms of diffusion coefficient in order to approach

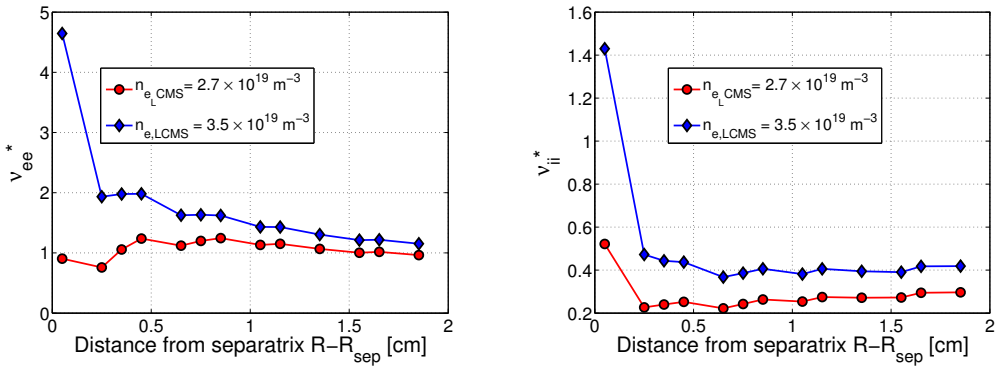

(a) (b)

Figure 3.3: (a) Electron and (b) ion upstream collisionality profiles obtained by using eqs. 3.4 as a function of the distance from the separatrix.

the power e-folding length foreseen by the Eich's scaling (eq. 3.3). In this case the upstream density is fixed and the obtained results in terms of power loads and global trends are scanned as a function of λ_q.

Density scan

The separatrix density is constrained to $n_{e,LCMS} = 2.7,\ 3,\ 3.2,\ 3.4$, and $3.5 \times 10^{19}\ m^{-3}$ which is compatible with a predicted average density of $\langle n \rangle = 7.7 \times 10^{19}\ m^{-3}$. Even though we are simulating an H-mode plasma, we set constant diffusion coefficients that can approach the predicted power e-folding length. This value comes from previous TECXY simulations and a benchmark of these two codes will be presented hereafter.

Outer midplane profiles The first step in the analysis is the assessment of the plasma regime in the density scan. Figure 3.3 shows the profiles of the electron (3.3a) and ion (3.3b) upstream collisionality as a function of the distance from the separatrix given by[3]:

$$\nu_{ii}^* = \frac{L}{\lambda_{ii}} \approx 10^{-16} \frac{n_{i,u} L}{T_{i,u}^2}, \tag{3.4a}$$

$$\nu_{ee}^* = \frac{L}{\lambda_{ee}} \approx 10^{-16} \frac{n_{e,u} L}{T_{e,u}^2}, \tag{3.4b}$$

where L is the connection length obtained as the distance between the equatorial plane and the target in the parallel direction and the subscript u refers to the upstream quantities evaluated at the equatorial plane. The profiles for both the

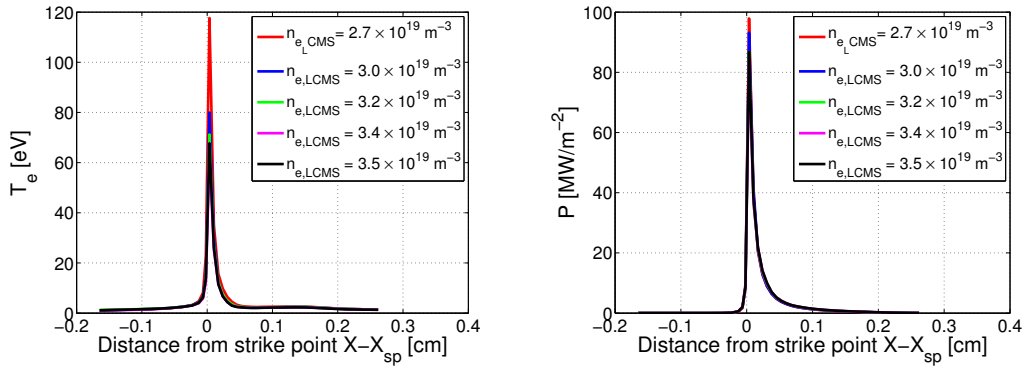

(a) (b)

Figure 3.4: (a) Electron temperature and (b) power flux density profiles on the outer target obtained with the EDGE2D-EIRENE simulations of DEMO scenario corresponding to the reference parameters of table 3.1. The profiles correspond to the different values of the upstream density imposed in the simulations.

highest and lowest density is depicted in order to assess the SOL plasma and divertor conditions in the over all range of simulated densities. First of all, it is worth noting that $\nu^*_{ee} > \nu^*_{ii}$ that means $T_{e,u} < T_{i,u}$. By considering that the input power is equally split between ions and electrons, this behaviour is related to the higher volumetric losses for electron than for ions that occurs in the SOL.

By comparing the upstream collisionality values with the the conditions in section 1.3.3 we see that the SOL plasma is in sheath limited regime since $\nu^* \ll 30$. As a consequence, since of the low influence of the neutral dynamics in this plasma condition, we confirm the possibility to adopt a perpendicular target instead of a vertical one. Therefore, we can evaluate the results in terms of power load by simply considering the target tilting.

Considering that in 'well attached conditions' the parallel power flux is $P \propto n_e T_e^{3/2}$, we can evaluate the power e-folding length at the equatorial plane. By considering the temperature and density profiles for the lowest density, we get $\lambda_q = 3.64mm$, slightly higher than the one obtained in eq. 3.3.

Outer target profiles Figure 3.4 shows the temperature (3.4a) and power flux density profiles on the outer target (3.4b) for the different values of the densities taken into account. As expected, the code predicts very high electron temperature on the outer target. The peak value decreases by 42% ranging from $T_{e,peak} = 117eV$ to $67eV$. Considering that the upstream temperature are around $T_e \approx 250eV$, which is a reasonable value for DEMO, the temperature gradients that set up along the SOL are quite low, confirming the low recycling plasma condition. In addition, it is important to point out that these temperatures represent a critical issue for the

Table 3.2: Peak values of the density and ion flux on the outer target obtained in the numerical simulations of the density scan of the DEMO reference scenario with the EDGE2D-EIRENE. The trends for the different variables, in terms of the exponents of the upstream density, and the one predicted by the 2PM[3] are also given.

$n_{e,LCMS}$ $[10^{19}m^{-3}]$	$n_{e,ot,peak}$ $[10^{21}m^{-3}]$	$\Gamma_{ot,peak}$ $[10^{24}m^{-2}s^{-1}]$
2.7	0.96	1.42
3.0	1.37	1.75
3.2	1.3	1.78
3.4	1.52	1.92
3.5	1.59	1.95
E2D	1.68	1.25
2PM	3	2

sputtering problem even in presence of a pure deuterium plasma. In particular, the obtained target electron temperatures are higher than $T_e = 50eV$ which represents a threshold for the sputtering of W by deuterium ions.

The power profiles refers to the mesh with perpendicular target. Throughout the density scan the heat flux profiles remain approximately constant. This behaviour is related to the low change in the volumetric energy losses with respect to the increase in density. Indeed, the power peak decreases only by the 10% passing from $P_{ot,peak} = 97MW/m^2$ to $86MW/m^2$.

As a first approximation, the geometrical effect of the target tilting $\theta = 23°$ is given by:

$$P_{ot,peak,real} = P_{ot,peak} * \sin(\theta) = 33.9\frac{MW}{m^2}, \tag{3.5}$$

where we consider the highest density case since it is the least critical one. However, even though the geometry is taken into account the power loads are not sustainable for any target material. Clearly, the obtained results are totally unacceptable from an operational point of view and should be considered as a reference for a possible comparison with scoping studies of other alternative solutions.

Finally, it is interesting to compare the trends of the target quantities as a function of the upstream density obtained with the numerical simulations with the one predicted by the two point model. Table 3.2 gives the peak values of the density and ion flux on the outer target. The trends predicted by the EDGE2D-EIRENE result in a weaker dependence on the upstream density than in case of the two point model. This behaviour further confirms that the SOL plasma is in low recycling regime, where the $\Gamma_t \propto n_t \propto n_u$.

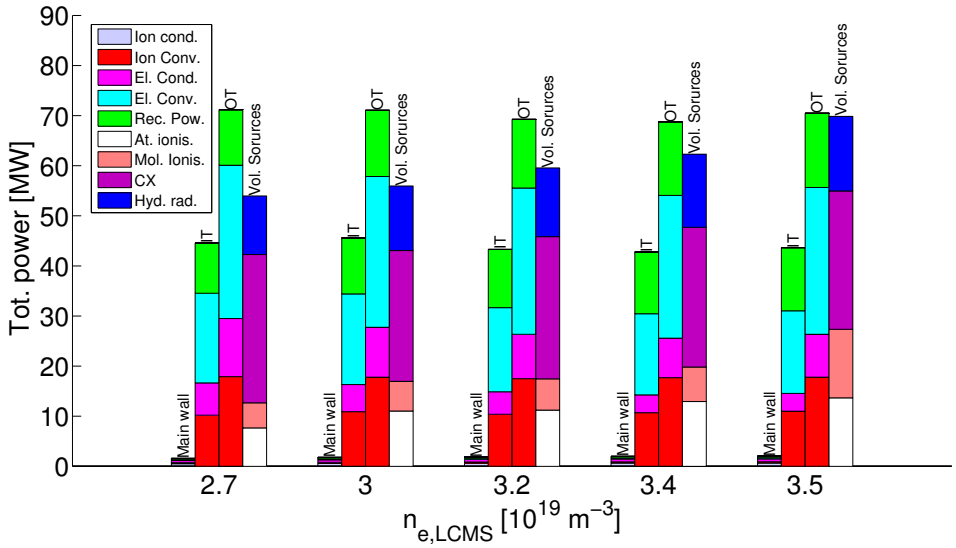

Figure 3.5: Histogram representing the total power balance of the EDGE2D-EIRENE simulations. The input flux is given by $P_{sep} = 150MW$. The different fluxes to main wall, outer divertor and inner divertor are decomposed in the different terms related to electron and ion conduction and convection. The different terms of the volumetric sources are also shown.

Global quantities In order to assess the correctness of the obtained results, the global energy balances are performed. Bearing in mind the EDGE2D conservation equations (cf section 2.3.1) and considering steady state conditions, we have that in the global balance the net flux must be equal to the internal volumetric sources. The sources are given by the plasma neutral interaction and includes ionisation and dissociation of atoms and molecules, hydrogen radiation and charge exchange.

Figure 3.5 shows the different terms of both outflux and volumetric sources for the 5 upstream density values taken into account. Furthermore, the recombination power reaching the vessel wall and the divertor plates is also shown. Performing the global balance and considering that the input power is $P_{sep} = 150MW$, we get a relative error $e_{rel,pow} = ((P_{sep} - P_{tot,out}) + Sources)/P_{sep} < 1\%$ in the over all density scan. This results is further confirmed by considering the particle balance which is dominated by the ionization source. Performing a global balance and normalizing the error to the ionization source the conservation of particle is fulfilled with an $e_{rel,part} = (\Gamma_{net} + Sources)/S_{ions} < 1\%$.

Observing the different terms in the global balance, we can see that the total power onto the divertor plates (both inner and outer) remains approximately constant throughout the density scan. Most of the power is carried by electron and ion convection through the sheath that is characteristic of the sheath limited regime. In

addition, a non negligible part of the power deposited on the divertor plates is given by the recombination power, which ranges from 14% to 20% in the density scan.

As far as the volumetric sources are concerned, they remain approximately constant as well as the contribution of the single terms. A large part of the sources is given by the ionisation and charge exchange processes. It is worth noting that the CX process is not able to dissipate momentum and energy such that the SOL plasma can access different regimes. Indeed, more than 1/3 of the CX processes in terms of volumetric power sources occur inside the confined region, while the remaining part is split between main SOL and inner divertor chamber ($< 30\%$) and outer divertor chamber. However, a small change is observed by varying the upstream density. The hydrogen radiation is small for all the upstream density values and increases by 4 MW for $n_{e,LCMS} = 3.5 \times 10^{19} m^{-3}$ that corresponds to an increase by $\sim 27\%$.

As a final remark, we should focus on the different power reaching the inner and outer divertor plates. Figure 3.5 shows a big difference in the two integral values. In particular, the ratio of the two output power is $P_{out}/P_{in} = 1.6$. As expected, the outer divertor targets is the most critical one and this behaviour motivates the choice to concentrate our analysis on outer target quantities only.

Diffusion coefficients scan

The second performed scan involves a change of the diffusion coefficients by fixing the upstream density to $n_{e,LCMS} = 3 \times 10^{19} m^{-3}$, which corresponds to the averaged density in table 3.1, and keeping all the other inputs unchanged. The aim of this scan is to approach the $\lambda_q \approx 3mm$ obtained with the Eich's scaling. Moreover, we can study the effect of a change in the SOL behaviour by varying the set of diffusion coefficients, that is we are simulating a change of the cross field transport properties in the SOL plasma.

Figure 3.6 shows the three parallel power flux profiles obtained considering that $P \propto n_e T_e^{3/2}$. The profiles refers to the equatorial plane and are normalized to the corresponding separatrix values. The obtained power e-folding lengths are given by $\lambda_{q,1} = 3.11mm$, $\lambda_{q,2} = 3.64mm$ and $\lambda_{q,3} = 5.38mm$ for $D_{\perp,1} = 0.22m^2/s$, $\chi_{i,e,1} = 0.08m^2/s$ (red), $D_{\perp,2} = 0.32m^2/s$, $\chi_{i,e,2} = 0.12m^2/s$ (blue) and $D_{\perp,3} = 0.42m^2/s$, $\chi_{i,e,3} = 0.215m^2/s$ (green), respectively. We wish to point put that in order to study the effect of a change of the diffusion coefficients we use the power e-folding length as scanning parameter since the latter represents a more practical physical quantity than the couple $D_\perp, \chi$.

The results obtained in the diffusion coefficients scan are given in figure 3.7 in terms of power density profiles (3.7a) onto the outer target and global quantities (3.7b). As far the power profiles are concerned, a decrease in the power peak is observed by increasing in λ_q. In addition, a spread of the power deposition occurs, but the integral power remains approximately constant. This bahaviuor is simply related to geometrical reasons since higher λ_q, larger the wetted area A_{wet} as defined

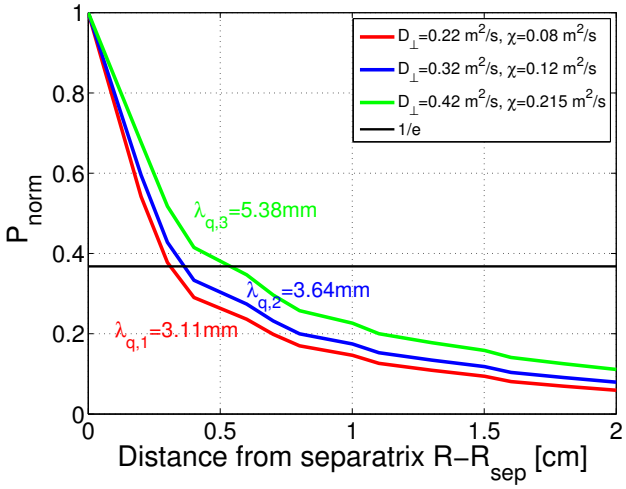

Figure 3.6: Parallel flux profiles $P \propto n_e T_e^{3/2}$ normalized to the separatrix value for the three different set of diffusion coefficients $D_{\perp,1} = 0.22m^2/s$, $\chi_{i,e,1} = 0.08m^2/s$ (red), $D_{\perp,2} = 0.32m^2/s$, $\chi_{i,e,2} = 0.12m^2/s$ (blue) and $D_{\perp,3} = 0.42m^2/s$, $\chi_{i,e,3} = 0.215m^2/s$ (green). Also shown are the corresponding λ_q and the $1/e$ line (black). The input power and the separatrix density are $P_{sep} = 150MW$ and $n_{e,LCMS} = 3 \times 10^{19}m^{-3}$.

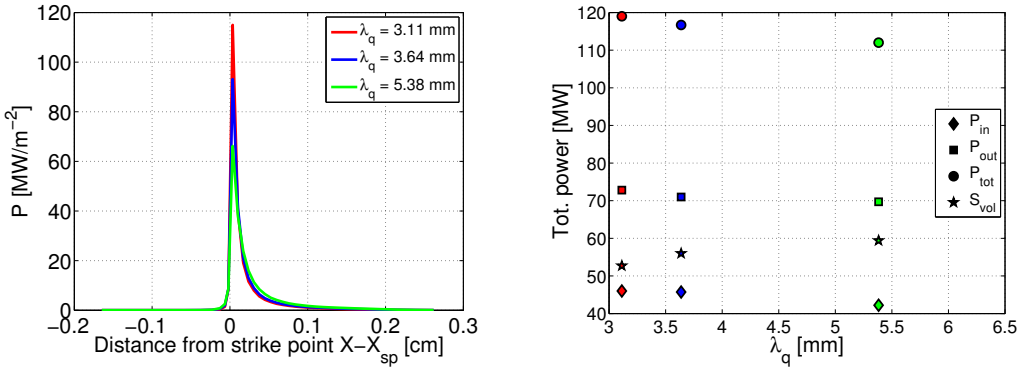

(a) (b)

Figure 3.7: (a) Power loads onto the outer target as a function of the distance from the strike point. (b) Total power reaching the inner (diamonds), the outer (square) and both the divertor (circle) plates. Also shown is the value of the volumetric sources (star). The results for the three different set of diffusion coefficient $D_{\perp,1} = 0.22m^2/s$, $\chi_{i,e,1} = 0.08m^2/s$ (red), $D_{\perp,2} = 0.32m^2/s$, $\chi_{i,e,2} = 0.12m^2/s$ (blue) and $D_{\perp,3} = 0.42m^2/s$, $\chi_{i,e,3} = 0.215m^2/s$ (green) are shown.

in 1.8. The validation of this hypothesis is confirmed by considering the dependence

of the power peaks on λ_q. By fitting the three peak values with a power function we get $P_{ot,peak} \propto \lambda_q^{-1}$. This behaviour also shows the minor role played by the volumetric losses on plasma conditions.

In addition, it is worth noting that the peak value corresponding to $\lambda_{q,1} = 3.11mm$ is more realistic than the one obtained in the previous section. By considering the target tilting we eventually have $P_{ot,peak,real} = P_{ot,peak} sin(23°) = 45MW/m^2$.

Contrarily, the global quantities (figure 3.7b) remain approximately constant for the different set of diffusion coefficients. A slightly decrease in the total power density on the divertor plates (both on inner and on outer target) is observed ($\approx 6\%$). This reduction is balanced by an increase in the volumetric sources mainly due to an increase in the atom ionisation, which amounts to $3.74MW$ (increase by $\approx 42\%$), while the other contributions are smaller and comparable each other. This bahaviour is further confirmed by the weak dependence on λ_q given by $P_{tot} \propto \lambda_q^{-0.1}$.

3.1.4 Benchmark of EDGE2D-EIRENE and TECXY

As discussed in 2.3.1, EDGE2D-EIRENE is not able to deal with advanced magnetic configurations because of the presence of the second null point. Therefore, the use of alternative numerical tools is necessary. TECXY is one of the available code that, differently form EDGE2D-EIRENE, make use of an analytical function to describe the neutral dynamic. However, due to the flexibility of the mesh generator, it is able to deal with the presence of more than one X-point.

In this section a benchmark of TECXY and EDGE2D-EIRENE is presented by comparing the numerical results obtained in the two calculations in terms of local profiles and global quantities. The comparison involves both the parameter scans performed with EDGE2D-EIRENE. The reasons for the differences are then investigated by considering the different numerical and physical models adopted in the edge plasma description.

TECXY inputs

Figure 3.8 shows the mesh used for the TECXY simulations. As in EDGE2D, the real magnetic geometry is taken into account, while the actual shape of the divertor is neglected by imposing perpendicular plates. It is worth noting that the lack of an accurate of the Monte-Carlo statistical approach allows to neglect the real divertor geometry and motivates the choice of perpendicular targets. As a consequence of the absence of the cell reshaping near the target, the computational time is drastically reduced and the effect of the poloidal tilting is recovered by using geometrical considerations. The computational domain, shown in red, is restricted to the SOL only whereas, differently from EDGE2D, the PFR and the core are not taken into account. This means that proper boundary conditions are set to the code, as explained in section 2.3.2. It is worth noting that the grid resolution is compatible

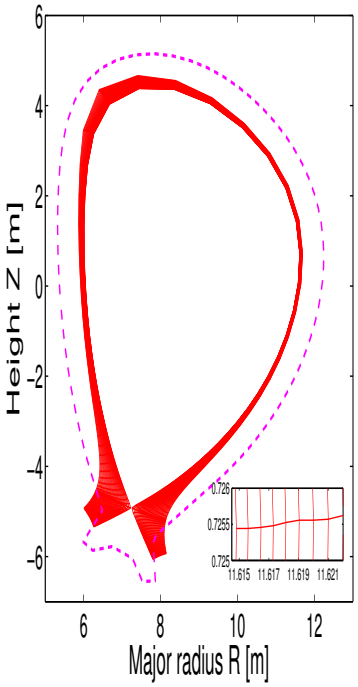

Figure 3.8: TECXY mesh used to simulate the SOL plasma of the DEMO reference scenario. The computational domain considers the SOL (red), while the core and PFR are not taken into account. The target plates are imposed perpendicular to the separatrix and the actual shape of the vessel is depicted with the magenta dotted line. A zoom of the OMP is shown in the right bottom corner.

with a $\lambda_q \approx 3mm$ since at least 5 rings are defined within a λ_q at the OMP. This feature is highlighted by means of the OMP grid zoom in the right bottom corner.

In order to compare the numerical results of the two codes, we perform the same parameter scan in density and diffusion coefficients. In the density scan the input are set similar to EDGE2D-EIRENE and derived from the values in table 3.1. However, the separatrix density at the equatorial plane is not feedback controlled but it is obtained by regulating the particle influx into the SOL. The diffusion coefficients are set to $D_{\perp,2} = 0.32m^2/s$, $\chi_{i,e,2} = 0.12m^2/s$. Finally, the particle sink is assigned by means of a recycling coefficient $R_c = 0.9985$ physically related to the pumped flux.

Comparison of the density scan results

Outer midplane profiles First of all, we compare the results in terms of profiles at the equatorial plane. Figure 3.9 shows the radial profiles of the electron density and temperature as a function of the distance from the separatrix obtained with

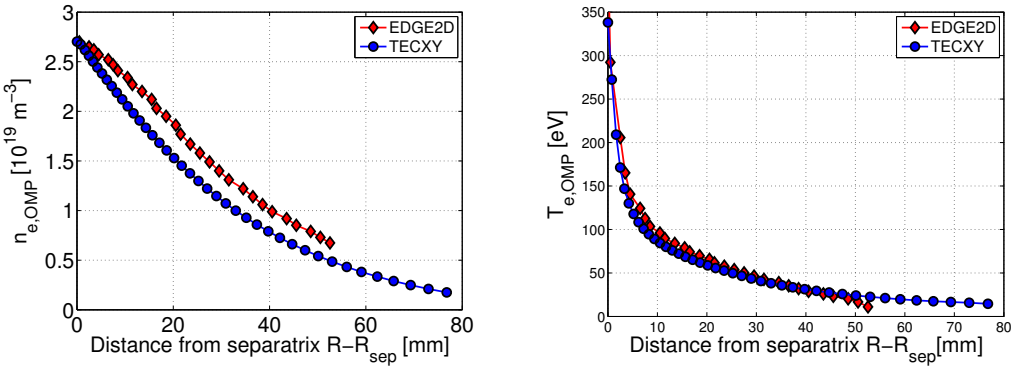

(a) (b)

Figure 3.9: Electron (a) density and (a) temperature profiles at the outer midplane as a function of the distance from the separatrix. The results obtained with EDGE2D-EIRENE (red diamonds) and TECXY (blue circles) refer to the DEMO reference scenario (table 3.1) with an upstream density $n_{e,LCMS} = 2.7{\times}10^{19}m^{-3}$. The diffusion coefficients are equal to $D_\perp = 0.32m^2/s$, $\chi_{i,e} = 0.12m^2/s$ for both calculations.

EDGE2D-EIRENE (red diamonds) and TECXY (blue circles). We refer to a separatrix density $n_{e,LCMS} = 2.7 \times 10^{19}m^{-3}$ since the profiles are similar in the overall density scan. Comparing the two curves, both in terms of electron density and temperature, we have a good match between the two codes since the most important differences stem in the neutral description and in the definition of the domain.

Furthermore, since the upstream profiles are similar and considering that the magnetic equilibrium is the same, we get similar results in terms of upstream collisionality. In other words, both the codes predict 'well attached' plasma conditions, i.e. a plasma is in sheath limited regime.

Outer target profiles We can now focus on the results in terms of target profiles. As previously, we refer to $n_{e,LCMS} = 2.7 \times 10^{19}m^{-3}$ since the results are similar for all the considered upstream densities. Figure 3.10 shows the electron density (3.10a) and temperature (3.10b) on the outer target obtained by means of EDGE2D-EIRENE (red diamonds) and TECXY (blue circles). The comparison of the results shows large mismatches, even though the OMP profiles agree quite well and the two codes foresee the same plasma condition in the divertor region. In particular, the electron density profiles differ by one order of magnitude; moreover, a different profiles shape is obtained being more peaked in EDGE2D-EIRENE than in TECXY.

Considering that the pressure should preserve along the flux tube as a consequence of the sheath limited regime, discrepancies are also observed in temperature profiles. Indeed, the temperature peak in TECXY is higher than in EDGED-EIRENE, respectively given by $T_{peak,TECXY} = 147eV$ and $T_{peak,E2D} = 117eV$; these

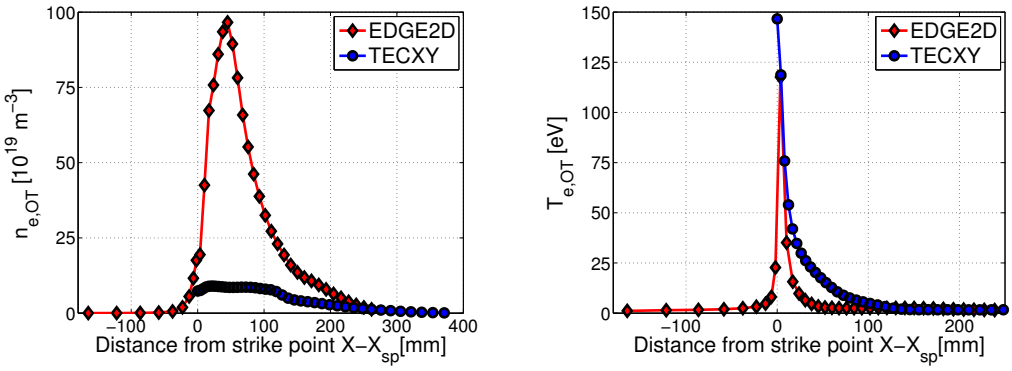

(a) (b)

Figure 3.10: Electron (a) density and (b) temperature profiles on the outer target as a function of the distance from the strike point. The results obtained with EDGE2D-EIRENE (red diamonds) and TECXY (blue circles) refer to the DEMO reference scenario (table 3.1) with an upstream density $n_{e,LCMS} = 2.7 \times 10^{19} m^{-3}$. The diffusion coefficients are equal to $D_\perp = 0.32 m^2/s$, $\chi_{i,e} = 0.12 m^2/s$ for both calculations.

results are closer than the ones in terms of target density since the temperature peaks are located in the proximity of the strike point where the density are also closer. Furthermore, the differences in the density profiles shape reflect on a different shape of the target temperature, which is more spread in TECXY than in EDGE2D-EIRENE.

An analysis of the data shows that this behaviour is related to the different neutral particles description since the particle source in the continuity equation depends on the neutral densities. Clearly, since of the high temperature fields there is a weak dependence on the ionisation cross section. Figure 3.11 shows a zoom in the divertor region of the neutral density and pressure computed by EDGE2D-EIRENE (respectively 3.11a and 3.11b) and TECXY(respectively 3.11c and 3.11c). A difference of two order of magnitude is obtained in the two calculations. This directly affects the source terms in the mass balance equation originating the difference in the electron density profile.

Furthermore, the codes predict a different ionisation distribution which can be inferred by observing both the neutral density and pressure contour plots. In particular, while in EIRENE the ionisation predominantly occurs in the near target region, in TECXY the neutral particles are able to penetrate into the SOL due the description by means of the analytical function in eq. 2.20. This behaviour clearly disagrees with the characteristic of the low recycling regime and can explain the different electron density profile shape predicted by TECXY. Therefore, these results shows how the neutral description affects the target plasma conditions.

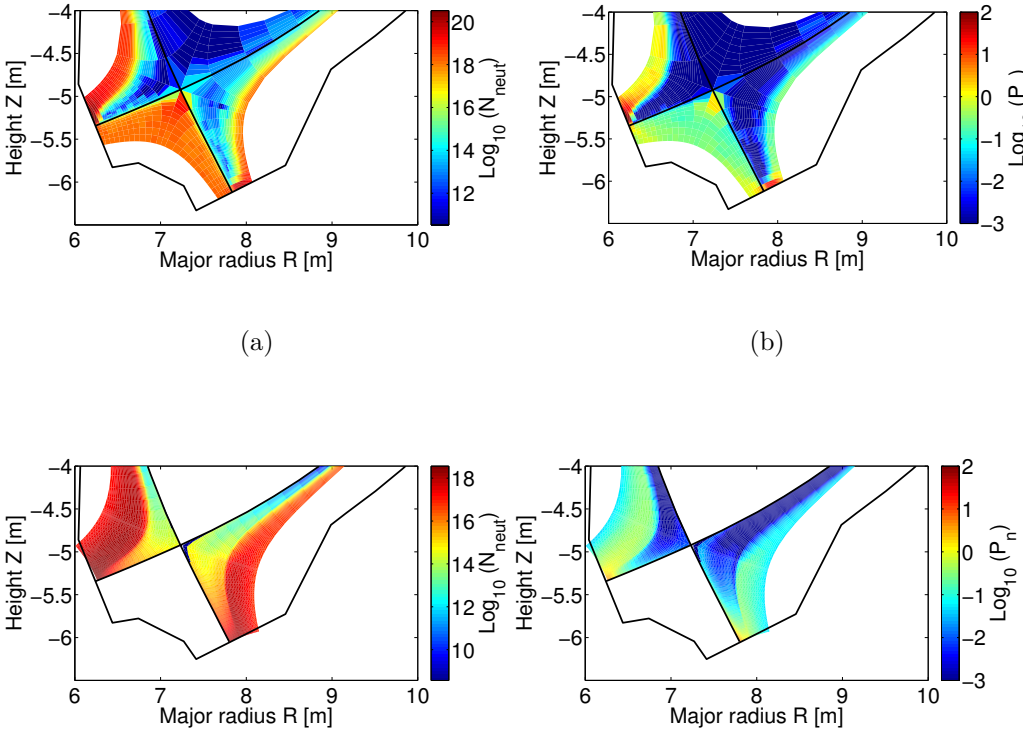

Figure 3.11: 2D contour maps of the (a), (c) neutral density and of (b), (d) the neutral pressure in the divertor area plotted in log scale. The figures on the top refer to the EDGE2D-EIRENE calculations while the ones on the bottom to TECXY. The simulations refer to an upstream density $n_{e,LCMS} = 2.7 \times 10^{19} m^{-3}$ and to the DEMO parameters given in table 3.1. The diffusion coefficients are set to $D_\perp = 0.32 m^2/s$, $\chi_{i,e} = 0.12 m^2/s$.

Despite the large difference observed in the density and temperature profiles, the power density fluxes predicted by the two codes match very well. The results in terms of heat flux profiles on the target plates for EDGE2D-EIRENE (red diamonds) and TECXY (blue circles) are depicted in figure 3.12. As can be seen, the two profiles overlap except for a slightly higher peak value in TECXY which is related to the absence of the PFR in the computational domain. This hypothesis is confirmed by calculating the integral value of the power inside the PFR in EDGE2D-EIRENE. By comparing the latter with the difference in the integral power in the first ring for the profiles obtained in the two calculations, we get a similar value.

In addition, a validation of the results in terms of power profiles is performed by

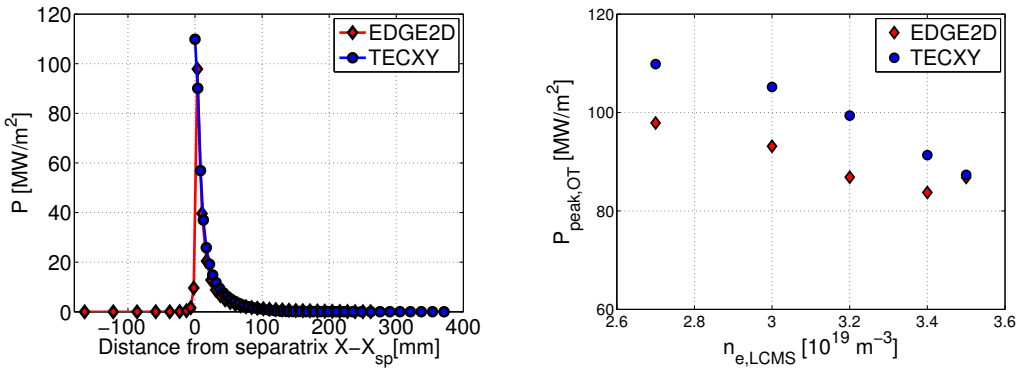

(a) (b)

Figure 3.12: (a) Power density profile on the outer target as a function of the distance from the strike point obtained by using EDGE2D-EIRENE (red diamonds) and TECXY (blue circles). The simulations refer to an upstream density $n_{e,LCMS} = 2.7 \times 10^{19} m^{-3}$. (b) Power peaks onto the outer target as a function of the upstream density. The DEMO reference scenario parameters are given in table 3.1. The diffusion coefficients are set to $D_\perp = 0.32 m^2/s$, $\chi_{i,e} = 0.12 m^2/s$ for both calculations.

considering the target boundary conditions. The parallel power can be evaluated by considering the density and temperature target profiles and the heat transmission coefficients (cf. section 2.3) $\gamma_i = 2.5$ and $\gamma_e = 4.5$. Similar values of the parallel heat flux profiles are obtained with the two codes data, confirming the correctness of the output quantities.

Finally, in figure 3.12b the comparison of the power peaks for the over all density scan are shown. The results of the two calculations are quite close, except the higher peak obtained in TECXY, and show the same decreasing trends as a function of the upstream density. Therefore, we can conclude that TECXY is suitable for the description of the SOL plasma behaviour in terms of power loads in case of 'well attached' plasma conditions albeit the difference in the local profiles of density and temperature.

Global quantities An important test of the reliability of TECXY involves the global quantities in terms of total power and volumetric losses. Figure 3.13 shows the results obtained in the two calculations. Both codes predict similar values of the integral power reaching the inner and outer divertor plates. However, the values calculated by TECXY (blue circles) are barely higher than the one obtained with EDGE2D-EIRENE (red diamonds). This behaviuor is related to the different volumetric sources computed by the analytical model of TECXY since the neutral density is underestimated with respect to EIRENE.

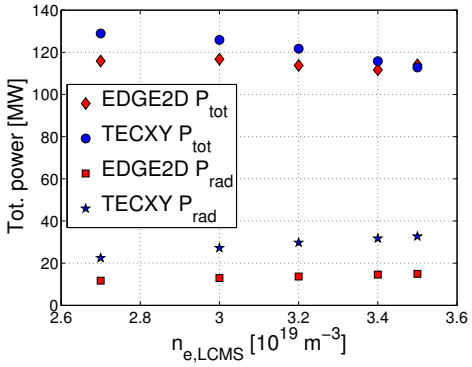

Figure 3.13: Total power reaching the inner and outer divertor plates as a function of the OMP electron density obtained by using EDGE2D-EIRENE (red diamonds) and TECXY (blue circles). The hydrogen radiation for the two codes are also shown with red squares (EDGE2D-EIRENE) and blue stars (TECXY). The input parameters for the simulations refers to table 3.1. The diffusion coefficients are set to $D_\perp = 0.32m^2/s$, $\chi_{i,e} = 0.12m^2/s$.

Most importantly, the trends predicted by the two numerical tools are quite similar and a weak dependence on the upstream density is observed in the whole density scan. Clearly, this behaviour correspond to a low recycling plasma regime where the effect of neutrals can be neglected and which does not affect the SOL conditions.

Finally, we can compare the results in terms of hydrogen radiation shown with red squares (EDGE2D-EIRENE) and blue stars (TECXY). As previously, higher peak values are obtained with the analytical model than with EIRENE albeit the neutral density shows an opposite behaviour. However, we have to consider that the radiation mainly occurs in the far SOL where the temperature fields are low. This effect combined with the high penetration of neutral particles in TECXY explain this behaviour. Similar trends are obtained in both the computations but the increase in TECXY (10 MW, $\approx 45\%$)is slightly higher than in EDGE2D-EIRENE (4MW, $\approx 27\%$).

Comparison of the diffusion coefficients scan results

As a final step of the benchmark, we compare the results of the two codes obtained by changing the diffusion coefficients while fixing the upstream density to $n_{e,LCMS} = 3.0 \times 10^{19} m^{-3}$. It is important to point out that the aim of this study is to evaluate the predicted trends as a function of the power decay length evaluated at the equatorial plane which is chosen as scanning parameter, disregarding the value and the ratio of $D_\perp$ and χ. More precisely, since of the different physical model adopted in the two calculations we are not interested in a perfect match of the λ_q

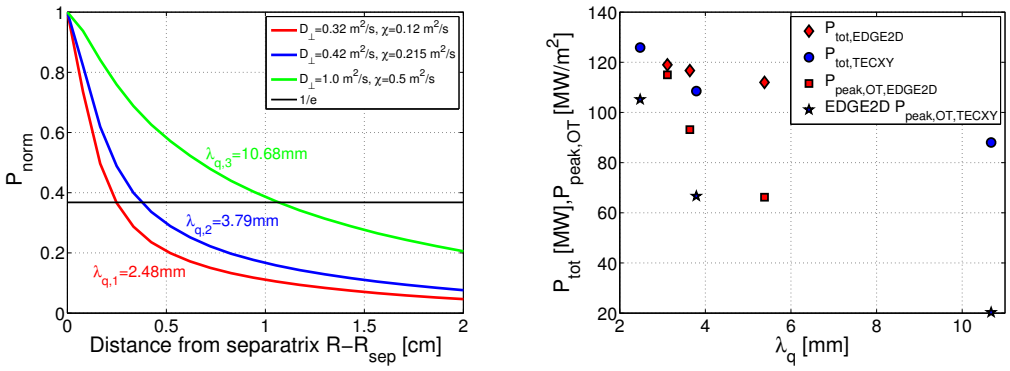

(a) (b)

Figure 3.14: (a)Normalized parallel power at the equatorial plane as a function of the radial distance from the separatrix obtained with TECXY. The diffusion coefficient are set to $D_{\perp,1} = 0.32m^2/s$, $\chi_{i,e,1} = 0.12m^2/s$ (red), $D_{\perp,2} = 0.42m^2/s$, $\chi_{i,e,2} = 0.215m^2/s$ (blue), $D_{\perp,3} = 1.0m^2/s$, $\chi_{i,e,3} = 0.5m^2/s$ (green). The corresponding power decay lengths are also shown. (b) Power peaks onto the outer target as a function of λ_q. The DEMO reference scenario parameters are given in table 3.1 and the upstream density is fixed to $n_{e,LCMS} = 3.0 \times 10^{19}m^{-3}$.

but rather in the prediction of its effect on the results in terms on power loads. Given this provisos, we can perform the analysis of the numerical results.

Figure 3.14a shows the normalized power flux obtained with TECXY as a function of the radial distance from the separatrix. The results refer to the three couples of diffusion coefficients $D_{\perp,1} = 0.32m^2/s$, $\chi_{i,e,1} = 0.12m^2/s$ (red), $D_{\perp,2} = 0.42m^2/s$, $\chi_{i,e,2} = 0.215m^2/s$ (blue), $D_{\perp,3} = 1.0m^2/s$, $\chi_{i,e,3} = 0.5m^2/s$ (green). The obtained power decay lengths are also given and are equal to $\lambda_{q,1} = 2.48m$, $\lambda_{q,2} = 3.79mm$ and $\lambda_{q,3} = 10.58mm$. Considering the previous results obtained with EDGE2D-EIRENE (figure 3.6), the two codes provides two different λ_q corresponding to the same value of the couple $D_\perp, \chi$. Bearing in mind that both perpendicular and parallel transport are described by the same physical model (cf. section 2.3) and that the effect of the neutral particles is negligible in the upstream region, this behaviour is related to the different boundary conditions imposed on the core side.

The predicted trends of the total power reaching the divertor and of power peaks are depicted in figure 3.14. As expected, due to 'well attached' plasma conditions, the total deposited power shows a weak dependence on the e-folding length λ_q in both codes. In addition, since P_{tot} remains approximately constant, the peak power is inversely dependent on λ_q in accordance with the predicted plasma conditions.

As a final remark, the benchmark of the EDGE2D-EIRENE and TECXY shows the possibility to use the latter to analyse the divertor plasma conditions not in terms of absolute values but in terms of general trends. Indeed, since in 'well

Table 3.3: Main parameters of the DTT reference SN scenario used for the EDGE2D-EIRENE simulations[10].

Parameter	Unit	Value
Major radius (R)	m	2.15
Aspect ratio (A)	-	3.1
Toroidal field (B_{tor})	T	6.0
Plasma current (I_p)	MA	6.0
Average density ($\langle n \rangle$)	$10^{20} m^{-3}$	1.7
Auxiliary power (P_{aux})	MW	45
Power crossing separatrix (P_{sep})	MW	37
(P_{sep}/R)	MW/m	17

attached' conditions the role of the neutral does not affect the SOL behaviour, we are allowed to use a more simple description of the neutral dynamics which allows to decrease the complexity of the code and, most importantly, to drastically reduce the computational time. Therefore, the similar numerical results in terms of both power loads on the divertor plates and general trends confirm the possibility to adopt TECXY as a fast tool to explore a wide range of possible parameters for the different configurations that can help in solving the power exhaust issue in order to study their different characteristics, as done for example in [51].

3.2 DTT simulations

Up to now, we have evaluated the SOL conditions and highlighted the criticality of a possible DEMO scenario. In the considered case of a pure deuterium plasma, numerical modelling predicts harsh conditions in terms of target power loads and electron temperature, totally unacceptable from an operational point of view. The next step in the analysis is the study of alternative divertor configurations by simulating the SOL plasma of DTT. In particular, the aim of this work is the identification of the different edge plasma features obtained either by changing the magnetic topology, i.e. by adopting an advanced divertor magnetic configuration, or by modifying the divertor target material, i.e. by using a liquid Lithium divertor. Both analyses are carried out by using EDGE2D-EIRENE.

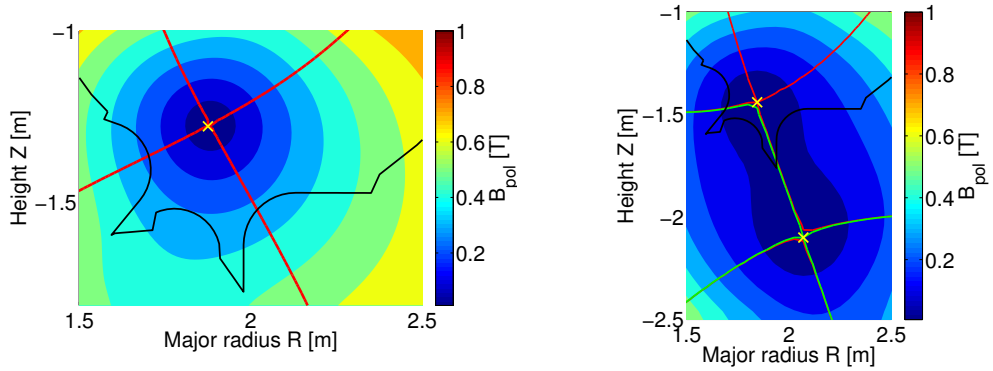

(a) (b)

Figure 3.15: Divertor zooms of the contour plot of B_{pol} in the (a) SN and (b) QSF divertor magnetic configurations of DTT. Red lines indicate the main separatrix, while for the QSF the secondary separatrix is depicted in green. The X points and the vessel wall are also given with yellow crosses and black line, respectively.

3.2.1 Advanced magnetic divertor configurations analysis

SN and QSF configurations

The main focus of the DTT machine, described in section 1.2.3, is the study of the power exhaust issue in DEMO relevant conditions. Indeed, one of the main design criterion is to ensure a high divertor flexibility. As a results, this tokamak machine is able to test a wide range of possible alternative configurations. The main geometrical parameter are given in table 3.3[10].

Among the different magnetic scenarios foreseen in DTT, we present a comparison of a reference SN scenario with a Quasi SnowFlake(QSF, as defined in [21]) one. The DTT reference scenario foresees an H-mode plasma with W divertor plates. The toroidal field and the plasma current are given by $B_{tor} = 6T$ and $I_p = 6.0MA$, respectively. Considering the parameters given in table and the scaling of eq. 3.1, we get $P_{LH} \approx 20MW$. A preliminary analysis of the total power entering the SOL is performed in [10] with the self consistent core-edge coupled code COREDIV. Different scenarios are taken into account by considering an input power $P_{aux} = 45MW$ and the possible injection of external impurities. Among the different scenarios, we simulate the most critical one where no external impurities are present and the core W radiation is low. More specifically, the core radiation account for $\sim 20\%$ and the predicted power crossing the separatrix is fixed to $P_{sep} = 37MW$. It should be noted that on one hand this power level is optimistic for the H-mode operation, since $P_{sep} \approx 2P_{LH}$, while on the other hand it is a precautionary value for the SOL and divertor conditions since of the low radiation level.

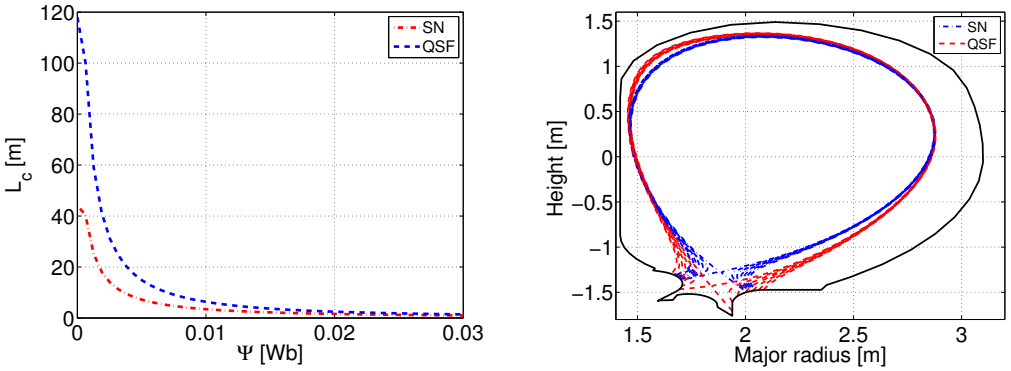

(a) (b)

Figure 3.16: (a) Connection length as a function of the flux surface coordinate for the SN (red) and QSF (blue) magnetic divertor configurations. (b)Sketch of the SN (red) and of the QSF (blue) flux surfaces in the poloidal plane showing the different flux expansion.

In order to highlight the features of the two different considered magnetic configurations, the contour plot of the magnetic poloidal field for the SN and QSF are shown in figure (3.15a) and (3.15b), respectively. First of all, as stated in the section 1.4.1, the QSF is characterized by the presence of a second null point (yellow cross on the bottom) outside the vessel wall. The different behaviour of B_{pol} near the main X-point is clearly visible: while in SN B_{pol} linearly increases with the distance from the separatrix, in QSF there is a 'flatness' in between the two nearby nulls. As a consequence, the flux surfaces spread out near the divertor target and there is an increase in the divertor volume and in the connection length L_c since the field lines runs almost toroidally. However, the poloidal magnetic field B_{pol} cannot be arbitrarily reduced since the grazing angle of the magnetic field line with the target surface is constrained to $\gamma > 1^\circ \div 2^\circ$. This limit is related to the need to shadow the leading edges of the individual tiles and also constrains the poloidal tilting of the target to $\theta \sim 20^\circ$.

The effects of the increase in the divertor volume and in L_c are shown in figure 3.16. Naturally, closer the magnetic field line to the X-point, higher the increase in L_c with a maximum at $r - r_{sep} \sim 0.3mm$ of $L_{c,SN} = 44m$ and $L_{c,QSF} = 118m$ for the SN and QSF, respectively. In addition, by observing figure 3.16b we can appreciate the different shape of the flux surfaces. In particular, the large increase in the flux expansion in QSF case is visible.

These two characteristics have an intrinsic mitigation effect on the power loads even if the possible benefit discussed in 1.4.1 are not taken into account. On one hand, the increase in f_x directly reflects on a large wetted area. This affect can be quantified by considering the near SOL, where most of the power is carried by ions

and electrons, and is simply given by $l_{t,QSF}/l_{t,SN}$, where l_t is the distance between two flux surfaces. This approximation clearly holds if the two configurations are characterized by the same upstream decay length. On the other hand, the increase in the connection length means a longer dwell time τ_w for the particles to reach the target. As a consequence, there is an increase in the cross field diffusion both for particle and energy. Considering that the cross filed length $\lambda \propto \sqrt{L_c}$, the global effect deriving from the topology is given by geometrical factor f_r:

$$f_r = \sqrt{\frac{L_{c,QSF}}{L_{c,SN}}} \frac{l_{t,QSF}}{l_{t,SN}}. \tag{3.6}$$

This factor can be then compared to the decrease in the power peaks in order to assess if some additional effects, that is an increase in the volumetric losses, could be originated by the use of an advanced magnetic configurations, as seen for example in numerical simulation[21],[51],[52].

EDGE2D-EIRENE Inputs

A pure deuterium plasma is taken into account since we are simulating the worst scenario where no external impurities and low core radiation are foreseen. Most importantly, the primary aim of this work is to identify the different plasma behaviours obtained by the change of the divertor magnetic configuration. In addition, the attainment of detached regime is studied by increasing the upstream density in the two cases. Therefore, the actual geometry of the vessel is considered since of the effect of the divertor closure.

The first input to consider is the mesh for the EDGE2D-EIRENE calculations. While the generation of the mesh in SN case is straightforward, in QSF configuration we face out some problems. Figure 3.17 shows the mesh obtained with GRID2D, where the three different sub-domains (core, SOL and PFR in blue, red and green, respectively) are shown. As stated in section 2.3.1, GRID2D is able to treat standard SN cases since there are problems in handling the presence of a second null point. As a consequence, the mesh generation obtained by considering the original computational box yields to failure of the code. Since the second null point is located far from the vessel wall, a redefinition of the domain is possible in order to exclude the second X-point, shown in figure with the black cross on the bottom. The new domain is given in figure with a red box where the presence of the main X-point alone is clearly visible.

The main input parameters in the simulations refer to the reference values reported in table 3.3. The pumping surfaces are located in the PFR region for both the configurations with an albedo $\alpha = 0.94$, while the recycling coefficients are set to $R_c = 1$. The external deuterium puff is feedback controlled by imposing the upstream separatrix density. Even though we are modelling a H-mode scenario, we use constant transport coefficient set to $D_\perp = 0.15 m^2/s$ and $\chi_{i,e} = 0.35 m^2/s$.

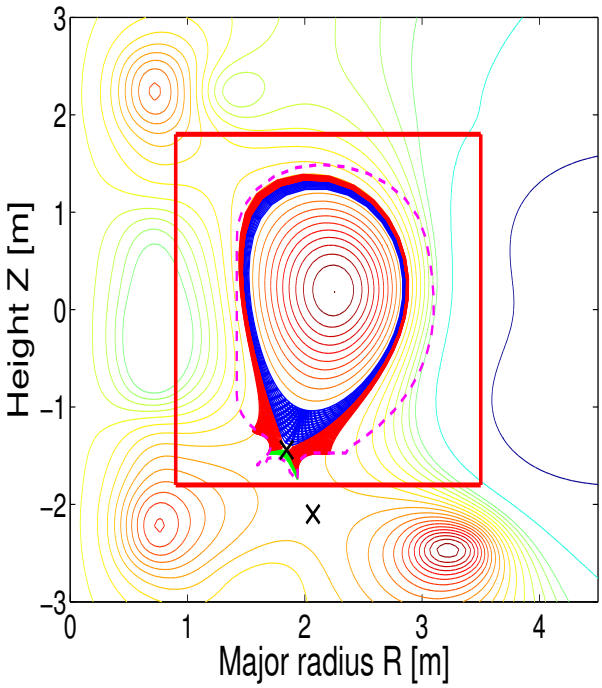

Figure 3.17: Mesh used to simulate the SOL plasma of the DTT in QSF configuration. As previously, the SOL is depicted in red, the core in blue and the PFR in green. The original computational box and a contour map of the flux surfaces are given. The redefined domain for the GRID2D mesh generator is highlighted with the red box. The two X-points are also shown with black crosses. The magenta line is the vessel wall.

As far as the EIRENE calculations are concerned, two different models are used in the density scan. For low density, where the plasma is far from the detachment condition, the default EIRENE model is set. However, for high density cases, the target plasma start to detach and a more accurate description is needed. Therefore, the Kotov-2008 [53] setup is used since it is more suited than the standard one. In particular, in this model a more extensive set of elastic and inelastic collision between Deuterium ions and molecules is included.

Results

In order to study the SOL conditions and the possible differences arising from the change of magnetic topology, a density scan is perfomed. By referring to [10], we consider the three main foreseen scenarios: low, reference and high density scenarios corresponding to $n_{e,LCMS} = 0.5,\ 0.75$ and $1.0 \times 10^{20} m^{-3}$, respectively. In addition, two further points in the density scan, i.e. $n_{e,LCMS} = 1.2$ and $1.4 \times 10^{20} m^{-3}$, are

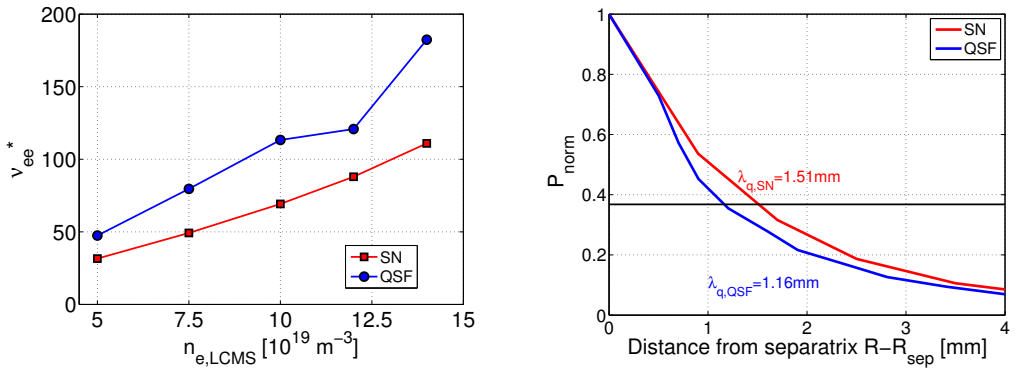

(a) (b)

Figure 3.18: (a) Upstream electron collisionalities for SN(red squares) and QSF (blue circles) configurations against the upstream density. ν^*_{ee} are calculated by using eqs. 3.4. The upstream conditions are evaluated on the first SOL ring which corresponds to $r - r_{sep} \sim 0.3mm$. (b) Upstream radial profiles of the normalized parallel power for SN (red) and QSF (blue). The values of the obtained decay length are also given. The simulations refers to P_{sep}=37MW and diffusion coefficients $D_\perp = 0.15m^2/s$ and $\chi_{i,e} = 0.35m^2/s$.

considered in order to assess the effect of the magnetic geometry on the attainment of the detached regime. It is worth noting that the latter two density values are consistent with the Greenwald density limit and correspond to $0.3n_{GW}$ and $0.35n_{GW}$, respecitvely, where n_{GW} is the Greenwald limit given by:

$$n_{GW} = \frac{I_p}{\pi a^2} = 3.89 \times 10^{20} m^{-3}. \tag{3.7}$$

However, we should note that the Greenwald fractions refer to separatrix density in place of the bulk density, both in terms of top pedestal density or average plasma density. For instance, if we consider the multi machine scaling in [54], we get $n_{e,ped}/n_{e,LCMS} \approx 2$ for $n_{e,LCMS} = 0.3n_{GW}$ and $0.35n_{GW}$, that means a Greenwald fraction of $\sim 0.6 \div 0.7$ for the considered upstream density values.

Evaluation of SOL plasma conditions The analysis starts by considering the upstream conditions. Figure 3.18a depicts the electron upstream collisionality ν^*_{ee} calculated by means of eq. 3.4 evaluated on the first SOL ring corresponding to $r - r_{sep} \sim 0.3mm$. Both configurations shows an increasing trend of the upstream collisionality, which is quite high also in case of low density. In this scenario, the code foresees a plasma in high recycling regime. Increasing the density the plasma conditions move towards a detached regime. However, the QSF case is more prone that SN to reach detachment. Indeed, the two configurations show a difference in

ν^*_{ee} that is higher in QSF than SN in the over all density scan ($\nu^*_{ee,QSF}/\nu^*_{ee,SN} \sim 1.5$). As a consequence, while in case of QSF the detachment starts in the high density scenario and then the divertor conditions approach a fully detached regime for $n_{e,LCMS} = 1.4 \times 10^{20} m^{-3}$, in case of SN we observe only an incipient detachment condition for the highest value of the density. Hereafter, a validation of this results is performed by studying the evolution of outer target quantities and recognizing the typical detachment indications, e.g. the density roll-over (cf. section 1.3.3).

The higher values ν^*_{ee} in QSF than in SN are essentially caused by the increase in the connection length which directly reflects on an increase in ν^*_{ee}. For the considered SOL ring we have $L_{c,QSF}/L_{c,SN} = 4.7$. However, a change of the upstream conditions is observed. Bearing in mind that the upstream density is fixed, this opposite effect is related to a change of the separatrix temperature in QSF albeit all the setup of the simulations are equal. More specifically, we get $T_{e,LMCS,QSF} \sim 1.3 T_{e,LMCS,SN}$.

The different upstream conditions also reflect on a different power decay lengths. As shown in figure 3.18b, the normalized parallel power flux profiles ($P \propto n_e T_e^{3/2}$), calculated by referring to the lowest density, are narrower in case of QSF. As a results, we get different values of the power e-folding length respectively given by $\lambda_{q,SN} = 1.51mm$ and $\lambda_{q,SN} = 1.16mm$. The obtained values agree with the value of $\lambda_{int} = 1.7$ mm reported in [10] calculated with the scaling in [13].

Clearly, the different widths of the relevant channel for the power deposition on the target plates have to be taken into account, that is a correction factor of $\lambda_{q,SN}/\lambda_{q,QSF}$ is applied to the geometrical factor f_r (eq. 3.6).

Once evaluated the conditions at the equatorial plane, we can analyse the SOL plasma behaviour in the divertor region. As previously, the analysis focus on the outer divertor only, since it is the most critical in terms of heat loads.

Figure 3.19 shows the electron temperature on the outer target both in terms of profiles along the X coordinate on the target plate (3.19a) and the strike point temperatures (3.19b). In the former plot the results obtained in the three density scenarios for SN (red) and QSF (blue) configurations are reported. First of all, we can observe that in case of low density the temperature peak is higher in QSF than in SN case that is a direct consequence of the different upstream temperatures. This is consistent with the plasma condition found with the collisionality analysis since the plasma is in conduction limited regime. Therefore, the volumetric losses are of minor importance. In addition, the increase in the connection length is of minor importance because of the high temperature field distribution.

As the upstream density is increased, the temperature peaks in the near SOL of QSF reaches (in the reference scenario) and then falls (in high density scenario) below the corresponding peaks in SN case since the volumetric sources becomes more and more important. In case of QSF, for an upstream density of $n_{e,LCMS} = 1.0 \times 10^{20} m^{-3}$ an incipient detachment state is found which is confirmed by the peak value of $T_{e,peak} = 6eV$. On the contrary, in SN case the electron temperature peaks remain

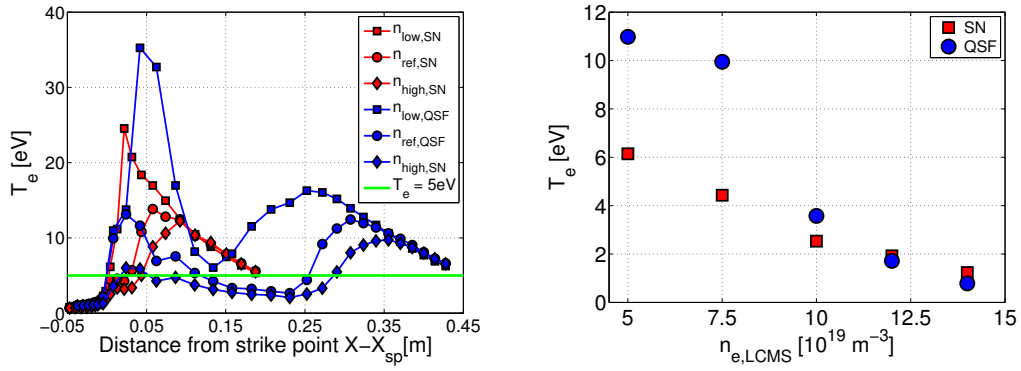

(a) (b)

Figure 3.19: (a) Profiles of the electron temperature on the outer target for the three different density scenarios: low (squares), reference (circles) and high (diamonds) density. The red curves refer to SN, while the blue ones to QSF. The threshold $T_e = 5eV$ is also given in green. (b) Outer strike point electron temperatures as a function of the upstream density for SN (red squares) and QSF (blue circles) configurations.

slightly higher than $T_{e,peak} = 10eV$ which is a clear indication of the conduction limited regime that is also found with $\nu^*_{ee,u}$.

By increasing the density, the strike point temperatures fall below the $T_e = 5eV$ (see figure 3.19b) in both configurations reaching conditions where the recombination may represent the dominant process. These results seem in contrast with the divertor conditions inferred from the collisionality. On the other hand, by considering the temperature profiles, while in QSF T_e remains below the $T_e = 5eV$ threshold along most of the target plate, especially for the highest density, in case of SN there is an increase of T_e and peak values are shifted, as is also visible in figure 3.19a.

Secondly, a different shape of the profiles is found for the two magnetic configurations. These results are coherent with the shape of the SOL and of the mesh on the outer target plate. By referring for example to figure 3.20c, the reversal of the temperature profile in QSF is located where the vessel change inclination with respect to the poloidal flux surfaces. As a consequence, while in the proximity in the strike point the neutral particles are remitted towards the separatrix, in the far SOL they are remitted in the outer part of the SOL itself; in turn, this reflects in a reduction of the volumetric source by re-ionisation and recombination. Figure 3.20c and 3.20d shows the ionisation and recombination distribution in the divertor region for the QSF case. The contour plots refer to the low density scenario. A sharp decrease in the two sources is observed when the vessel switch from close to open geometry thus confirming the role of the remitted neutral particles on the temperature profiles.

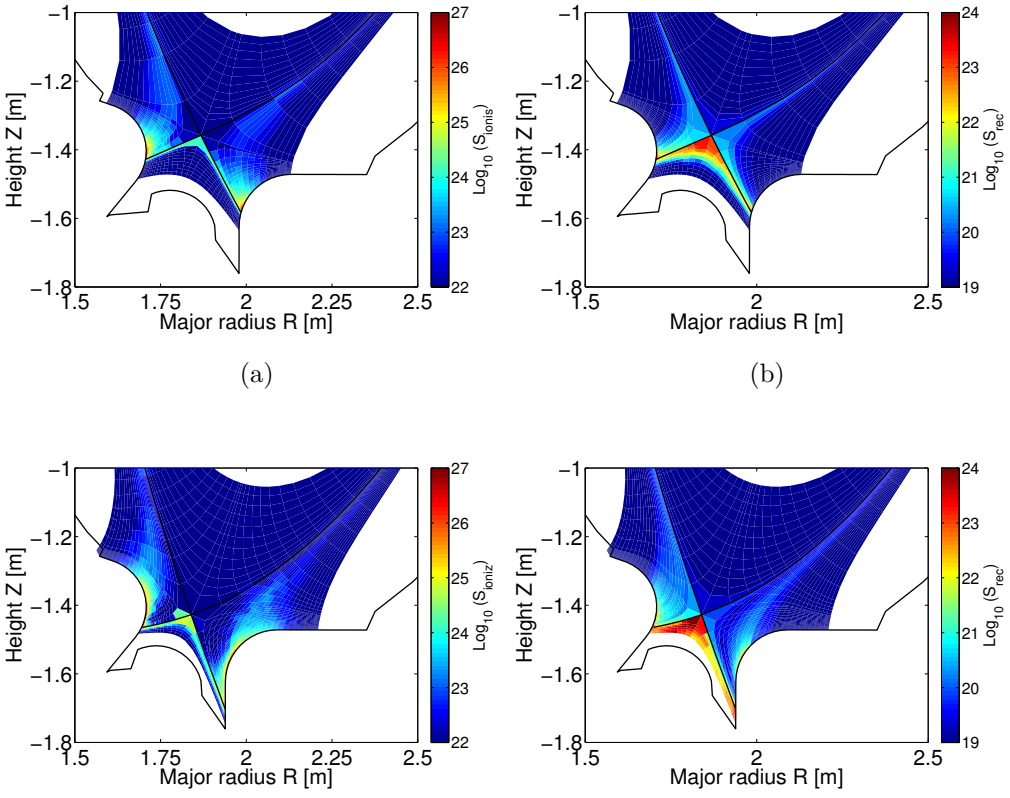

Figure 3.20: 2D contour maps of the (a), (c) ionisation and (b), (d) recombination sources in the divertor region plotted in log scale. The figures on the top refer to the SN calculations while the ones on the bottom to QSF. The simulations refer to an upstream density $n_{e,LCMS} = 5 \times 10^{19} m^{-3}$ and to the diffusion coefficients couple $D_\perp = 0.15 m^2/s$, $\chi_{i,e} = 0.35 m^2/s$.

Furthermore, different ionisation and recombination distributions are observed in the near SOL by changing the magnetic topology. In particular, while in SN both ionisation and recombination fronts are able to penetrate along the separatrix, in QSF they are located in a narrow layer near the target or in the far SOL region. This feature of the QSF is retained also in the highest density case, where a fully detached state is reached, and reflects in a stabilizing effect. Hereafter, this point is discussed more in details by analysing the neutral particles behaviour.

A further analysis on the SOL behaviour is performed by considering the strike point electron density (3.21a) and the maximum ion saturation current (3.21b) on the outer target. In the plot on the left we can see the different behaviour in terms of target density corresponding to the two different configurations. While in SN there

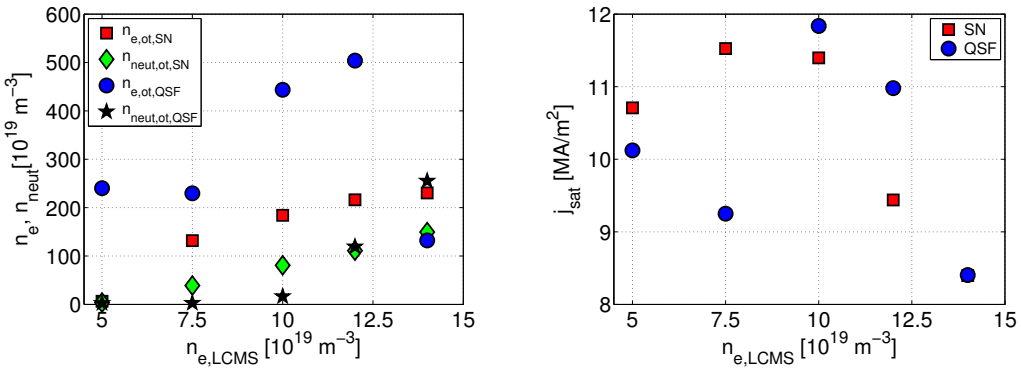

(a) (b)

Figure 3.21: (a) Target density at the outer strike point as a function of the upstream density for the SN (red squares) and QSF (blue circles). The local values of the neutral density are also shown (green star for SN and black diamonds for QSF). (b) Maximum of the ion saturation current on the outer target as a function of upstream density for SN and QSF (red squares and blue circles, respectively).

is a continuous increase in n_t by increasing the upstream density with a saturation at the end of the density scan, in QSF the saturation is foreseen by the code in the high density scenario ($n_{e,LCMS} = 1.0 \times 10^{20} m^{-3}$) and a clear indication of the density roll-over is observed. This results is in accordance with the previous prediction on the target plasma conditions. In addition, the results are further validated by considering the corresponding values of the total neutral density (both atomic and molecular) since when the QSF reaches the detachment regime the recombination processes become dominant, while in SN this is not observed.

Finally, an analysis of the maximum ion saturation current is performed. Figure 3.21b shows the evolution of $J_{sat,max}$ as a function of the upstream density. As expected, a roll-over of $J_{sat,max}$ is observed for the QSF in the high density scenario, followed by a sharp decrease in the highest density case. However, we also observe a roll-over for the SN case, which is in contrast with the previous results. The reason for this behaviour is not yet understood and the analysis is still under investigation.

Analysis of the power loads Figure 3.22a shows the profiles of the heat flux density onto the outer target for the low (squares), reference (circles) and high (diamonds) density scenarios in case of SN (red) and QSF (blue) magnetic configurations. A large difference in terms of power peaks is foreseen by the code. As far as the SN is concerned, the obtained values of the power peaks are totally unacceptable for an operational point of view. In particular, even in case of high density scenario we get $P_{peak} > 40 MW/m^2$. In addition, the power profiles are quite narrow and characterized by a deposition width of $l_{t,SN} = \lambda_q * f_x = 8.5 mm$, where f_x is the flux

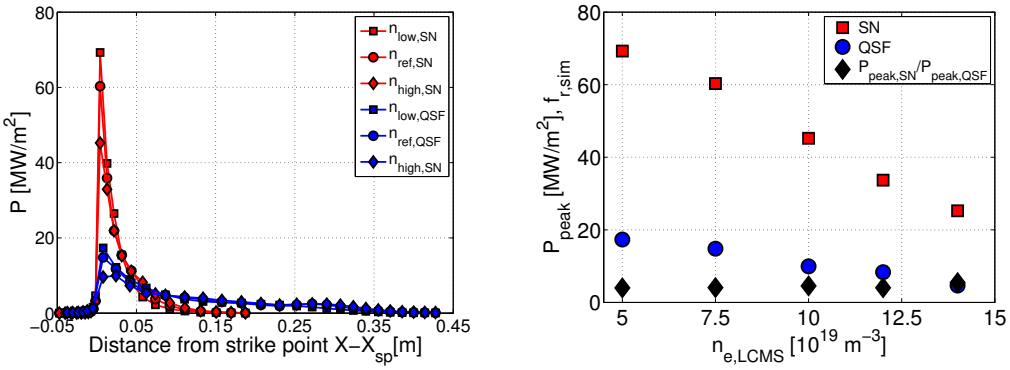

(a) (b)

Figure 3.22: (a)Power density profiles on the outer target as a function of the distance from the strike for the low (squares), reference (circles) and high (diamonds) density scenarios. The red curves refer to SN while the blue to QSF. (b) Power peaks in the two magnetic configurations (red squares for SN and blue circles for QSF). The reduction factors obtained in the simulations, $f_{r,sim} = P_{peak,QSF}/P_{peak,SN}$ are also shown with black diamonds. The simulations refer to an input power $P_{sep} = 37MW$ and to the set of diffusion coefficients $D_\perp = 0.15m^2/s$ and $\chi_{i,e} = 0.35m^2/s$.

expansion defined in eq. 1.9 given by $f_{x,SN} \sim 6$.

However, it is important to point out than in the SN case the separatrix is approximately perpendicular to the target plate, as can be seen in the contour plots 3.20. As a consequence, the power peaks can be reduced by target tilting, for instance by shifting the separatrix strike point on the vertical tiles. If we consider a value of the poloidal angle as in QSF $\theta = 22°$, we get $P_{peak,tilt} \sim 17MW/m^2$. This is a threshold limit for the target materials considering the pulse length and the number of discharge planned for the DTT machine. Clearly, the predicted power loads are even worse in case of reference density scenario. Therefore, the injection of external impurities is mandatory in order to increase the radiated power fraction into the SOL and to reach tolerable values.

By increasing the density beyond the values foreseen in the three main scenarios, the power peaks (figure 3.22b) clearly decrease but remain higher than the threshold of $10MW/m^2$ foreseen for a fusion reactor as DEMO. This situation is also met for the highest density taken into account, where the plasma starts to detach.

On the contrary, in case of QSF configuration we get manageable values of the power peaks, which are lower than $15MW/m^2$ in the overall density scan. The heat flux profiles are flatter than the one in SN and are characterized by a power deposition width of $l_{t,QSF} = 2.7cm$ and a flux expansion $f_{x,SN} \sim 25$. A value of the power peak smaller than the $10MW/m^2$ is obtained for the high density scenario. It seems therefore reasonable to forecast pure deuterium plasma discharges in high

Table 3.4: Summary of the integral power values for the SN and QSF magnetic divertor configurations of DTT with $P_{SOL} = 37MW$. The power peaks are also given. The topological reduction factor obtained by considering eq. 3.6 is $f_r \approx 5.3$.

	SN					QSF				
$l_t[cm]$	0.85					2.7				
$n_{e,LCMS}[10^{20}m^{-3}]$	0.5	0.75	1.0	1.2	1.4	0.5	0.75	1.0	1.2	1.4
$P_{peak,OT}[MW/m^2]$	69.3	60.3	45.2	33.7	25.2	17.3	14.8	9.9	8.3	4.6
$P_{tot,OT}[MW]$	19.4	19.2	18.4	17.8	16.6	18.1	18.1	17.6	17	14
$P_{rec,OT}[MW]$	3.4	5.8	7	7.6	7.9	2.6	4.8	6.7	7.7	7.2
$P_{tot,IT}[MW]$	13.7	13.1	11.6	11.4	10.2	15.4	14.1	12.9	11.8	12
$P_{rec,IT}[MW]$	3.3	5.3	5.5	6.1	7.1	2.6	4.9	6.4	6.7	7
$P_{At.ions.}[MW]$	1.7	5.6	7.1	7.6	7.9	0.5	4.6	7.3	8.5	9.4
$P_{Mol.ions.}[MW]$	0.85	1.5	2.5	3.7	5.3	0.7	1.3	2.2	3.2	4.1
$P_{CX}[MW]$	6.27	6.2	6.3	6.5	6.6	6.1	5.9	6.63	6.7	7
$P_{Hyd.rad.}[MW]$	1.28	2.3	3	3.3	3.8	1.4	2.4	3.1	3.7	4
$P_{tot,vol}[MW]$	10.2	15.7	19.9	21.2	23.6	8.7	14.2	19.3	22.1	24.6

density case without the presence of external impurities. For the highest density cases featured by a detached plasma conditions, the power density profiles are very flat and we get $P_{peak,QSF} < 5MW/m^2$.

As previously stated, in order to evaluate the physical mechanisms leading to a decrease in the power peaks in QSF and to flatter heat flux density profiles, we can compare the ratio of the peak power obtained in the simulations for SN and QSF, i.e. $f_{r,sim} = P_{peak,QSF}/P_{peak,SN}$, against the topological reduction factor defined in 3.6. By considering a connection length corresponding to the first SOL ring $L_{c,SN} = 44m$ and $L_{c,QSF} = 118m$, we get:

$$f_r = \sqrt{\frac{L_{c,QSF}}{L_{c,SN}}} \frac{l_{t,QSF}}{l_{t,SN}} = 5.3, \tag{3.8}$$

where $l_{t,SN}$ and $l_{t,QSF}$ are the distance of the flux surface on the target plate reported in table 3.4. It is important to point out that the latter refers to $\lambda_{q,SN} = 1.51mm$ and $\lambda_{q,QSF} = 1.16mm$; therefore, we take into account the correction factor related to the narrower upstream parallel heat flux density profile in QSF than in SN.

Figure 3.22b shows the $f_{r,sim}$ obtained as a function of the upstream density. Additionally, the power peaks are also given in table 3.4. For the different values of the upstream density we get almost the same power peaks reduction, which ranges from $f_{r,sim} = 4$ for the low density to $f_{r,sim} = 5.4$ for the highest considered density

case. Since the obtained values are close to the reduction factor caused by the change of topology, we deduce that the mitigation effect is primarily due to the geometrical features of the two magnetic configurations. In particular, considering the two terms on the r.h.s of eq. 3.6, we see that the most driving effect is related to the higher increase in the flux expansion than to the increase in L_c.

This results is consistent with the foreseen SOL plasma conditions. Bearing in mind that we simulate a pure deuterium plasma and considering the ionisation energy for deuterium is $E_{ion} = 13.6eV$, due to the high temperature field the increase in L_c is not able to give rise to an increase in the radiation power. For DTT, the effect of the magnetic divertor configurations on the high radiative regime where external impurities are injected into the plasma can thus represent an interesting future study.

To validate this results we perform an analysis of the integral quantites in terms of total power load onto the divertor plates and volumetric source. The obtained results are given in table 3.4. First of all, we can observe the same decreasing trend of the total power deposited both on inner and outer target. By focusing on the outer outer divertor plate, we get a a comparable decrease in the total power given by $\Delta P_{tot,SN} = 2.8MW$ (14 %) and $\Delta P_{tot,QSF} = 4.1MW$ (22 %). However, a substantial increase in the recombination power deposited onto the target is provided by the code since the plasma moves from high recycling (low density scenario) to detached regime ($n_{e,LCMS} = 1.4 \times 10^{20} m^{-3}$).

As far as the the volumetric sources are concerned, the results shows a similar increase in both configurations. In particular, the radiated power by deuterium atoms are very close in the two magnetic configurations. This confirm the pivotal role played by the geometrical factor as well as the minor effect of the increase in L_c on the radiative performances. Moreover, the CX processes represent a remarkable part of the total volumetric source, especially in the low density scenario.

By increasing the density, the highest increase is related to the ionisation process (both atomic and molecular), which is a sign of the change in the divertor conditions and of the higher and higher neutral particles recycling that occurs at the divertor target.

Finally, considering the total power deposited on inner and outer divertor tiles, a different power sharing is observed in the two configurations. In particular, the ratio P_{out}/P_{in} is smaller in QSF than in SN. This behaviour can be probably related to the churning mode explained in section 1.4.1. However, a more accurate study of the power sharing should also consider the effect of the drifts which are turned off in the numerical simulations. These cross fields drifts, primarly $\mathbf{E} \times \mathbf{B}$, ∇B and centrifugal drifts, give rise to diamagnetic poloidal flows which can change the in/out divertor asymmetry[1].

[1]For an exhaustive explanation on how the drifts can affect the in/out asymmetry the reader

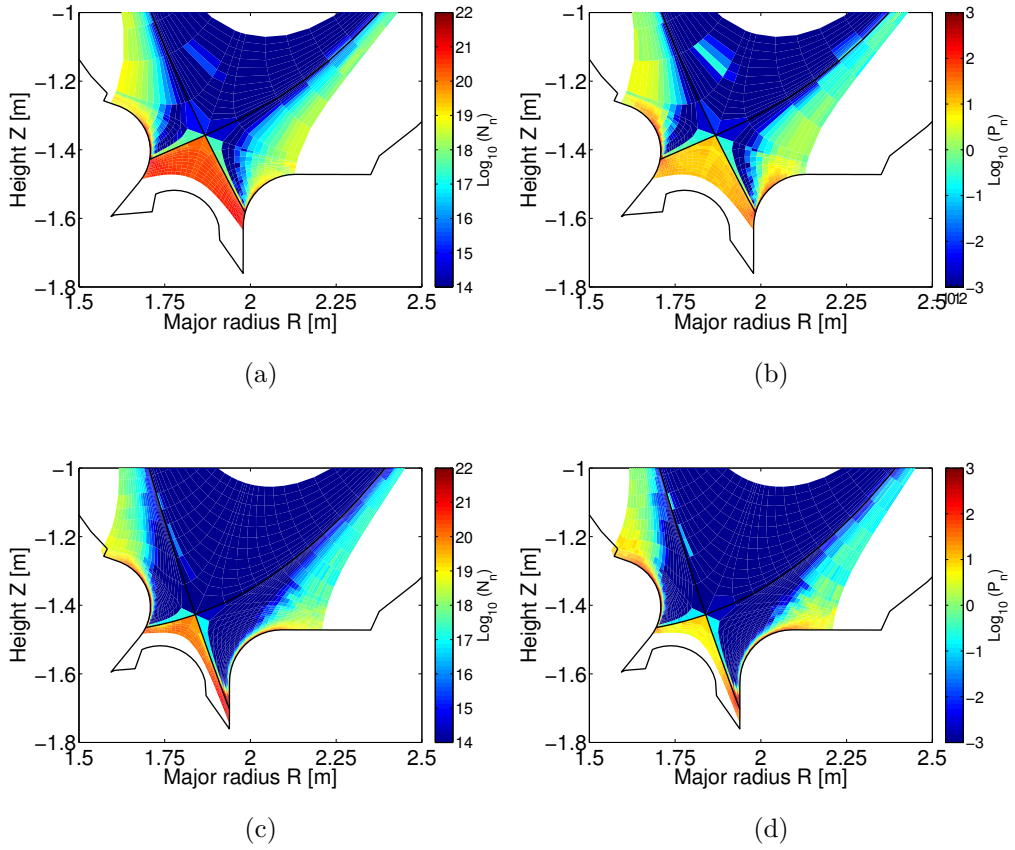

Figure 3.23: 2D contour maps of the (a), (c) neutral density and (b), (d) pressure in the divertor region plotted in log scale. The plots on the top refer to the SN while the one on the bottom to QSF. The simulations refer to an upstream density $n_{e,LCMS} = 1.4 \times 10^{20} m^{-3}$, an input power $P_{sep} = 37MW$ and to the diffusion coefficients couple $D_\perp = 0.15 m^2/s$, $\chi_{i,e} = 0.35 m^2/s$.

Neutral particles behaviour The last point in the analysis of the change of topology focuses on the effect on neutral particles. Indeed, since a stable detachment is mandatory for a future DEMO machine, it is essential to study how the detachment front evolves and if possible stabilizing effect could arise by adopting different configurations.

The contour plots of the neutral density and of the neutral pressure for SN and QSF cases are shown in figure 3.23. These plots refer to the highest density case, i.e. $n_{e,LCMS} = 1.4 \times 10^{20} m^{-3}$, since it corresponds either to a detached regime or

is referred to chapter 18 in [28].

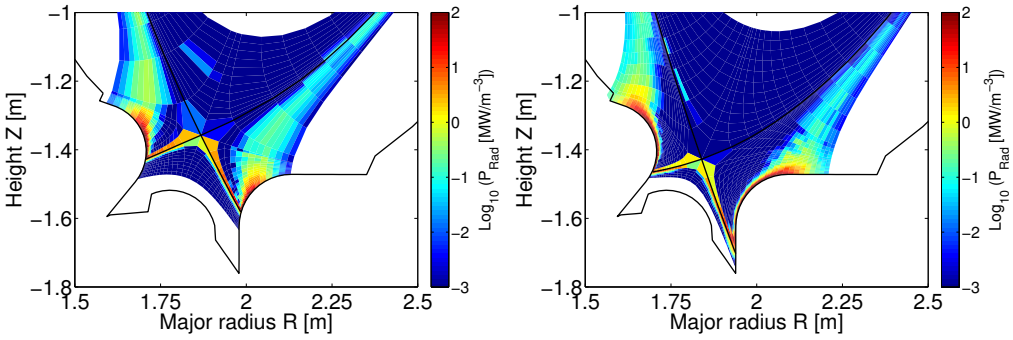

(a) (b)

Figure 3.24: 2D contour maps of the deuterium radiation distribution in the divertor region plotted in log scale for the (a)SN and the (b)QSF. The simulations refer to an upstream density $n_{e,LCMS} = 1.4 \times 10^{20} m^{-3}$, an input power $P_{sep} = 37MW$ and to the diffusion coefficients couple $D_{\perp} = 0.15 m^2/s$, $\chi_{i,e} = 0.35 m^2/s$.

to the start of the detachment for QSF and SN, respectively. A different neutral behaviour is observed in the two cases. Even though in the standard configuration a fully detached regime is not reached, a higher penetration of the neutral particles than in QSF is visible. This condition is observed in both the divertor legs. Indeed, for QSF in both plots we see that neutral particles in the near SOL are confined in a narrow layer near the target plates and only the neutral in the far SOL region tends to spread out. However, this condition is not met in close proximity to the separatrix, where the neutrals show a similar behaviuor in both cases.

Since of the different closure of the outer target, one of the possible reasons can be related to the remission paths. However, since the same different behaviour is observed in the HFS where both SN and QSF are featured by the same vessel geometry, we tend to exclude this possibility and the role played by the geometry itself.

Bering in mind that the QSF configuration is a transition from XD to SF and that in the considered QSF configuration the flux surfaces slightly flares in the target regions, a possible explanation for the different neutral particles penetration can be related to the stabilizing effect characterizing the XD configurations, as explained in section 1.4.1. This hypothesis is confirmed by the characteristic of the ionisaton front which in QSF remains well attached to the target plates, except for the narrow layer near the separatrix.

Finally, we analyse the radiation distribution for both cases (figure 3.24). First of all, we can see that while in the QSF the strongly radiating region is distributed along all the divertor plates, in SN the radiation is more concentrated near the strike point,

thus confirming the SOL plasma condition previuosly found. Most importantly, as a results of the better neutral confinement in QSF than in SN and considering the different plasma regimes characterizing the two cases, we observed a more stable high radiating region just in front of the target plates in QSF. Nonetheless, also in case of QSF the movement of neutral particle in the close proximity to the separatrix (the yellow narrow layer in figure) could lead to a MARFE (cf. section 1.4.1) but the situation seems less critical than in SN.

Collectively, these results shows that the use of the advanced configurations can represent a promising tool for the handling of the high power loads on the divertor target. The change of the magnetic topology affects the attainment of the detachment and, most importantly, is able to spreads the power on larger area even considering the geometrical factor only. However, it is important to predict the effect on the radiation performance in case of external impurity seeding. Furthermore, the change of the magnetic divertor configuration also affect the neutral particle behavior since a more stable detachment is observed in the QSF case. This property is particularly important in view of a DEMO machine, since stable fully detached state are mandatory to prevent excessive target material erosion.

3.2.2 Liquid Lithium divertor

The use of liquid metal as target material represents a different solution proposed by the fusion community to mitigate the power issue. As discussed in section 1.4.2, a liquid surface is able to withstand higher thermal loads than a solid surface and can give rise to a self healing process also known as vapor shield effect. In this section a preliminary study of a liquid Lithium divertor for the DTT machine is presented. The results are then compared with the reference SN scenario with W divertor plates in order to assess if the change of the target material could lead to beneficial effects on the power loads.

EDGE2D-EIRENE setups

While liquid metal limiters has been successfully tested on different tokamak machines as T-11M[55] and FTU[26], a precise design of a liquid metal divertor is not yet available. So far, liquid metals have never been used for a divertor; different possible conceptual designs have been proposed for instance by Goldston *et al* [56], which is based on a vapour box divertor, or by Lyublinski *et al*[57], based on a CPS system.

Among the different liquid metal, we choose lithium since it is one of the possible candidate which has been largely tested in present tokamak machines. As a consequence, an extended database is available for the numerical computation. The presence of the lithium liquid wall is taken into account by setting Li as intrinsic impurity. It is worth noting that in order to simulate the presence of Li a peculiar

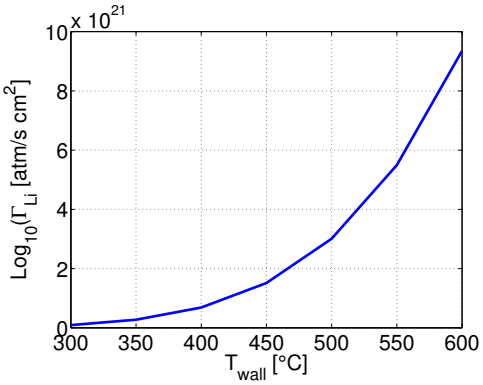

Figure 3.25: Evaporation of Lithium($atoms/scm^2$) in vacuum as a function of the temperature.

version of the EDGE2D-EIRENE code is used, where the Li database is implemented and such that EIRENE can treat the Li neutral atoms and the liquid Li wall[2].

In this work, as a first approximation we disregards any real liquid metal divertor configuration since we are interested in a preliminary scoping study. Indeed, the aim of this analysis is to asses if the change from solid to liquid wall could originate some possible mechanisms able to alleviate the power loads on the divertor targets. The presence of the liquid wall is simply defined by imposing a Li divertor into the code, while keeping the W as first wall material.

The main inputs for the simulations (e.g. P_{sep}, diffusion coefficients, etc.) refer to the standard SN reference scenario of DTT given in table 3.3. As far as the Li setup are concerned, we set the same particles diffusion coefficient of the deuterium atoms, that is $D_{\perp,Li} = D_{\perp} = 0.15m^2/s$. In addition, it is considered as a non recycling impurity since the causes leading to numerical instabilities and code crashes in case of Li recycling are not yet fully understood and they still are under investigation.

Finally, an important remark should be made on the evaporation properties of the liquid Li. As discussed in section 1.4.2, the evaporation rate is a strong function of the wall temperature which, in turns, is determined by the deposited power flux. This strong dependence is shown in figure 3.25[3]. While for Li temperature, that is T_{wall}, below $T_{Li} = 450\ ^{\circ}C$ the evaporation rate Γ_{Li} remains low, for higher value of T_{Li} a sharp increase is observed. This bahaviour reflects in the vapour shield effect. Therefore, it is essential to model this physical process in order to accurately estimate the effect of a liquid metal divertor.

Unfortunately, the current version of EDGE2D-EIRENE is not able to model the evaporation process, while the sputtering is taken into account. Consequently, in this

[2]The EDGE2D-EIRENE version is $edge2d\_v240815\_Li$ and is provided by Derek Harting

[3]The data are provided by Matteo Iafrati.

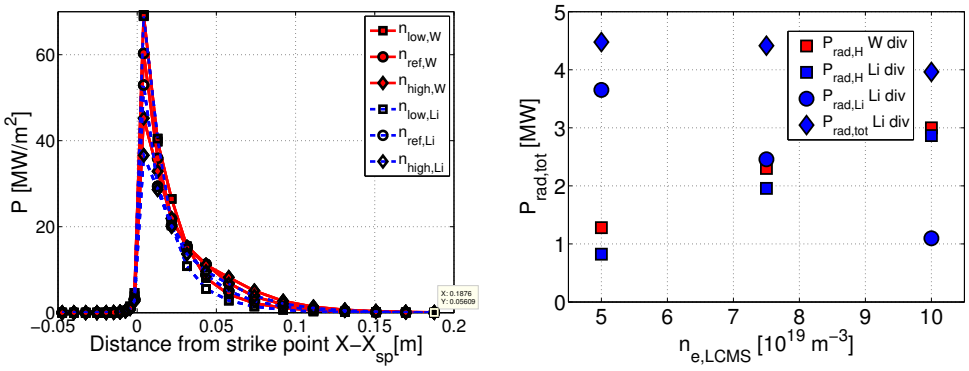

(a) (b)

Figure 3.26: (a)Power density profiles onto the outer target as a function of the distance from strike point for the low (squares), reference (circles) and high (diamonds) density scenarios. Solid symbols refers to W plates while open symbols to Li divertor. (b) Evolution of the radiated power by deuterium atoms (red and blue squares for W and Li), Li impurity (blue circles). In case of Li divertor, the total radiation is also shown with blue diamonds The input power for the simulations is set to $P_{sep} = 37MW$.

preliminary analysis we shows the results of regimes dominated by the sputtering, that is for low values of the wall temperature. A possible approach to simulate the the evaporation stems in an artificial puffing of Li atoms from the divertor region. However, this procedure leads to incorrect results since the increase in the local and total radiation is negligible even in case of strong external Li puffs. The reason for this discrepancy in the code is still under investigation.

Results

In order to evaluate the effect of change of the divertor material, the three different density scenarios are taken into account. The analysis is performed in terms of heat power fluxes and focuses on the outer divertor target. Figure 3.26a shows the three power profiles onto the outer target for the three density scenarios for the standard W (red) and Li (blue) divertor cases. We can clearly see that no major difference are present. In particular, for the low density scenario the two curves overlap and no reduction in the peak power is observed. Increasing the upstream density a slight reduction of the power peak is observed corresponding to $\Delta P_{peak,ref} = 7.4MW/m^2$ (12%) and $\Delta P_{peak,high} = 8.6MW/m^2$ (19%) for the reference and high density scenario, respectively. The reduction is primarily due to the Li radiation.

As can be seen in figure 3.26b, the total power radiated by Li (blue circles) is a

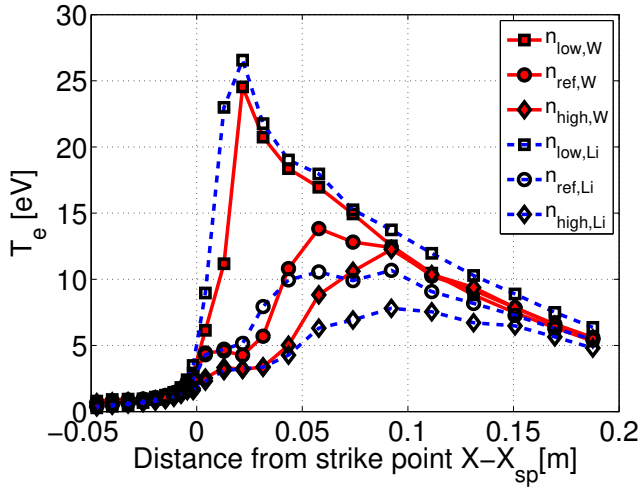

Figure 3.27: Electron temperature profiles on the outer target as a function of the distance from strike point for the low (squares), reference (circles) and high (diamonds) density scenarios. Solid symbols refers to W plates while open symbols to Li divertor. The input power for the simulations is set to $P_{sep} = 37MW$.

decreasing function of the upstream density (reduction by $P_{rad,Li} = 3.65$ to $1.1MW$ from low to high density scenarios), while the total radiation increases driven by the raise in the Hydrogen deuterium radiation. This results is consistent with the electron temperature at the outer target, shown in figure 3.27. As shown in the previous section, higher the upstream density, lower the target electron temperature. This is due to the change of the SOL conditions that yields to high parallel temperature gradients. Firstly, for $n_{e,LCMS} = 1.0 \times 10^{20} m^{-3}$ the electron temperature falls below $10eV$ all along the target. By observing figure 1.8 where the radiative power L_z in coronal equilibrium are given as a function of the electron temperature, we see a drastic reduction in the L_z for $T_e \sim 10eV$. Therefore, the decrease in T_e directly affect the power radiated by Li.

Most importantly, the decrease in temperature has another consequence. Since we only consider the sputtering of Li from the wall, the decrease in T_e reflects in a reduction of the Li atoms extracted from the surface. This behaviour is clearly visible in figure 3.28 where the contour plots of both distribution of the Li radiation and total impurity density are depicted. First of all, we can see a strong reduction of the Li content, especially near the separatrix. This behaviour is a consequence of the strong decrease in the electron temperature in the proximity of the strike point (for $n_{e,LCMS}$ falls below $T_e = 5eV$) since the impinging ions are less effective in extracting Li atoms. As a results a strong decrease in the radiated power is observed in the near SOL, especially in the X-point region. In addition, since the main difference in the Li radiation distribution between the low and high density scenario are located

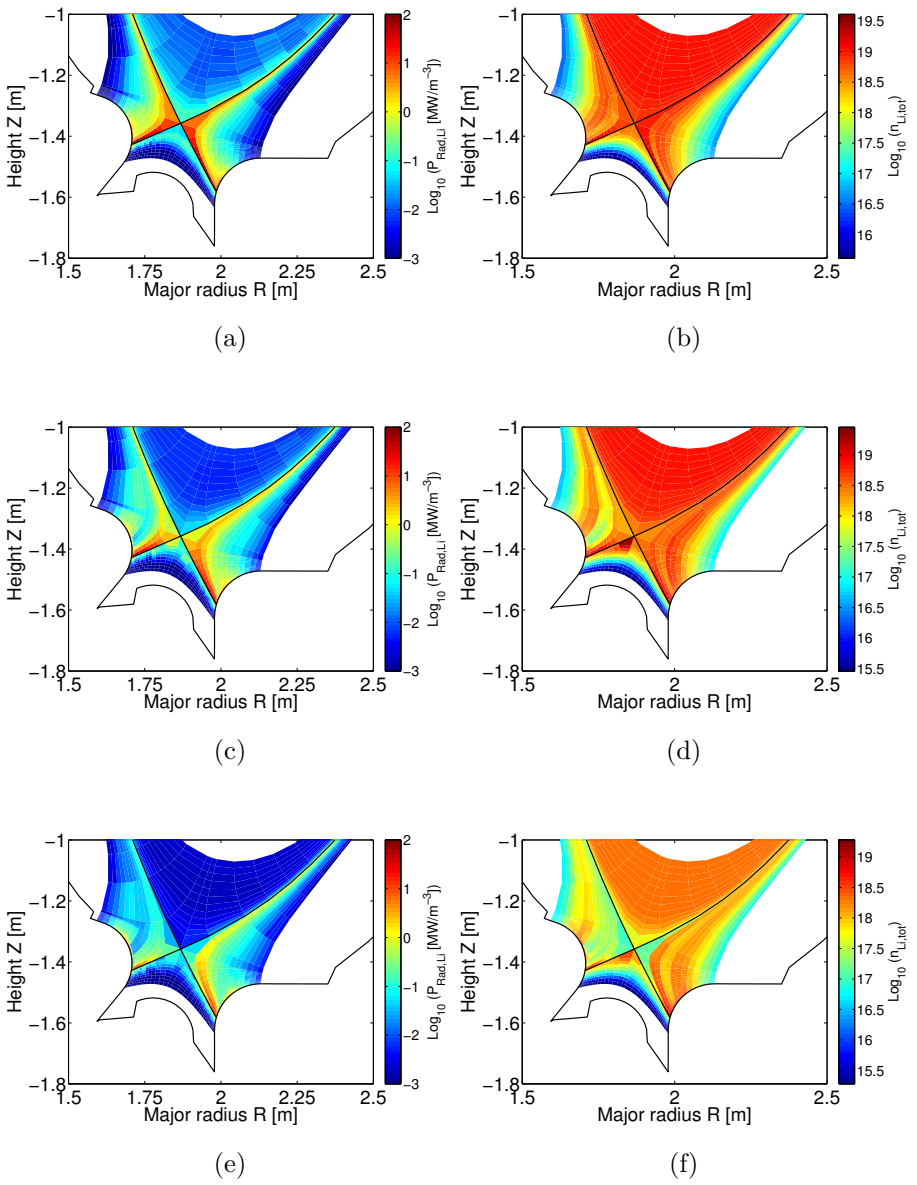

Figure 3.28: 2D contour maps of the (a), (c),(e) Li radiation distribution and of the (b), (d), (f)total impurity density in the divertor region plotted in log scale in the Li divertor case. From the top to the bottom, the results refer to low, reference and high density scenarios. The input power is set to $P_{sep} = 37MW$.

inside the first SOL ring, the main driver for the reduction $P_{rad,Li}$ is related to the drop in the Li sputtering. In addition, it is interesting to remark that the Li concentration inside the core region is quite high; for instance, by considering the

reference scenario, we get a lithium concentration of $c_{Li} = n_{Li}/n_e = 7.8\%$ which reflects in a reduction of P_{fus} by $\approx 40\%$.

In conclusion, the presence of a Li wall in regimes dominated by sputtering are not effective in mitigating the power loads on the divertor plate. Furthermore, this feature is further stressed for high upstream densities, where the decrease in the target electron temperature results in a reduction of the radiation by Li primarily driven by the reduction in the Li sputtering. However, it is important to remark that a liquid surface is able to withstand higher thermal load than a solid one, as experimentally seen in the linear device Magnum-PSI where a steady state power load up to $12.5 MW/m^2$ has been achieved (but it could be higher) [58]. In addition, the strong Li evaporation corresponding to an increase in the surface temperature should be taken into account since it could give rise to the vapor shield effect with beneficial effect on target damage prevention. Therefore, in order to perform an accurate analysis, high evaporation regimes should be included such that possible high radiated power levels and strong reductions of power peaks can be correctly studied and numerically reproduced.

Chapter 4

SOLEDGE2D-EIRENE modelling

The use of advanced magnetic divertor configurations can represent a possible solution to alleviate the power exhaust issue foressen in future tokamak machine as DEMO. The study of the SOL plasma behaviour and of possible mechanisms originating by the change in the magnetic topology is performed by means of 2D edge code and is essential to make prediction on the real advantages related to these solutions.

However, the most used and validated codes currently available in the fusion community, as EDGE2D-EIRENE and SOLPS, are not able to deal with these configurations since of the presence of a second null point within the mesh domain, as shown in the previous chapter. Therefore, the use of different numerical tools is necessary. One of the recently developed codes is SOLEDGE2D-EIRENE (section 2.3.3). In this chapter we present a SOLEDGE2D-EIRENE validation analysis performed by comparing the numerical results with the experimental data of the JET M15-20 experiment on the effect of the flux expansion on the radiative divertor performance.

The SN reference equilibrium and the unseeded plasma discharge JPN 91986 are considered since the main goal is the assessment of the SOLEDGE2D-EIRENE reliability. The numerical results are compared to the experimental data in terms of upstream and downstream profiles. Finally, the analysis involves the radiation distribution reconstruction obtained from bolometry data. It is important to point out that the main aim of this work is not yet fully achieved and that we here present only preliminary results describing the state of the art.

4.1 Description of M15-20 experiment

The high radiative divertor scenarios obtained with the injection of low-Z impurities are mandatory for safe operations in future burning plasma machines. Several studies has been conducted during the years for the evaluation of the effect of the

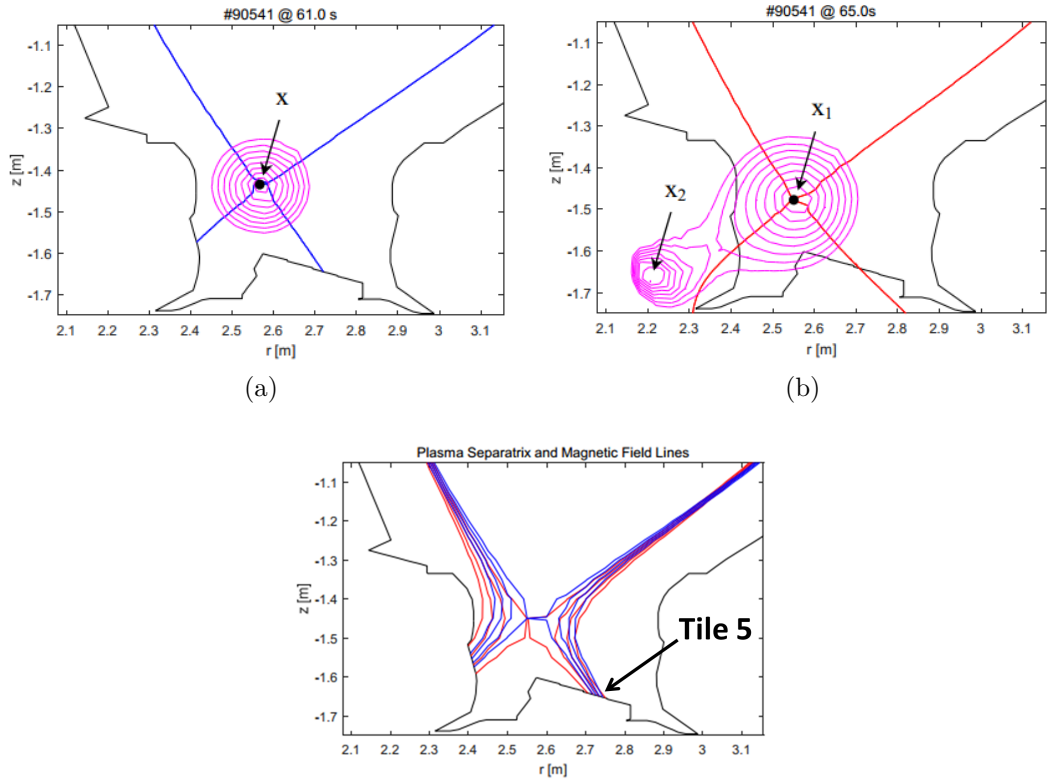

Figure 4.1: Isocontour lines (magenta) of the poloidal magnetic field for the (a) reference and (b) two nearby nulls magnetic configurations. The X-points are also indicated. (c) Flux surface for the reference (blue line) and two nearby nulls configuration showing the change in the FE. The plots refers to the JET-ILW experimental discharge JPN #90541 at $t = 61s$ (reference) and $t = 65s$ (HFE) [63].

divertor geometry on radiatve divertor performance on different machines, as described for example in [59], [60], [61], [62]. Here we focus on the set of experiment performed in the M15-20 experimental campaign on the assessment of the effect of a change of the flux expansion (FE) on the radiative divertor performance and on the radiation peak in the X-point region.

4.1.1 High flux expansion plasmas

In this work we refers to the semi horizontal configurations, that is when the strike point is located on the main load bearing tile (tile5), in JET equipped with ITER like Wall (JET-ILW). The main parameters of the high triangularity shaped nitrogen seeded H-mode plasma are given by $B_{tor} = 2.15T$, $I_p = 2MA$ and $q_{95} = 3.35$ [64]. A configuration with High Flux Expansions has been obtained by means of two

nearby poloidal field nulls, as described in [63]. Figures 4.1 shows the two magnetic poloidal field obtained in an initial ohmic discharges of the HFE experiments with $I_p = 1.8MA$ for the reference (low flux expansion, LFE) and two nearby nulls (high flux expansion, HFE) divertor configurations. While the reference scenario is a standard SN (the X-point is indicated in figure with **X**), in the HFE case there is the presence of a second null of B_p (indicated as $\mathbf{X_2}$) located in the HFS outside the vessel wall. The second null point creates a 'flatness' of the poloidal field as can be observed with the magenta isolines of B_p; in turn, this yields to a flaring of the flux surfaces that can be directly translated in an increase in the flux expansion. Different from the defintion in eq. 1.9, in [63] the flux expansion on the inner/outer target is the distance between the strike point of the SOL boundary and of separatrix evaluated along the target tile, while the flux expansion at the primary X-point is the expansion of the flux tube on the horizontal plane.

As reported in [63], an increase in FE by $\sim 20\%$ and by 50% is respectively obtained at the primary X-point outwards and at the outer divertor target by changing the magnetic topology. This feature is visible in figure 4.1c where the flux surfaces for LFE (blue lines) and HFE (red lines) are depicted. The flaring of the flux surface is clearly visible.

In order to assess the effect of the flux expansion on the radiative divertor performance a preliminary predictive study has been conducted by B. Viola et al. in [65] by considering both unseeded and nitrogen seeded JET-ILW H-mode plasmas by means of EDGE2D-EIRENE code. In this work, three different magnetic equilibria have been taken into account: a reference LFE and two different HFE equilibria, i.e. HFE1 and HFE2 which differ in the the inner target to X-point distance. The results in [65] shows that in the unseeded plasma there is an increase by $\sim 15\%$ in the total radiated power and by 50% in the X-point radiation in HFEs with respect to LFE case. This enhancement is related to the atomic and molecular processes and charge exchange. In the nitrogen seeded plasma a reduction by $\sim 20\%$ of the nitrogen content is observed to reach the same level of required radiation in HFEs than in LFE. In additon, by fixing the nitrogen seeding an increase by 40% and 30% in the total radiated power is observed for HFE1 and HFE2, respectively, with respect to LFE.

Moreover, these predicted results have been compared to the experimental data in [64], showing that the bolometry data are quite matched in case of nitrogen seeding, while the code is not able to reproduce unseeded discharges.

4.1.2 Diagnostics

The diagnostics used in the validation phase are a shown in figure 4.2 and are given by:

- the high resolution Thomson scattering (HTRS) shown with the blue line in

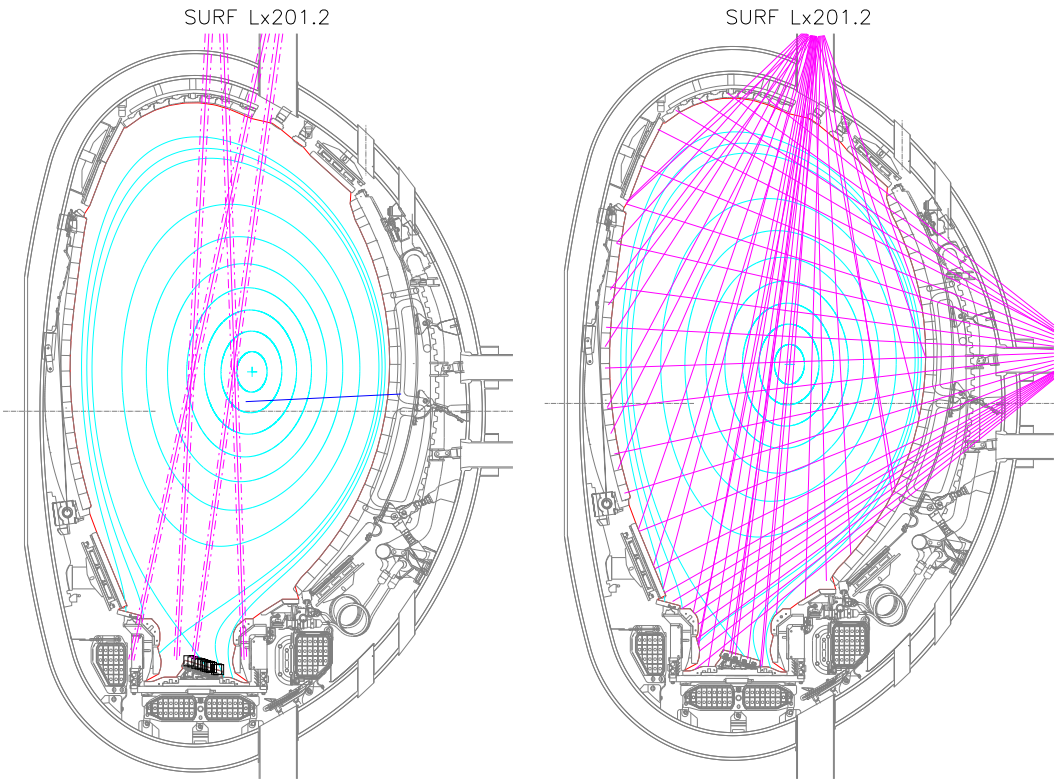

(a) (b)

Figure 4.2: (a) Visible spectroscopy, tile 5 Langmuir probes and HTRS diagnostics are shown in magenta, blue and black, respectively. (b) Lines of sight of the bolometry are shown in magenta. The diagnostics are superimposed to the equilibrium reconstruction (cyan lines) of the JPN 91986 at $t = 50s$.

figure 4.2a. It is used to measure the electron temperature and density on the outer mid plane. The signal is sampled every $50ms$. Due to the uncertainty in the actual position of the separatrix obtained with the equilibrium reconstruction, a deconvolution of the HTRS data is performed[1] [66] by using a *mtanh* function [67]. The position of the separatrix is then chosen accordingly with the 2PM and also compared with the data obtained from XLOC code [2] [68];

- Langmuir probes on the outer target shown with black squares in figure 4.2a. This diagnostic is used to evaluate the electron density and temperature on the target plates, other than to measure the saturation current and to extract the power loads profiles;

[1]The convoluted data are provided by L. Frassinetti.

[2]The data are provided by G. Artaserse.

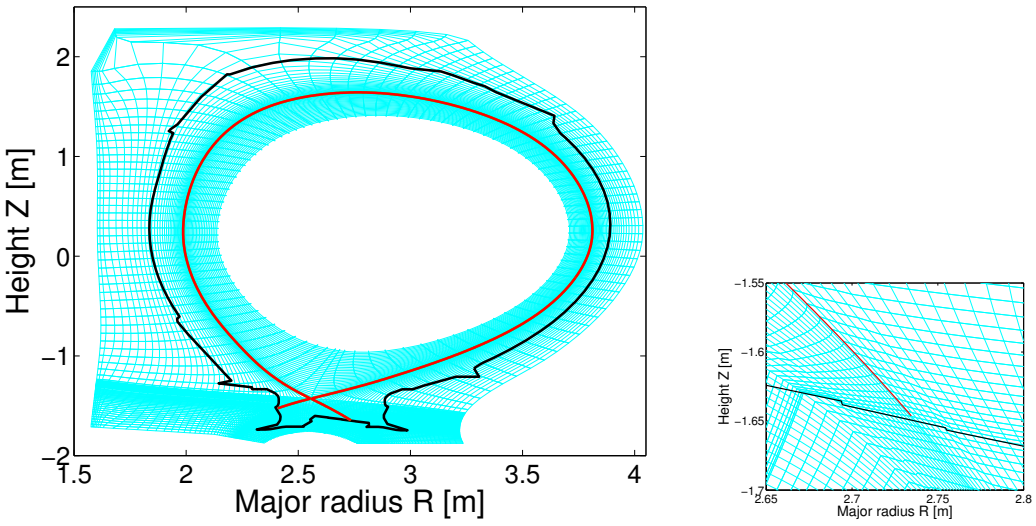

(a) (b)

Figure 4.3: (a) Mesh generated (cyan) from the EFIT equilibrium reconstruction for the SOLEDGE2D computation. The mesh extends into the SOL wall.(b) Magnification of the mesh in the outer target region showing the alignment of the cell with the target plate. The separatrix and the vessel walls are shown in red and black, respectively.

- Visible spectroscopy on the inner and outer target shown in magenta in figure 4.2a and in particular the EDG8 signal. It collect particular lines of sight (LOS) of the KS3 spectroscopy and it is used to measure particular line emission;

- Bolometry shown in magenta in figure 4.2b. This diagnostic measures the radiation on the different LOS viewing the plasma both vertically and horizontally. From the bolometric signal is also possible to derive the radiation distribution on the poloidal plane (tomographic reconstruction[3]).

4.2 SOLEDGE2D-EIRENE inputs

4.2.1 Grid

The mesh for the SOLEDGE2D computation is shown in figure 4.3a. The mesh is field aligned and is obtained from the equilibrium reconstruction of the JET pulse

[3]The tomographic reconstruction are provided by A.Huber.

#91986 at $t = 50s$ by means of the EFIT code[4]. As discussed in section 2.3.3, the peculiarity of the SOLEDGE2D mesh is to extend into the wall, as can be clearly seen in figure. This feature allows for a more accurate evaluation of the effect of the first wall on the SOL plasma behaviour. The region outside the vessel wall are treated numerically by means of a penalization technique, that is by imposing a penalization terms in the fluid equations. The JET-ILW is simulated by imposing a W wall in the divertor region, while the main chamber is set to Be.

Additionally, the magnification in the outer target region is given in figure 4.3b. An alignment of the cell is performed on the target plate in the neighbour of the strike point. This characteristic gives more stability to the code since it helps to reduce errors due to penalization interpolations of fluxes on the wall.

Finally, it is worth noting that the grid resolution is much higher than the ones previously shown. However, a different numerical scheme is adopted to solve the fluid equations; moreover, there is the possibility to split the computational domain, thus performing a parallelization of the fluid calculations. These two features reflects in a computational time comparable, and even shorter, than the one required by the EDGE2D-EIRENE code.

4.2.2 Power and puffing

Once defined the computational mesh we can evaluate the power to set as input in the simulations. This value is applied as a boundary condition on the innermost flux surface on the core side. It comes from a balance of the total heat power supplied to the plasma minus the core radiation inside the confined region and the change of the diamagnetic current $\dot{W}_{dia}$. In formulae:

$$P_{in} = P_{NBI} + P_{OHM} - P_{rad,core} - \dot{W}_{dia}. \tag{4.1}$$

It is important to remark that the term $\dot{W}_{dia}$ is related to the energy stored in the pedestal region between two ELM events. Therefore, this energy term does not contribute to the energy crossing the separatrix during the inter-ELM phase and has to be subtracted from the global power balance. Following the procedure described in [40], we get $\dot{W}_{dia} = 3.5MW$.

Figure 4.4 shows the time traces of the various term to consider in the power balance for the input power calculation. The $t = 50s$ used for the equilibrium reconstruction is also shown. These data are obtained by the post processed data system EFIT DDA for the NBI (red) and Ohmic (blue) power, while for the bulk radiation (TOBH) we use the BOLO DDA, which is based on a selection of the horizontal bolometer LOS. By considering the different terms we get an input power

[4]The equilibrium reconstruction is provided by I. Lupelli.

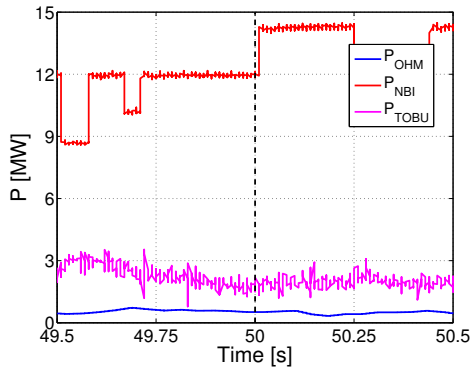

Figure 4.4: Time traces of the NBI and Ohmic power read from the EFIT DDA are shown in red and blue, respectively. The total bulk radiation obtained from the post processed bolometry data is shown in magenta. The vertical black dotted line indicates the $t = 50s$ used for the equilibrium reconstruction.

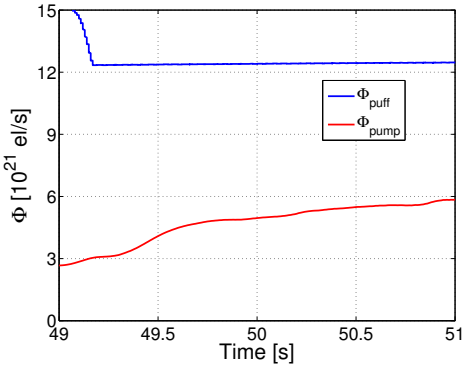

Figure 4.5: Time traces of the puffing rate (blue line) and of the pumped flux of deuterium in the JPN #91986.

for the simulation of $P_{in} = 8MW$. This value is equally split between ions and electron (4 MW each).

As far as the particle deuterium fluxes are concerned, the puffing rate is posed equal to the experimental one $\Phi_{puff} = 1.25 \times 10^{22} el/s$ (blue line in figure 4.5). This value is obtained by the post processed data read by the GASM DDA. Finally, the pumped flux, shown in red figure 4.5, can be evaluated by following formula[40]:

$$\Phi_{pump}(el/s) = 2n_{neut}S(\frac{m^3}{s}), \tag{4.2}$$

where the neutral density n_{neut} is obtained by the measure of the Penning Gauge of $p_{neut,subdiv}$ in the sub-divertor region and by considering the ideal gas equation $p = k_b nT$. The temperature in the sub-divertor region is posed equal to $T = 300K$.

S is the pumping speed posed equal to $S = 100m^3/s$. In the numerical simulation the pumped flux is calculated by the code by considering an albedo $\alpha = 0.95$. In addition, we can observe a difference in the puffed and pumped flux, which can results from possible outgassing from the wall. From the computational point of view, we can consider a Recycling coefficient on the main chamber $R_c^{mc} < 1$. Hereafter, the effect of a change in the recycling coefficient is investigated.

Finally, in the simulation we cansider also the presence of Be defined as an intrisic impurity, while the W impurity is neglected. The physical sputtering of Be, which represent the source, can be imposed in SOLEDGE2D-EIRENE in different way, in particular we use the Bohdansky sputtering model (see [28] and reference therein).

4.3 Comparison with experimental data

Once described the main features and the main inputs for the numerical simulations, we can compare the numerical results with the experimental data of the inter-ELM phase of the JPN #91986 at $t = 50s$.

4.3.1 Upstream profiles

The first step in the analysis is the comparison of the upstream profiles. Since we are simulating an H-mode plasma, we use a couple of diffusion coefficients $D_\perp$, χ which vary with the radial coordinate at the outer midplane in order to simulate the Edge Transport Barrier which set up. The radial profile are adjusted in order to approach the density and electron temperature at the equatorial plane measured by means of the HTRS system. The diffusion coefficient of Be is posed equal to the that of deuterium, while we set $\chi_i = \chi_e$ since of the lack of measurement of the ion temperature. In addition, since the transport barrier should not extend below the the X-point, the transport coefficients in the inner and outer divertor chamber are set constant and equal to $D_\perp = 0.64m^2/s$ and $\chi = 1m^2/s$, as made in [65].

Initially, the same transport coefficient profiles as in [65] are used in the simulations. However, we get a high value of the electron temperature at the separatrix, which in turn reflects on target quantities. The different behaviour observed in the two numerical tools, i.e. EDGE2D-EIRENE and SOLEDGE2D-EIRENE, is probably related to the different energy equations solved by the two codes. More specifically, while EDGE2D-EIRENE solves the equations for internal energy, in SOLEDGE2D-EIRENE the total energy equation is considered.

As a consequence, a redefinition of the transport coefficients profiles is necessary in order to approach the n_e and T_e experimental profiles. In figure 4.6 the profiles of $D_{\perp,1}$ and $\chi_{i,e,1}$ are shown in blue and red, respectively. We can observe a sharp increase of the energy diffusion coefficient just outside the separatrix. This choice is

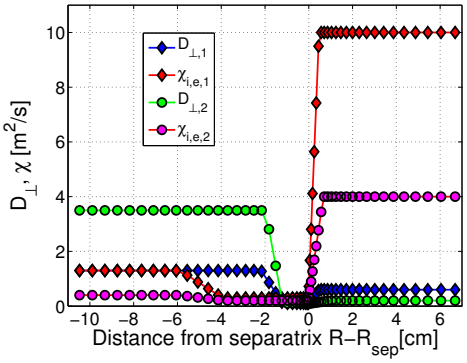

Figure 4.6: Radial profiles of $D_\perp$ and χ as a function of the distance from the separatrix used for the simulation of the JPN #91986 by means of SOLEDGE2D-EIRENE. The two sets of diffusion coefficients are shown with diamonds (blue and red for $D_{\perp,1}$ and χ_1, respectively) and circles (green and magenta for $D_{\perp,2}$ and χ_2, respectively).

motivated by the need to decrease the separatrix temperature to a reasonable value. In the simulation we get $T_{e,LCMS} = 73.8eV$.

Following this procedure, we compare the obtained profiles with the experimental data. As previously stated, there is an uncertainty on the exact position of the separatrix obtained with the EFIT reconstruction (the expected error in the separatrix postion is $\sim 2cm$). Therefore, accordingly with [64], the experimental data obtained with the HTRS system are shifted by $\sim 2.8cm$ outward in order to have a separatrix electron temperature consistent with the 2PM. This shift is evaluated by considering the electron temperature profiles fit with the *mtanh* function. This value is then compared to the shift obtained with the ROG (radial outer gap) value given by the XLOC code. The two values are consistent since with the XLOC data we get a a shift of $\sim 2.5cm$.

Figure 4.7 shows in blue the density and temperature profiles obtained in the simulations by using the set of diffusion coefficient previously described. The experimental data obtained with the HTRS system are shown in red with the error bar. We can see a good match of the upstream density profile, especially in the pedestal region, while the temperature profiles is quite high and out of the error band. However, for both density and temperature a more flat profile is obtained in the SOL since of the high diffusion coefficients setups. This behaviuor is clearly visible by computing the fall-off length, which is given by $\lambda_q > 1cm$. This condition clearly affect the downstream profiles, as we are going to discuss in the next section. In addition, the separatrix density is underestimated. In particular, a value of $n_{e,LCMS} = 2.3 \times 10^{19} m^{-3}$ is obtained, while the density estimated with the deconvoluted data is $n_{e,LCMS} = 3.4 \times 10^{19} m^{-3}$.

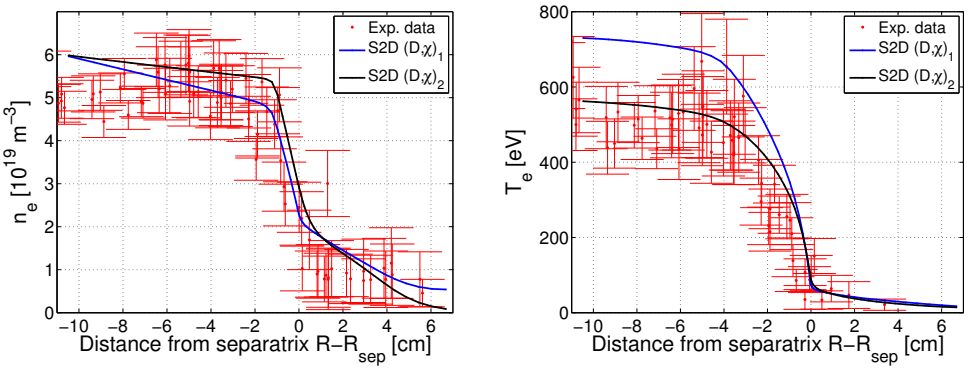

(a) (b)

Figure 4.7: (a) Upstream density and (b) temperature profiles obtained in the simulations with $D_{\perp,1}, \chi_1$ are shown in blue while the experimental data are shown with red points with the error bar. The profiles obtained with $D_{\perp,2}, \chi_2$ are shown in black.

It is therefore necessary to redefine the transport coefficient in order to decrease the decay length and to approach the experimental profiles. However, this optimization procedure is still on going and we report only preliminary results obtained in the calculations. The new radial profiles of $D_{\perp,2}, \chi_2$ are shown in figure 4.6 in green and magenta, respectively, and the upstream electron density and temperature profiles are shown in figure 4.7 with black lines. As we can see, a better match with the experimental data is obtained, especially in terms of temperature profiles. The separatrix density is given by $T_{e,LCMS} = 88.4eV$ compared to $T_{e,LCMS,exp} = 88.2eV$.

As far as the electron density is concerned, the separatrix density is still underestimated ($n_{e,LMCS} = 3.0 \times 10^{19} m^{-3}$), while a good match for the pedestal and core region is obtained. The results in terms of λ_q are closer than the previous one and are give by $\lambda_{q,S2D} = 4.5mm$ and $\lambda_{q,exp} = 3.3mm$ for the numerical computation and the one derived from the experimental data, respectively.

4.3.2 Outer target profiles

Once evaluated the upstream conditions we can proceed by considering the target quantities. The experimental data are obtained by a set of Langmuir Probes (LP) located along the Tile 5. However, a post processing of the signal is necessary since of the presence of the ELMs. In particular, the row data are characterized by a high noise and a ELM filtering procedure is applied. The filtering is based on the signal of total emission by Be^{2+} in the outer divertor region 'TBEO' read by means of the the EDGE8 DDA.

An example of the temporal evolution of the total photon flux by Be^{2+} in the

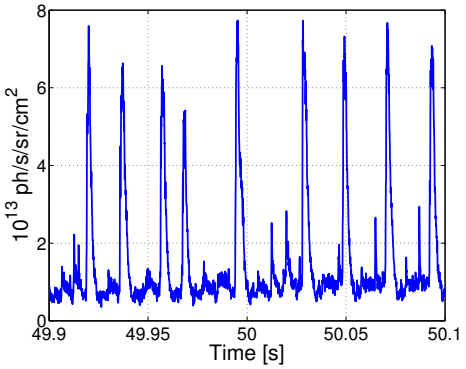

Figure 4.8: Time trace of the total photon emission in the outer divertor in the JPN #91986 around $t = 50s$. The signal is used as a marker for the ELM.

outer divertor, expressed in $ph/cm^2sr\ s$, is shown in figure 4.8. In case of an ELM event, this signal shows the presence of spikes. Therefore, the LP data are filtered by applying a suitable threshold and by considering only the signals in the inter-ELM phase.

In addition, since of the uncertainty on the strike point position, a shift is also applied to the post processed Langmuir data (read by means of the KY4D DDA). The strike point position is evaluated by means of the coordinate given by the XLOC code. Eventually, the data are shifted by $\sim 1.9cm$ towards the SOL.

Figure 4.9 shows the profiles of the electron density (4.9a), electron temperature (4.9b) and power density (4.9c) obtained in the simulations with the two different set of diffusion coefficients (blue and black line for D_1, χ_1 and D_2, χ_2). The post processed experimental data obtained with the signal of the Langmuir probes are shown with red dots. In the simulations with the set of diffusion coefficients $(D, \chi)_1$ shown in figure 4.6 a good match of the electron density is obtained, except in the far SOL region where there is an increase that is not observed in the experiment. This behaviour is related to a high the neutral pressure in the right corner. On the contrary, both temperature and power profiles are not recovered in the simulation. This effect is a result of the high value of χ that is set in the SOL region.

By observing the black line, we see that by redefining the transport coefficient $(D, \chi)_2$ in order to approach the upstream conditions, the electron density is strongly underestimated, while the temperature shows a high peak as a result of the pressure conservation along the flux tube. Indeed, a temperature peak higher than $T_{e,OT} > 10eV$ is observed on the target plates in the experiment which results in a well attached plasma regime. The reason for the density drop is not yet understood and the work is still on going. On the other hand, since of the lower value of λ_q obtained in this case, the power profile is closer to the experimental data than the one previously obtained.

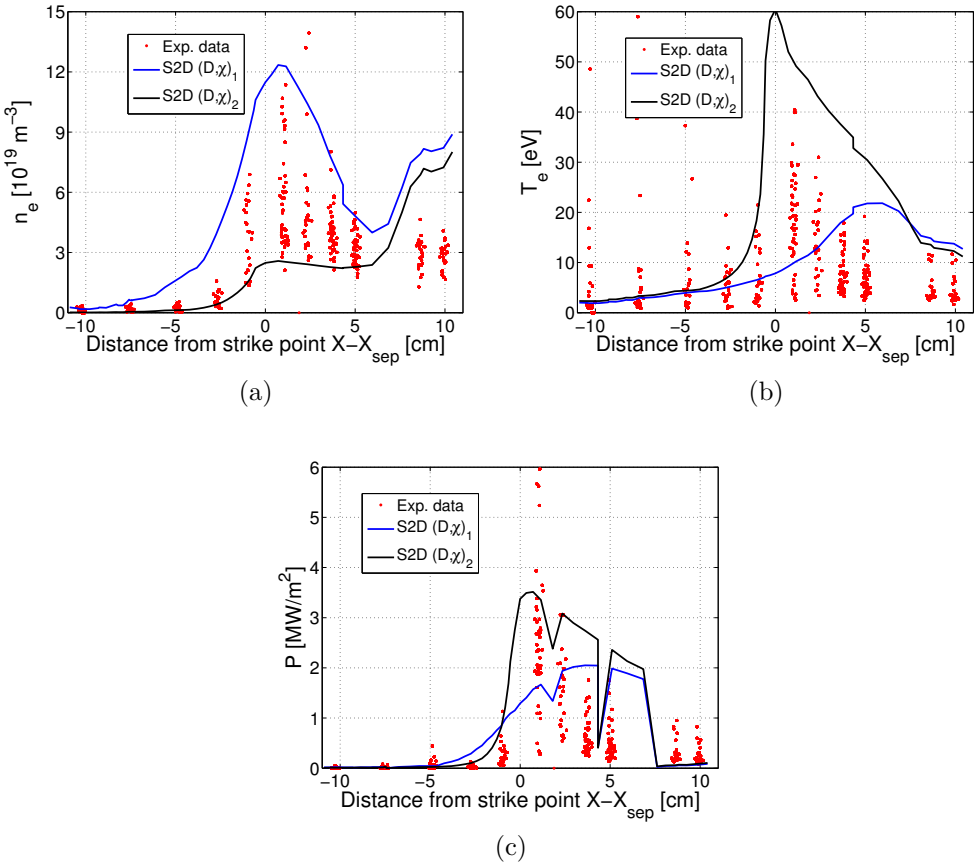

Figure 4.9: (a) Target electron density, (b) electron temperature and (c) power flux density profiles obtained in the simulation with $D_{\perp,1}, \chi_1$ are shown in blue while the experimental data of the JPN #91986 are shown with red dots and are shifted towards the SOL by $\sim 1.9cm$. The profiles obtained with the set of diffusion coefficients $D_{\perp,2}, \chi_2$ are shown in black.

Furthermore, it is interesting to note that the sharp decreases in the power profiles are merely related to the detailed shape of the vessel used in the computational grid. In particular, these drops are located in the discontinuity of the vessel, where the target abruptly change inclination.

Summarizing, we can state that a definition of the diffusion coefficient that allows a better match of the upstream profiles is necessary to recover the downstream conditions. However, this is a long and time requiring procedure and the best couple of coefficients is not yet achieved.

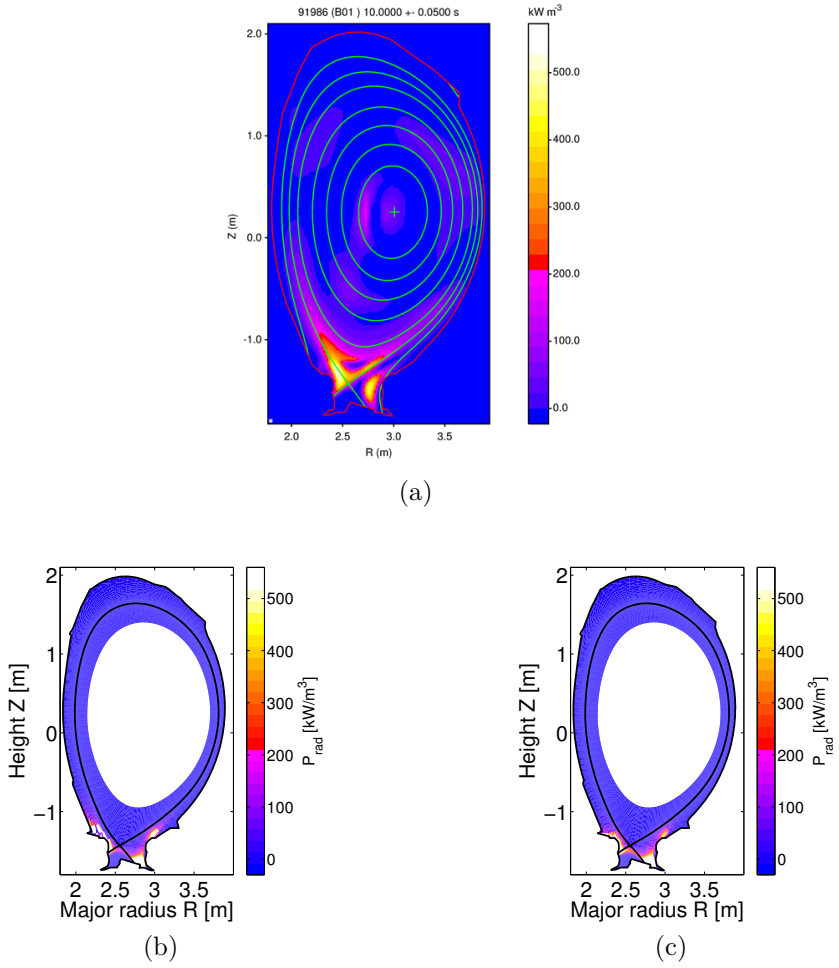

(a)

(b)

(c)

Figure 4.10: (a) Tomographic reconstruction of the 2D radiation density for the JPN #91986 at $t = 50s$[A. Huber]. Contour plot of the 2D radiation distribution obtained in SOLEDGE2D-EIRENE calcuation by setting (b) $R_c^{mc} = 1$ and (c) $R_c^{mc} = 0.6$.

4.3.3 Radiation

The last point in the analysis focuses on the 2D radiation distribution. Here, we refer to the set of diffusion coefficient labeled $D_{\perp,2}, \chi_2$ since they gives the best results in terms of upstream profiles. The radiation obtained in the calculation are then compared with the tomographic reconstruction obtained from the bolometry data.

Figure 4.10a shows the experimental 2D radiation distribution reconstruction of the JPN #91986. The total radiation is mainly localized in the inner divertor chamber and also extend near the separatrix above the X-point position. A high radiated region is also observed in the outer divertor chamber.

By comparing the 2D radiation density obtained in the numerical simulations,

setting a recycling coefficient on the main chamber $R_c^{mc} = 1$, we see that the radiation in the inner divertor region is partially recovered even if it is located in front of target and does not extend up to the separatrix. On the other hand, discrepancies between experimental and numerical data are observed in the LFS since in SOLEDGE2D-EIRENE simulations the radiation zone is located on tile 5. Furthermore, a high radiating zone above the HFS baffle and that extend in the main SOL is predicted by the code, while it is not observed experimentally.

In order to evaluate the nature of the latter radiation peaking region, the total radiation is broken down in the different contributions related to the deuterium and Be ions emission. In addition, a cross check of the total radiation in performed. For the experimental data we refers to the total radiation in the divertor and X-point region. By comparing the total radiated power we see an overestimation by a factor ~ 2 in the numerical simulations, where the deuterium contribution is $\sim 65\%$.

In order to approach the same level of the total radiated power a sensitivity analysis on the recycling coefficient of the deuterium on the main chamber is performed, while keeping $R_c^{div} = 1$ on tungsten. This choice is also motivated by the different experimental values of the pumped and puffed fluxes, as shown in figure 4.5.

The results of the simulations with $R_c^{mc} = 0.6$ is shown in figure 4.10c. We can see a slight improvement of the results with respect to the previous one with $R_c^{mc} = 1$ since the extension of the radiation distribution in the SOL region above the HFS baffle is reduced. However, the peaking of the radiation on tile 5 in the outer divertor chamber is still observed. In addition, by considering the different terms of the radiation distribution for the deuterium and Be ions, we observe that the radiation peaking region on the HFS baffle is primarily related to Be^{1+}, in accordance with the co-deposition and outgassing of Be during ELM observed in JET-ILW [69]. Therefore, the next step in the analysis is to evaluate the change in the recycling coefficient for Be, since we are simulating an inter ELM phase.

As a final remark, the conclusion is that even though a match of the plasma divertor conditions is not fully obtained in terms of electron density and temperature, the code is able to fairly recover the results in terms of power loads. However, it should be pointed out that a precise definition of the diffusion coefficient is not yet achieved. In addition, the analysis of the radiation distribution also shows that the effect of the main chamber wall on the SOL behaviour can be directly studied since of the features of the computational grid. Therefore, the results of the preliminary validation phase show that SOLEDGE2D-EIRENE can represent a promising numerical tool for the study of the edge plasma, especially in view of advanced magnetic divertor geometry which can not be handled by other 2D edge codes.

Chapter 5

Conclusions

The power exhaust is recognized as one of the major challenges in a future fusion reactor as DEMO. The current proposed solution is based on the ITER highly radiative baseline scenario which foresees the use of a standard single null (SN) divertor with tungsten divertor plates[48], [49]. However, in order to mitigate the risk that this conventional scenario should not extrapolate from ITER to DEMO the EUROfusion consortium is currently assessing alternative solutions.

Two different approaches can be adopted in order to reduce the heat loads on the divertor plates. On one hand, a change of the magnetic divertor configuration leads to a higher flux expansion than in the standard SN, which in turns reflects on a spreading of the power on larger surfaces. This feature is related to the presence of a second null point of the poloidal magnetic field and these configurations are also referred to as Advanced magnetic configurations (AC). In addition, the change of the topology could result in high radiation fraction in the divertor chamber due to the longer connection length and the increase in the divertor volume. Different configurations has been proposed in the past; among them, the X divertor (XD)[18], Super-X divertor (SXD) [19]and the Snowflake divertor (SFD) [20] have been considered as promising divertor improvement of the conventional one.

On the other hand, the heat power issue can be tackled by changing the properties of the target materials, i.e. by adopting liquid metal divertors. Nowadays, the most promising solution is based on stationary fluids confined in a porous system which ensure the stability of the liquid metal in a strong magnetic field[56], [57]. The liquid surface is able to withstand higher power fluxes than the conventional solution. Most importantly, a self-healing process, the so-called '*vapour shield*' [25], could set up since the increase in the heat flux reflect in an increase of the evaporation rate and, in turn, of the radiated power fraction.

The numerical modelling represent an essential ingredient in order to assess the beneficial effects that could originate from the different alternative solutions to take into account. The Ph.D. research activity presented in this thesis is focused on the analysis of the Scrape off layer plasma and the divertor region by means of 2D

edge codes. In particular, this work focuses on the study of alternative divertor configurations and is carried out in the framework of the two EUROfusion Work Packages WPDTT1 and WPDTT2.

Initially, a possible DEMO scenario is simulated with EDGE2D-EIRENE [33], [38] by considering a set of relevant parameters that define the so-called '*baseline scenario*' which foresees the use of a conventional SN divertor configuration with W plates [49]. Two main assumptions are used. The first one involves the use of perpendicular targets on both the inner and outer target, even though in the considered scenario both the strike points are located on vertical target plates. The second one concerns the pure Deuterium assumption in order to speed up the simulations. In order to study the general features of the considered scenario and to identify the possible SOL plasma regimes, two different scans are performed by changing the transport coefficients and the upstream density. By analysing both the upstream collisionality and the target conditions, we see that the code predicts a plasma in sheath limited regime in the overall density scan. In addition, this result is further confirmed by the minor role played by the volumetric losses, by the predicted trends of the maximum density and of the ion flux on the outer target against the upstream density and by the trend of the power peak against the upstream power decay length ($P_{peak,OT} \propto \lambda_q^{-1}$).

The obtained results shows that both electron temperature and power peaks are totally unacceptable from an operational point of view since $T_{e,OT} > 50eV$ and $P_{peak,OT} > 30MW/m^2$ even considering the target tilting in the poloidal plane. This results highlights the criticality of DEMO and confirms that external impurities injections are mandatory for safe operation and to reach high radiation fraction in the SOL ($P_{rad} > 80\%P_{sep}$). However, these results could represent a reference for a comparison with other alternative solutions to take into account. A more realistic analysis should consider an impurity seeded plasma and the actual divertor geometry.

Subsequently, a benchmark of TECXY [31] is carried out. This 2D edge code is simpler and faster than EDGE2D-EIRENE. Moreover, differently from the latter, TECXY is also able to deal with the presence of a second null point but it is not able to accurately describe the neutral dynamics and the corresponding effect on the SOL and divertor plasma conditions due to the simple analytical neutrals model. By comparing the results, discrepancies are observed in the profiles of the electron temperature and density on the outer target due to the different physical models used for description of the neutrals. However, a good match of the numerical results of the two codes is obtained in terms of upstream quantities and power loads on the divertor target. The two codes also predict the same trends for the total deposited power and volumetric losses as a function of both upstream density and λ_q. Therefore, we show than in case of well attached plasma conditions TECXY can be reliably used to perform a fast screening of the possible configurations to

take into account in order to identify the main features and the most promising solutions. Additionally, a strong reduction of the computational time is obtained since only few hours are required by TECXY while in case of EDGE2D-EIRENE we spent almost 1 month for a simulation.

Since a facility named Divertor Test Tokamak (DTT) has been proposed to study the power exhaust issue in view of DEMO[10], the second step of this Ph.D. thesis focuses on the study of the alternative magnetic configurations of the DTT machine. First of all, a scoping study is performed by comparing the standard SN reference solution with a Quasi snowflake (QSF)[21] configuration. By analysing the upstream collisionality variation in a density scan, we show that the QSF is more prone to reach the detachment than SN. In particular, while in SN only an incipient detachment state is observed, in QSF a totally detached regime is achieved for the highest value of the density. This results is confirmed by the roll-over of the maximum target density, by the drop of the target electron temperature below $T_e = 5eV$ and by the high deuterium radiation distributed all along the target. Furthermore, the numerical results show that in case of QSF we get manageable value of the power loads on the outer target, while in SN power level higher than the tolerable value are obtained. This different behaviour is related to the change in topology, especially it is due to geometrical factor being the higher flux expansion the main driver for the power spreading. A negligible difference is observed in the radiation level in the two cases for a pure deuterium plasma.

Finally, an analysis of the neutral particle behaviour shows that in case of a detached plasma a better neutral confinement is obtained in QSF with respect to SN. This feature is probably related to the stabilizing effect introduced by the flaring of the flux surfaces in the divertor region since the ionization front is not able to move towards the X-point in case of QSF.

Therefore, the comparison of the two magnetic configurations shows that the QSF can represent a promising solution for the heat power issue in terms of both power loads and achievement and stability of the detachment. In addition, further analysis can take into account the injection of external impurities in order to assess the effect of the connection length on the radiative performance.

A preliminary study of a liquid lithium divertor is also presented but without considering the Li evaporation. However, minor differences are seen with respect to the standard solution with W plates since we simulate a regime dominated by Li sputtering. A more accurate analysis should also take into account the Li evaporation which can give rise to the vapor shield effect.

The last chapter of the thesis deals with the use of a different numerical tool, i.e. SOLEDGE2D-EIRENE[41], [42]. This code is able to treat the ACs; in particular, it is a suitable code for the study of the magnetic configurations characterized by the presence of two nearby nulls as the ones performed in the JET experimental campaign M15-20 for the assessment of the effect of the flux expansion on the radiative

divertor performance [63], [64], [65]. Preliminary results of the validation phase are presented. By comparing the numerical results with the experimental data of JET pulse 91986 we see that while the upstream profiles are fairly matched by the code, the electron temperature and density on the outer target shows large discrepancies. On the contrary, the power density profile is partially reproduced. However, the definition of a suitable couple of transport coefficients able to well reproduce the upstream profiles is still on going. Finally, by comparing the 2D radiation distribution we see that the code is able to partially recover the HFS radiation even though difference are observed in the region above the inner baffle. By redefining the recycling coefficient on the main chamber R_D^{mc} an improvement is obtained. However, the validation phase is still on going and the best set of input parameters able to reproduce the experimental data is not yet obtained.

Nonetheless, this work gives confidence that SOLEDGE2D-EIRENE can represent a reliable numerical tool for the study of the SOL. In addition, by considering the high flexibility and the possibility to treat AC, it can represent a promising tool for the study of the possible alternative solutions able to alleviate the power exhaust issue.

Bibliography

[1] Cabal H. at al., *Analysis of the Potential Contribution of Fusion Power in a Future Low Carbon Global Electricity System*, Energy Strategy Reviews, Vol. 15, p. 1-8, 2017

[2] EFDA. *Fusion Electicity - A roadmap to the realisation of fusion energy 2012*, 2012.

[3] J. Freideberg, *Plasma Physics and Fusion Energy*, Cambridge University Press, 2007.

[4] EUROfusion: Image Gallery. `https://www.euro-fusion.org/2011/09/tokamak-principle-2/?view=gallery-428`.

[5] Wagner, F. et al. , *Regime of Improved Confinement and High Beta in Neutral Beam-Heated Divertor Discharges of the ASDEX Tokamak.* Phys. Rev. Lett., **49**, 1408, 1982.

[6] Zohm, H., *Edge localized modes (ELMs).*, Plasma Phys. Control. Fusion, **38** , 105-128, 1996.

[7] EUROfusion: Image Gallery. `https://www.euro-fusion.org/2011/09/jet/?view=gallery-428`.

[8] EUROfusion: Image Gallery. `https://www.euro-fusion.org/jet/jets-main-features/`.

[9] ITER: Image Gallery. `https://www.iter.org/doc/www/content/com/Lists/WebText_2014/Attachments/230/tkm_cplx_final_plasma2013-07.jpg`.

[10] DTT, Divertor Tokamak Test facility project proposal, ENEA, 2015

[11] EUROfusion: Image Gallery. `https://www.euro-fusion.org/wpcms/wp-content/uploads/2016/03/Divertor_chart.jpg`.

[12] W. Fundamenski, *POWER EXHAUST IN FUSION PLASMAS*, Cambridge University Press, 2010.

[13] T. Eich, et al., *Inter-ELM power decay length for JET and ASDEX Upgrade: measurement and comparison with heuristic drift-based model*, Phys. Rev. Lett. **107**, 215001, 2011.

[14] Y. Shimomura, et al., *Characteristics of the divertor plasma in neutralbeam-heatedASDEX discharges*, Nucl. Fus. **23**, 869, 1983.

[15] P.C. Stangeby and A.W. Leonard, *Obtaining reactor-relevant divertor conditions in tokamaks*. Nucl. Fus. **51**, 063001, 2011.

[16] Y. R. Martin, et al., *3D Power requirement for accessing the H-mode in ITER*, J. Phys.: Conf. Ser., **123**, 012033, 2008.

[17] H. Lux, et al., *Impurity radiation in DEMO systems modelling*,Fusion Eng. Des., **101**, 42-51, 2015.

[18] M. Kotschenreuther, et al., *Magnetic geometry and physics of advanced divertors: The X-divertor and the snowflake*, Phys. plasma, **20**, 102507, 2013

[19] P. M. Valanju, et al. *Super-X divertors and high power density fusion devices*, Phys. plasma, **16**, 056110, 2009.

[20] D. D. Ryutov and V. A.Soukhanovskii, *The snowflake divertor*, Phys. plasma, **22**, 110901, 2015.

[21] G. Calabró, et al., *EAST alternative magnetic configurations: modelling and first experiments*, Nucl. Fus. **55**, 083005, 2015.

[22] S.V. Mirnov, et al., *Liquid-metal tokamak divertors*, J. Nucl. Mater., **196-198**, 45-49, 1992.

[23] R.B. Gomes , et al., *Liquid gallium jet-plasma interaction studies in ISTTOK tokamak*, J. Nucl. Mater., **390-391**, 938-941, 2009.

[24] S. V. Mirnov, et al., *The tests of liquid metals (Ga, Li) as plasma facing components in T-3M and T-11M tokamaks*, Fusion Eng. Des., **81**, 113-119, 2006.

[25] J. W. Coenen, et al., *Liquid metals as alternative solution for the power exhaust of future fusion devices: status and perspective*, Phys. Scr., **T159**, 2014.

[26] G. Mazzitelli, et al., *Experiments on FTU with an actively water cooled liquid lithium limiter*, J. Nucl. Mater., **463**, 1152-1155, 2015.

[27] G. Mazzitelli, et al., *Comparison between liquid lithium and liquid tin limiters in FTU*,44th EPS Conference on Plasma Physics, Belfast, Northern Ireland, 2017.

[28] P. C. Stangeby, *The Plasma Boundary of Magnetic Fusion Devices*, Taylor and Francis Group, 2000.

[29] S. I. Braginskii, *Transport processes in plasma*, Reviews of plasma physycs, volume **1**, pages 205-311. Consultants Bureau, New York, 1965.

[30] R. Fitzpatrick, *PLASMA PHYSICS: An introduction*, CRC Press, 2014.

[31] R. Zagórski, et al., *Numerical Modelling of Marfe Phenomena in TEXTOR Tokamak*, Phys. Scr., **70**, (Part 2/3), 173-186, 2004.

[32] E.L. Vold, et al., *Fluid model equations for the tokamak plasma edge* , Phys. Fluids, **B 3**, 3132-3152, 1991.

[33] D. Reiter, et al., *The EIRENE and B2-EIRENE codes*, Fusion Science and Technology, **47**, 172-186, 2005.

[34] D. Reiter, et al., *The EIRENE code user manual* , Fusion Science and Technology, Available at www.eirene.de, 2017.

[35] H. P. Summers, *Atomic data and analysis structure user manual* , University of Strathclyde, 2nd edition, 2004.

[36] D. Reiter, *The data file AMJUEL: additional atomic and molecular data for EIRENE* , Available at www.eirene.de, 2011.

[37] A. Taroni, et al., *The Multi-Fluid Codes Edgeid and Edge2D: Models and Results* , Contrib. Plasma Phys., **32**, 438-443, 1992.

[38] R. Simonini, et al., *Models and numerics in the multi-fluid 2-D edge plasma code EDGE2D/U*, Contrib. Plasma Phys., **34**, 368-373, 1994.

[39] G. J. Radford, *The Application of Moment Equations to Scrape off Layer Plasmas*, Contrib. Plasma Phys., **32** (3-4), 297-302, 1992.

[40] D.J.Moulton, *Numerical Modelling of H-mode Plasmas on JET*, PhD Thesis Imperial College, England, 2012

[41] H. Bufferand, et al.*Numerical modelling for divertor design of the WEST device with a focus on plasma-wall interactions*, Nucl. Fus., **55**, 053025, 2015.

[42] G. Ciraolo, et al, *Investigation of Edge and SOL Particle Flux Patterns in High Density Regimes using SOLEDGE2D-EIRENE Code*, Contrib. Plasma Phys., **54** (4-6), 432-436, 2014.

[43] H. Bufferand, et al., *Applications of SOLEDGE-2D code to complex SOL configurations and analysis of Mach probe measurements*, J. Nucl. Mater, **415**, S589-S592, 2011.

[44] H. Bufferand, et al., *Near wall plasma simulation using penalization technique with the transport code SOLEDGE2D-EIRENE*, J. Nucl. Mater, **438**, S445-S448, 2013.

[45] V. Rozhansky, et al., *New B2SOLPS5.2 transport code for H-mode regimes in tokamaks*, Nucl. Fus., **49**, 025007, 2009.

[46] S. Wiesen, et al., *The new SOLPS-ITER code package*, J. Nucl. Mater, **463**, 480-484, 2015.

[47] Y. Feng, et al., *3D Edge Modeling and Island Divertor Physics*, Contrib. Plasma Phys., **44** (1-3), 57-69, 2004.

[48] D. Maisonnier, et al., *Power plant conceptual studies in Europe*, Nucl. Fus., **47**, 1524-1532, 2007.

[49] G. Federici, et al., *3D Overview of EU DEMO design and R&D activities*, Fusion Eng. Des., **89**, 882-889, 2014.

[50] A. Loarte, et al., *Effects of divertor geometry on tokamak plasmas*, Plasma Phys. Contr. Fusion, **43**, R183-R224, 2001.

[51] V. Pericoli Ridolfini, et al., *Comparative study of a conventional and snowflake divertor for the FAST (Fusion Advanced Studies Torus) tokamak*, J. Nucl. Mater, **438**, S414-S417, 2013.

[52] B. Viola, et al., *Preliminary Comparison of the Conventional and QuasiSnowflake Divertor Configurations with the 2D Code EDGE2D/EIRENE in the FAST Tokamak* , Contrib. Plasma Phys., **54**, No. 4-6, 459-463, 2014.

[53] V. Kotov, et al., *Numerical modelling of high density JET divertor plasma with the SOLPS4.2 (B2-EIRENE) code*, Plasma Phys. Contr. Fusion, **50**, 105012, 2008.

[54] A. Kallenbach, et al., *Multi-machine comparisons of H-mode separatrix densities and edge profile behaviour in the ITPA SOL and Divertor Physics Topical Group*, J. Nucl. Mater., **337-339**, 381-385, 2005.

[55] S. V. Mirnov, et al., *Experiments with lithium limiter on T-11M tokamak and applications of the lithium capillary-pore system in future fusion reactor devices*, Plasma Phys. Contr. Fusion, **48**, 821â€“837, 2006.

[56] R. J. Goldston, et al., *The lithium vapor box divertor*, Phys. Scr., **T167**, 014017 2016.

[57] I. E. Lyublinski, et al., *Status of design and experimental activity on module of lithium divertor for KTM tokamak*, Fusion Eng. Des., **88**, 1862-14865, 2013.

[58] T. W. Morgan, et al., *Liquid metals as a divertor plasma-facing material explored using the Pilot-PSI and Magnum-PSI linear devices*, Plasma Phys. Control. Fusion **60**, 014025, 2018.

[59] C. Lowry, et al., *Divertor configuration studies on JET*, J. Nucl. Mater., **241-243**, 438-443, 1997.

[60] R. Pitts, et al., *Divertor geometry effects on detachment in TCV*, J. Nucl. Mater., **290-293**, 940-946, 2001.

[61] M. Groth, et al., *Divertor plasma conditions and neutral dynamics in horizontal and vertical divertor configurations in JET-ILW low confinement mode plasmas*, J. Nucl. Mater., **463**, 471-476, 2015.

[62] A E Jaervinen, et al., *Impact of divertor geometry on radiative divertor performance in JET H-mode plasmas*,Plasma Phys. Contr. Fusion, **58**, 045011, 2016.

[63] G. Calabró, et al., *Divertor currents optimization procedure for JET-ILW high flux expansion experiments*,to be submitted .

[64] B. Viola, et al., *Impact of poloidal flux expansion on JET divertor radiation*,44th EPS Conference on Plasma Physics, Belfast, Northern Ireland, 2017.

[65] B. Viola, et al., *EDGE2D-EIRENE simulations of the impact of poloidal flux expansion onthe radiative divertor performance in JET*,Nucl. Mat. En., in press, 2016. doi:`http://dx.doi.org/10.1016/j.nme.2017.07.004`

[66] L. Frassinetti, et al., *Spatial resolution of the JET Thomson scattering system*, Rev. Sci. Instrum., **83**, 013506, 2012.

[67] A. Golev, et al., *A Note on the Soboleva' Modified Hyperbolic Tangent Activation Function*, International Journal of Innovative Science, Engineering & Technology, **Vol. 4**, Issue 6, June 2017.

[68] F. Milani, *Disruption Prediction at JET*, PhD Thesis, Univ. of Aston in Birmingham, 1998.

[69] S. Wiesen, et al., *Impact of the JET ITER-like wall on H-mode plasma fueling*, Nucl. Fus., **57**,066024 , 2017.